Dipl.-Ing. Manuel Johannes Zingl, BSc

Mott physics and transport properties of $BaMn_2As_2$ and LaMnAsO

DOCTORAL THESIS

For obtaining the academic degree of
Doktor der technischen Wissenschaften

Doctoral Program in Engineering Sciences
Doctoral School Physics

Graz University of Technology

Supervisor:
Univ.-Prof. Dr.rer.nat. Enrico Arrigoni

Co-Supervisor:
Ass.Prof. Dipl.-Ing. Dr.techn. Markus Aichhorn

Institute of Theoretical and Computational Physics

Graz, Sept. 2017

Abstract

High-temperature superconductivity, colossal magneto-resistance, Mott insulators, enhanced magnetism or a huge thermoelectric response are just a few examples of the exotic phenomena displayed by strongly correlated materials. With the exception of superconductivity, all these phenomena have been observed in the class of manganese pnictides. Particularly, we focus our theoretical investigation on $BaMn_2As_2$ and LaMnAsO, using the combination of density functional theory and dynamical mean-field theory. We show that the studied compounds are placed at the verge of a metal-insulator transition, which in turn is responsible for their high Néel temperatures. Although their crystal structure is composed of similar building blocks, our analysis shows that the two materials exhibit a very different effective dimensionality, LaMnAsO being a quasi-two-dimensional material, in contrast to the much more three dimensional $BaMn_2As_2$. We demonstrate that the experimentally observed differences in the Néel temperature, the band gap, and the optical properties of the manganese compounds under consideration can be traced back to exactly this difference in effective dimensionality. A special emphasis is put on the effect of electron doping in LaMnAsO, which results in unusually large Seebeck coefficients. We provide an investigation of the underlying electronic ingredients, by disentangling the role of magnetism, the influence of the peculiar band-structure shape and the degree of particle-hole asymmetry in the spectral function.

Kurzfassung

Stark korrelierte Materialien weisen oftmals eine Vielzahl von bemerkenswerten Eigenschaften auf. Beispiele dafür sind die Hochtemperatursupraleitung, der kolossale magnetoresistive Effekt, das Auftreten von Mott-Isolatoren, gute thermoelektrische Eigenschaften sowie verstärkter Magnetismus. Mit Ausnahme der Supraleitung wurden die genannten Phänomene in Manganpnictiden beobachtet. Anhand der Kombination aus Dichtefunktionaltheorie und dynamischer Molekularfeldtheorie untersuchen wir die zwei Vertreter $BaMn_2As_2$ und LaMnAsO aus dieser Materialklasse. Wir zeigen, dass diese Materialien nahe an einem Metall-Isolator-Übergang liegen, was wiederum die hohen Néel-Temperaturen erklärt. Obwohl deren Kristallstruktur aus ähnlichen Bestandteilen aufgebaut ist, zeigt unsere Analyse eine stark unterschiedliche effektive Dimensionalität der beiden Materialien auf. Wir klassifizieren LaMnAsO als ein quasi-zweidimensionales Material im Unterschied zu dem viel stärker dreidimensionalen $BaMn_2As_2$. Anschließend demonstrieren wir, dass die experimentell beobachteten Unterschiede in den Néel-Temperaturen, den Bandlücken und den optischen Eigenschaften auf genau diesen Unterschied in der effektiven Dimensionalität zurückgeführt werden können. Ein spezieller Schwerpunkt wird auf den Einfluss der Elektronendotierung gelegt, welche bei Raumtemperatur zu unüblich hohen Seebeck-Koeffizienten in LaMnAsO führt. Durch eine getrennte Betrachtung der Rolle des Magnetismus, der Auswirkung von speziellen Eigenschaften der Bandstruktur und der Asymmetrie der Spektralfunktion untersuchen wir die Wichtigkeit dieser verschiedenen elektronischen Einflüsse auf den Seebeck-Koeffizienten.

Acknowledgments

I would like to express my special thanks to Enrico Arrigoni who supported me not just throughout my PhD thesis, but also during my Master's thesis and my time as an undergraduate student. I am especially thankful for giving me the freedom to develop my own ideas.

My sincere gratitude goes to Markus Aichhorn for making himself available whenever I needed help – his door was always open. I am thankful for his invaluable competence in answering my countless questions. His ongoing support goes far beyond his duties.

I am grateful to A. Georges, O. Parcollet and M. Ferrero for making multiple research stays at Collége de France, École Polytechnique and CEA Saclay possible. I greatly enjoy working with you and being a part of the TRIQS community.

For their strong interest in my work and all the lengthy, but fruitful, discussions, I am deeply indebted to my closest co-students Daniel Bauernfeind, Gernot Kraberger and Robert Triebl. Without them this thesis would not have been possible.

Surely, I will miss the great working atmosphere at the Institute of Theoretical and Computational Physics. I am particularly grateful to (in alphabetical order) Lilia Boeri, Antonius Dorda, Gerhard Dorn, Hans Gerd Evertz, Delia Fugger, Martin Ganahl, Christoph Heil, Winfried Kernbichler, Michael Rumetshofer, Ewald Schachinger, Max Sorantin, Irakli Titvinitze, Wolfgang von der Linden, Jakob Neumayer, and Martin Nuss. Thanks for all the fun we had.

A big thank you goes to our system administrator Andreas Hirzy for solving my computer issues and our secretary Brigitte Schwarz for her help with bureaucratic work.

Finally, I would like to thank my parents with all my heart for their continuous support and most importantly Conny for her encouragement and all her love.

Contents

1. Introduction **1**

2. Theoretical background **5**

2.1. Density functional theory (DFT) 5
2.2. The Hubbard model 9
2.3. Dynamical mean-field theory (DMFT) 13
2.4. Impurity solvers 19
2.4.1. Exact diagonalization (ED) 20
2.4.2. Iterated perturbation theory (IPT) 21
2.4.3. Continuous-time hybridization expansion (CTHYB) 21
2.4.4. Fork tensor product states (FTPS) 23
2.5. Analytic continuation 25
2.6. The Mott transition 29
2.7. A successful marriage: DFT+DMFT 33

3. Transport properties **39**

3.1. Linear response 39
3.2. Optical conductivity in d $\rightarrow \infty$ 42
3.3. Connection to Boltzmann theory 47
3.4. TRIQS/DFTTools transport code 49

4. A prototypical example - $SrVO_3$ **53**

4.1. Introduction 53
4.2. Results 55
4.2.1. DFT and projective Wannier functions 55

4.2.2. Correlated spectral function . . . 57
4.2.3. Transport calculations . . . 59
4.2.4. Atomic multiplet structure . . . 61
4.3. Conclusion . . . 67

5. Importance of effective dimensionality in manganese pnictides 69
5.1. Introduction . . . 70
5.2. Methods . . . 72
5.3. Results . . . 74
5.3.1. Electronic structure . . . 74
5.3.2. Maximally localized Wannier functions . . . 78
5.3.3. Néel temperature . . . 81
5.3.4. Optical properties . . . 84
5.3.5. Further comparisons to experiments . . . 87
5.4. Conclusion . . . 92

6. Thermopower of electron-doped LaMnAsO 93
6.1. Introduction . . . 93
6.2. Methods . . . 95
6.3. Results . . . 96
6.3.1. Virtual crystal approximation (VCA) . . . 96
6.3.2. Spectral functions under electron doping . . . 99
6.3.3. Seebeck coefficient and its origin . . . 104
6.4. Conclusion . . . 112

7. Conclusions 113

A. DFT band structure of $BaMn_2As_2$ and LaMnAsO 115

B. Hall number of Sr_2RuO_4 117
B.1. Motivation . . . 117
B.2. Methods . . . 120
B.3. Results . . . 121

List of Abbreviations **129**

List of Publications and Presentations **131**

List of Figures **135**

List of Tables **137**

Bibliography **139**

1. Introduction

A central goal of computational condensed matter physics is the in-depth understanding of solids directly from "first principles". In contrast to an empirical modeling of experimental observations, the first principles approach starts from what we already know *ab initio*; namely that solids are essentially a collection of (ordered) atoms, with positively charged nuclei and a bunch of negatively charged electrons. The motion and the interaction of these constituents of solids are governed by fundamental quantum mechanical laws. Although the underlying physics of the individual parts is rather simple and well-understood, a sheer endless number of complex properties emerge from their interplay. Or, as P. W. Anderson remarks in "More is Different" [1]:

> The behavior of large and complex aggregations of elementary particles, it turns out, is not to be understood in terms of a simple extrapolation of the properties of a few particles. Instead, at each level of complexity entirely new properties appear, and the understanding of the new behaviors requires research which I think is as fundamental in its nature as any other.

Indeed, the prohibitively large size of the problem restricts the straightforward calculation of such emergent properties in practice. The most popular approaches to determine – at least – the electronic ground state are band-theory methods, like density functional theory (DFT) [2–4], which have proven to accurately explain physical properties of many materials, e.g. simple metals and insulators. However, materials which are governed by the physics of open d or f shells constitute cases where conventional band-theory methods often lead to even qualitatively wrong results, e.g. a system is predicted to be a metal while in fact it is an insulator. The single-electron picture fails in such materials, because of the localized nature of the valance orbitals in which electrons experience a strong Coulomb repulsion. Transition metals (e.g. copper, manganese, iron and vanadium) and their oxides fall into this class of so-called strongly

correlated materials. There the electronic correlations are the pivotal factor for the emergence of fascinating phenomena like high-temperature superconductivity [5], colossal magneto-resistance [6] or a huge thermoelectric response [7]. But precisely these electronic correlations make the theoretical and computational treatment of strongly correlated systems challenging.

In most cases many-body approaches based on low-energy model Hamiltonians need to be employed. The Hubbard model [8] is arguably the most intensively used in the context of real-material modeling, because it captures the essential physics of strongly correlated systems. This ranges from the description of the Mott metal-insulator transition [9] to antiferromagnetism [10] and possible d-wave superconductivity [11]. Although simple-looking, the Hubbard model turns out to be notoriously difficult to solve, especially in cases of multiple relevant orbital degrees of freedom. One of the most popular methods available to tackle the Hubbard model is the dynamical mean-field theory (DMFT) [12–16]. The success of DMFT is owed to the fact that it offers a bridge between the physics of itinerant and localized systems [15]. This is important to capture the nature of the Mott phenomenon, which is the occurrence of an insulating state solely due to electronic correlations [17]. With regard to the ab-initio modeling of such physics in real materials, the combination of DMFT with band theory (DFT+DMFT) [14, 18–20] has become the work-horse method in the last two decades.

In this thesis we focus on the two manganese pnictides $BaMn_2As_2$ and LaMnAsO, which are isostructural to the iron-based superconductors $BaFe_2As_2$ and LaFeAsO. In these compounds the whole $3d$ manifold is relevant for the electronic properties, and has thus to be taken into account on the level of the Hubbard model. In contrast to the iron pnictides, the investigated manganese compounds host five electrons in the five Mn-$3d$ bands, and as a consequence, electronic correlations are expected to promote Mott physics [21–23]. Multiple experiments show that both manganese pnictides are semiconductors [24–30], but also exhibit strong antiferromagnetic order persistent well above room temperature [31, 32]. Naturally, the question arises whether the semiconducting ground state in these half-filled systems is due to electronic correlations alone (Mott mechanism) or because of symmetry breaking due to magnetism (Slater mechanism). Although sharing the Mn-As layers as common building blocks, the difference in the interlayer distance suggest a classification of LaMnAsO as quasi-two-dimensional

compound [33–35], whereas $BaMn_2As_2$ is much more three dimensional [27, 36]. This substantial difference in the effective dimensionality of the two compounds is decisive to understand the experimentally observed differences in the Néel temperature, the band gap, and the optical conductivity.

Next to these properties, experiments have repeatedly reported enhanced Seebeck coefficients in manganese pnictides [37–43]. For example, $LaMnAsO_{1-\delta}F_\delta$ samples at room temperature exhibit a Seebeck coefficient of about $-300\,\mu V\,K^{-1}$ at a doping level of $\delta = 0.03$ [43]. Motivated by this finding, we carry out an investigation of the underlying electronic influences on the Seebeck coefficient of electron-doped LaMnAsO. Clearly, gaining a deeper understanding of the microscopic mechanisms at play is a critical first step towards purposefully designing thermoelectric materials [44]. This is again of major interest in the search of alternative energy sources [45, 46], as thermoelectric materials can intrinsically convert (otherwise wasted) heat into electric energy.

In general, we see it as an important task of theoretical condensed matter physics to provide manifold links to experiments. Transport properties, like the optical conductivity, Seebeck coefficients, or also Hall conductivities, constitute such links, because they are relatively easy accessible in both areas, theory and experiment. Therefore, a part of this work is devoted to the implementation of numerical tools for the evaluation of transport quantities within the DFT+DMFT framework.

In Ch. 2 we provide an overview of various aspects of the theoretical and computational modeling of strongly correlated materials. Then, in Ch. 3 we discuss the Kubo formula (linear response) for the (optical) conductivity and the Seebeck coefficient, as well as the corresponding details of the TRIQS/DFTTools transport code. On the example of the "benchmark" material $SrVO_3$, we demonstrate in Ch. 4 important aspects of DFT+DMFT calculations, and additionally provide new insights on the nature of its upper Hubbard band. We continue in Ch. 5 with the discussion of the electronic structure and the magnetic and optical properties of $BaMn_2As_2$ and LaMnAsO. In Ch. 6 we present our results on electron-doped LaMnAsO and study the electronic influences on the Seebeck coefficient. To keep Chs. 4, 5 and 6 self-contained we provide an individual introduction and conclusion for each of them. We supplement our work with App. B, where we discuss the calculation of Hall conductivities for strongly correlated materials and investigate the unusual temperature behavior of the Hall number of Sr_2RuO_4.

2. Theoretical background

Preamble

We start with the introduction of density functional theory (DFT) [2–4] and then work our way through the different aspects of the many-body Hubbard model to describe the low-energy physics of a material, especially with regard to the treatment of the model within dynamical mean-field theory (DMFT) [12–16]. We end with the DFT+DMFT method, which is nowadays the standard framework for the description of strongly correlated materials [14, 18–20].

As the well-known fundamental theories and concepts of condensed matter physics do not change over the short time span of a PhD thesis, some parts of this chapter contain adapted, modified or extended parts of the author's Master's thesis [47]. For the basics of solid state physics we refer the reader to one of the many comprehensive textbooks available, e.g. Ref. [48]. Throughout this chapter we employ atomic units ($e = m_e = \hbar = k_B = 1$), where the charge is measured in units of the electron charge e, the mass in units of the electron mass m_e and energies in units of $\hbar$.

2.1. Density functional theory (DFT)

The quantum-mechanical dynamics of a solid can be understood in terms of the movement of electrons and ions. As the dynamics of the ions is happening on a much smaller time-scale, in comparison to the dynamics of the electrons, we can use the

Born-Oppenheimer approximation and take the nuclei to be fixed.[1] Then, the Hamiltonian which describes the electron dynamics of any solid is [48]

$$H = -\frac{1}{2}\sum_i \nabla_i^2 - \sum_{\alpha i}\frac{Z_\alpha}{|\mathbf{r}_i - \mathbf{r}_\alpha|} + \frac{1}{2}\sum_{i\neq j}\frac{1}{|\mathbf{r}_i - \mathbf{r}_j|}\ , \tag{2.1}$$

where $\mathbf{r}$ is the position vector of the electrons labeled with the subscripts i/j and the nuclei labeled with the subscript α. The first term is the kinetic energy of the electrons and the second one the attractive Coulomb interaction between the positive nuclei (Z_α is the atomic number) and the electrons. The last term, the repulsive electron-electron interaction, is the cumbersome bit. The reason is that, although all the relevant physics is contained in Hamiltonian 2.1, the solution of the associated Schrödinger equation for a N-electron problem

$$H\psi\left(\mathbf{r}_1, ..., \mathbf{r}_N\right) = E\psi\left(\mathbf{r}_1, ..., \mathbf{r}_N\right) \tag{2.2}$$

is prohibitively expensive due to the exponential scaling of the Hilbert space dimension of the N-electron wave function $\psi\left(\mathbf{r}_1, ..., \mathbf{r}_N\right)$. Without electron-electron interactions the system is separable, hence the problem reduces to solving N single-particle Schrödinger equations.

One possible way to treat Eq. 2.2 in the presence of electron-electron interactions is the density functional theory (DFT) [2–4]. This ground-state theory maps the intractable many-body problem to a system of non-interacting electrons moving in an *effective* one-particle potential mediated by all the other electrons and nuclei. DFT is based on the Hohenberg-Kohn theorem [49]:

1. For any given external potential v_{ext} (as, e.g., the potential of the nuclei in Eq. 2.1) there exists a unique ground-state electron density $n^0(\mathbf{r})$. The total energy E of a system is a functional of the ground-state electron density $E\left[n^0(\mathbf{r})\right]$.[2]

2. It can be shown that in analogy to the Rayleigh-Ritz variational principle for wave functions, a variational principle for the ground-state density exists. The total en-

[1] Additionally, we neglect contributions from relativistic effects like the spin-orbit interaction, but these might be included, e.g., on a perturbative level.

[2] To be precise, the ground-state expectation value of *any* observable is a functional of the ground-state density.

ergy has its minimum at the true ground-state density, thus $E[n^0(\mathbf{r})] \leqslant E[n(\mathbf{r})]$ for any density $n(\mathbf{r})$.

The Hohenberg-Hohn theorem allows to deal with the electron density $n(\mathbf{r})$ instead of the full wave function. This constitutes an enormous simplification of the many-body problem, because the number of dimensions is always three (spatial dimensions). It should be emphasized that for ground-state properties DFT is per se exact. However, the Hohenberg-Kohn theorem does not provide rules how to construct the effective one-particle potential, and in practical applications one is always forced to employ approximations, as we will see in the following.

In a first step we can split off the known parts and collect the unknown parts in the exchange-correlation functional E_{xc} [49]

$$E[n] = T[n] + \int d\mathbf{r}\ v_{ext}(\mathbf{r}) + \frac{1}{2}\int d\mathbf{r}\ d\mathbf{r}'\ \frac{n(\mathbf{r})n(\mathbf{r}')}{|\mathbf{r}-\mathbf{r}'|} + E_{xc}[n(\mathbf{r})]\ . \tag{2.3}$$

The first part $T[n]$ denotes the electronic kinetic energy of the many-body problem. The second term describes the effect of the external potential $v_{ext}(\mathbf{r})$ that stems from the nuclei and/or possible external fields. The third term is the Hartree potential and it captures the electrostatic contribution to the electron-electron interaction. The last term, namely the exchange-correlation energy $E_{xc}[n(\mathbf{r})]$, gathers all the remaining unknown electron-electron interactions. In practice, this can only be approximated.

A major breakthrough was achieved by the work of Kohn and Sham [50]. They introduced an auxiliary non-interacting reference system with the same ground-state density as the interacting system

$$E[n] = \tilde{T}[n] + \int d\mathbf{r}\ v_{ext}(\mathbf{r}) + \frac{1}{2}\int d\mathbf{r}\ d\mathbf{r}'\ \frac{n(\mathbf{r})n(\mathbf{r}')}{|\mathbf{r}-\mathbf{r}'|} + \tilde{E}_{xc}[n(\mathbf{r})]\ . \tag{2.4}$$

The kinetic energy of the auxiliary Kohn-Sham systems is

$$\tilde{T}[n] = \sum_i^N \langle\varphi_i|\,\frac{p}{2}\,|\varphi_i\rangle\ , \tag{2.5}$$

where $\varphi_i(\mathbf{r})$ are the so-called Kohn-Sham orbitals of the auxiliary system with N independent particles. The difference in the kinetic energy of the true system and the

auxiliary system has been put into the exchange-correlation functional $\tilde{E}_{xc}[n(\mathbf{r})]$. The electron density of the system is given by

$$n(\mathbf{r}) = \sum_{i=1}^{N} |\varphi_i(\mathbf{r})|^2 \ . \tag{2.6}$$

The variation of the above energy functional, $\delta E[n(\mathbf{r})] = 0$, leads to a one-electron Schrödinger equation [50]

$$\left(-\frac{1}{2}\nabla^2 + v_{KS}(\mathbf{r})\right)\varphi_i(\mathbf{r}) = \epsilon_i \varphi_i(\mathbf{r}), \tag{2.7}$$

with the Kohn-Sham potential $v_{KS}(\mathbf{r})$ defined as

$$v_{KS}(\mathbf{r}) = v_{ext}(\mathbf{r}) + \int d\mathbf{r}' \ \frac{n(\mathbf{r}')}{|\mathbf{r}-\mathbf{r}'|} + \frac{\delta \tilde{E}_{xc}[n(\mathbf{r})]}{\delta n(\mathbf{r})} \ . \tag{2.8}$$

The exchange-correlation functional can be written in terms of an exchange-correlation energy density $\epsilon_{xc}[n]$

$$\tilde{E}_{xc}[n(\mathbf{r})] = \int d\mathbf{r} \ n(\mathbf{r}) \, \epsilon_{xc}[n](\mathbf{r}) \ . \tag{2.9}$$

The fact that this exchange-correlation functional is unknown has led to a plethora of different approximations. The simplest, yet frequently used, approximation is the local density approximation (LDA) [51], where the exchange-correlation energy density $\epsilon_{xc}[n]$ does only depend on the local electron density. This assumption turns $\epsilon_{xc}[n]$ into a simple function of the density, $\epsilon_{xc}^{LDA}(n(\mathbf{r}))$, evaluated at point $\mathbf{r}$. In practice, the values of ϵ_{xc}^{LDA} are taken from a homogeneous electron gas of the same density. Another type is the generalized gradient approximation (GGA), where the exchange-correlation energy is assumed to depend not just on the density but also on its gradient $\epsilon_{xc}^{GGA}(n(\mathbf{r}), \nabla n(\mathbf{r}))$. Since GGA involves several adjustable parameters, many different schemes exist, where one of the most popular ones is the Perdew-Burke-Ernzerhof functional (PBE) [52]. The GGA-PBE functional is used for all DFT calculations carried out in this work.

The set of Kohn-Sham equations presented above (Eqs. 2.6, 2.7, 2.8 and 2.9) are solved self-consistently for the ground-state energy and the ground-state density. The solution of the Kohn-Sham equations also yields the Kohn-Sham eigenstates ϵ_i and the

Kohn-Sham eigenfunctions $\varphi_i(\mathbf{r})$, which are usually denoted as the DFT energies and the DFT orbitals. However, one has to be careful with an interpretation of the Kohn-Sham eigensystem in terms of physical quantities, because the Kohn-Sham spectrum is strictly speaking only a mathematical tool representing the auxiliary single-particle problem. Nevertheless, for many classes of materials, the DFT spectrum does compare surprisingly well with experimental data, even on a quantitative level.

2.2. The Hubbard model

Band theory ultimately fails as soon as the single-particle picture breaks down, which is the case in materials governed by the physics of electrons in localized open d or f shells. In these strongly correlated materials DFT does often provide even qualitatively wrong results, e.g. predicting a metallic ground state although the material is in reality an insulator. Therefore, many-body models based on low-energy Hamiltonians are used to capture the effect of electronic correlations. The (multi-orbital) Hubbard model [8] is the one usually set up in the context of real-material modeling to describe the valence electrons of the correlated orbitals around the Fermi energy. In the Hubbard model these orbitals correspond to sites arranged on a translationally invariant lattice, like in the real crystal (for a sketch see Fig. 2.1). Enforced by the Pauli principle, each orbital can be either empty, or occupied by one spin-up or spin-down electron, or occupied by two electrons with opposite spins.

In the simplest single-band (single-orbital) version the Hubbard Hamiltonian in second quantization is [8]

$$H = \sum_{\langle i,j\rangle\sigma} t_{ij} \left(c^\dagger_{i\sigma} c_{j\sigma} + \text{h.c.} \right) - \mu \sum_{i\sigma} n_{i\sigma} + U \sum_i n_{i\uparrow} n_{i\downarrow} \ . \tag{2.10}$$

The first term of the model is the kinetic energy of the electrons, which is understood as a hopping t_{ij} from site j to site i. The operators (in second quantization) present in the first term of the model destruct an electron with spin σ on site j (operator $c_{j\sigma}$) and creates it again, with the same spin, on site i (operator $c^\dagger_{i\sigma}$). In general, a direct hopping to any other site is possible, but is very unlikely for far apart atoms due

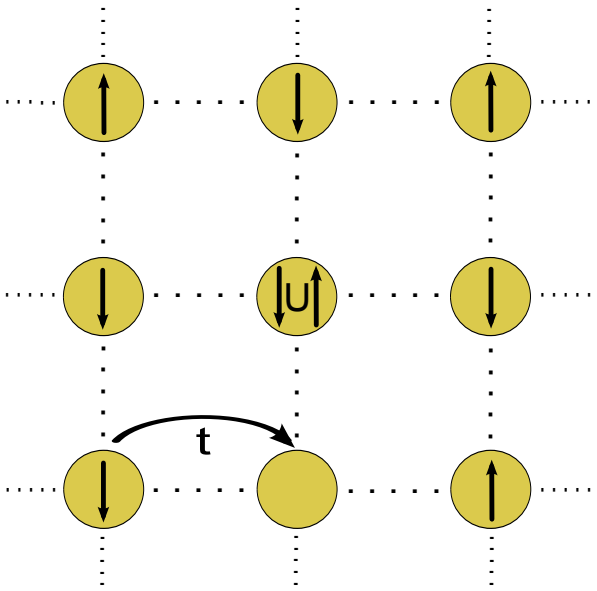

Figure 2.1.: Sketch of the single-orbital Hubbard model for electrons living on a 2D square lattice. Each circle corresponds to a lattice site. The electrons and their spins are indicated by the arrows in the circles. Electrons can hop to neighboring sites with hopping strength t and experience an on-site Coulomb repulsion U. This figure is taken from Ref. [47].

to the exponential diminution of the atomic wave functions. Often only hoppings to nearest-neighbor atoms are taken into account (denoted by $\langle i, j \rangle$ in Eq. 2.10).[3] The second term is the chemical potential μ of the system and the third term of the Hubbard model captures the electron-electron interaction. This "contact" Coulomb interaction U penalizes two electrons occupying the same lattice site. Note that $n_{i\uparrow} = c^{\dagger}_{i\uparrow} c_{i\uparrow}$ is the spin-density operator of site i and the occupation density operator is given by $n_i = n_{i\uparrow} + n_{i\downarrow}$. Electronic inter-atomic interactions are neglected, because undoubtedly the biggest contribution stems from two electrons occupying the same site.

Of course, the single-orbital Hubbard model is hardly sufficient to describe the complexity of the physics found in real materials with, e.g., open $3d$ shells. Hence, two additional points have to be considered [54]: First, the effect of orbital degrees of freedom on the hopping of electrons between different atoms, and second, the role of intra-atomic interactions between different orbitals. To this end, we extend the

[3] However, to study, for example, high-T_c superconductors it is necessary to consider also next-nearest-neighbor hoppings [53].

single-orbital Hubbard model to a multi-orbital version by assigning an orbital index to each lattice site and including additional orbital interaction terms. Then, the general form of the multi-orbital Hubbard model reads

$$\begin{aligned} H &= -\sum_{\substack{\langle i,j\rangle \\ \alpha\beta\sigma}} t_{i\alpha j\beta}\left(c^{\dagger}_{i\alpha\sigma}c_{j\beta\sigma} + \text{h.c.}\right) - \mu\sum_{i\alpha\sigma} n_{i\alpha\sigma} + \sum_i H_{U,i} \\ H_{U,i} &= \frac{1}{2}\sum_{\substack{\alpha\beta\gamma\delta \\ \sigma\sigma'}} \widetilde{U}_{\alpha\beta\gamma\delta} c^{\dagger}_{i\alpha\sigma}c^{\dagger}_{i\beta\sigma'}c_{i\delta\sigma'}c_{i\gamma\sigma} \ , \end{aligned} \tag{2.11}$$

where $\alpha\beta\gamma\delta$ are orbital indices, i.e. magnetic angular-momentum quantum numbers, and $H_{U,i}$ is the local interaction on lattice site i. $\widetilde{U}_{\alpha\beta\gamma\delta}$ is the general 4-index interaction tensor.

For an isolated atom, under consideration of the spherical symmetry, the interaction tensor $\widetilde{U}_{\alpha\beta\gamma\delta}$ can be efficiently parametrized by a small set of Slater integrals [55]. The full interaction tensor in Slater expansion for orbitals with an angular momentum l is given by [56–58]

$$\widetilde{U}_{\alpha\beta\gamma\delta} = \sum_{k=0}^{2l} \Theta^k\left(\alpha,\beta,\gamma,\delta\right) F^k \ . \tag{2.12}$$

The angular part Θ^k can be calculated from the spherical harmonics Y_{lm}

$$\Theta^k(\alpha,\beta,\gamma,\delta) = \frac{4\pi}{2k+1}\sum_{q=-k}^{k} \langle Y_{l\alpha}|Y_{kq}Y_{l\gamma}\rangle\langle Y_{l\beta}Y_{kq}|Y_{l\delta}\rangle \ . \tag{2.13}$$

Additionally, the Slater integrals F^k are obtained from the radial part of the wave functions R_{nl}

$$F^k = \int_0^{\infty} dr\ r^2 \int_0^{\infty} dr'\ r'^2\ \frac{\min(r,r')^k}{\max(r,r')^{k+1}}\ R^2_{nl}(r)R^2_{nl}(r') \ , \tag{2.14}$$

where n is the principal quantum number. Importantly, only three slater integrals (F^0, F^2 and F^4) are necessary to parametrize the interaction in the d shell ($l = 2$). We define the Hubbard U as the simple average over all possible pairs of orbitals [57, 58]

$$U \equiv \frac{1}{(2l+1)^2}\sum_{\alpha\beta}\sum_{k=0}^{2l} \Theta^k\left(\alpha,\beta,\alpha,\beta\right) F^k = F^0 \ , \tag{2.15}$$

and Hund's coupling J as

$$J \equiv \frac{1}{2l\,(2l+1)} \sum_{\alpha \neq \beta} \sum_{k=0}^{2l} \Theta_k\,(\alpha,\beta,\beta,\alpha)\,F^k = \frac{F^2+F^4}{14} \quad \text{(for } d \text{ electrons)}. \tag{2.16}$$

Further, as a relationship between F^2 and F^4 usually the atomic value $F^4/F^2 = 0.625$ is used [57]. This means that the full 4-index interaction tensor $\widetilde{U}_{\alpha\beta\gamma\delta}$ can be initialized by only two values: U and J. Note that the Slater parametrization of $H_{U,i}$ is fully rotational invariant, hence it does not change under unitary basis transformations.

In a solid we have to take into account that the surrounding electron cloud rearranges in response to the Coulomb potential of a charge, and thus the long-ranged Coulomb interaction will be screened.[4] The effect of screening is a substantial reduction of the atomic values of U and J.[5] To keep the imposed form of $\widetilde{U}_{\alpha\beta\gamma\delta}$, we assume that also the screened interactions are spherically symmetric. Two common methods to obtain the interaction parameters directly from band-structure calculations are the constrained local density approximation (cLDA) [59] and the constrained random phase approximation (cRPA) [60]. We do not employ these – sometimes delicate – methods for the compounds studied in this thesis, but rather use physical reasoning or, if available, values for U and J present in the literature.

Another parametrization of the interaction part of the Hubbard model, specifically constructed for the t_{2g} subspace, was proposed by Kanamori [61]

$$\begin{aligned} H^K_{U,i} =& U_K \sum_\alpha n_{i\alpha\uparrow} n_{i\alpha\downarrow} + \sum_{\alpha>\beta,\sigma} \left(U'_K n_{i\alpha\sigma} n_{i\beta\bar{\sigma}} + (U'_K - J_K)\, n_{i\alpha\sigma} n_{i\beta\sigma} \right) \\ & - \sum_{\alpha\neq\beta} J_K \left(c^\dagger_{i\alpha\downarrow} c^\dagger_{i\beta\uparrow} c_{i\beta\downarrow} c_{i\alpha\uparrow} + c^\dagger_{i\beta\uparrow} c^\dagger_{i\beta\downarrow} c_{i\alpha\uparrow} c_{i\alpha\downarrow} + \text{h.c.} \right) . \end{aligned} \tag{2.17}$$

Here, $\bar{\sigma}$ denotes the opposite spin of σ. When setting $U'_K = U_K - 2J_K$, which is strictly true only for an isolated atom, the Kanamori Hamiltonian is equivalent to the Slater Hamiltonian projected to the t_{2g} subspace. Of course, the interaction values U and J have to be adjusted accordingly. With the above choice of U'_K the Kanamori Hamiltonian is rotationally invariant under orbital rotations [62].

[4] This is also a reason why inter-atomic interactions are usually neglected in the Hubbard model.
[5] From this point on we always refer to the screened values when using the variables U and J

From the form of the Kanamori Hamiltonian it is easy to see how local atomic physics enters the Hubbard model. The interaction favors an electronic state with electrons in different orbitals, but with their spins pointing in the same direction ($U_K - 3J_K$ terms), over a state with electrons in different orbitals and with different spins ($U_K - 2J_K$ terms). The latter is again favored over a state with two electrons in the same orbital (U_K terms). This is in fact nothing else but Hund's second rule. Note that the terms in the last line of Eq. 2.17 describe spin-flip and pair-hopping processes.

In Chs. 5 and 6 we employ the Slater parametrization for the interaction to describe the Mn-3*d* subspace of the investigated manganese pnictides. The Kanamori Hamiltonian is used in Ch. 4 for the V-t_{2g} subspace of $SrVO_3$ and in App. B for the Ru-t_{2g} subspace of Sr_2RuO_4.

2.3. Dynamical mean-field theory (DMFT)

Treating both the kinetic one-particle term and the potential-energy term of Eq. 2.10 on an equal footing is a highly non-trivial task, because the kinetic term is diagonal in momentum space, whereas the interaction term is essentially diagonal in real space. Only in the special case of a one-dimensional system exact solutions exist for the Hubbard model [63].

The dynamical mean-field theory (DMFT) [12–16], developed over the last three decades, is one of the most powerful non-perturbative methods to deal with the Hubbard model. In contrast to a static mean-field decoupling of the interaction term, the dynamical mean-field theory, as the name suggests, employs a *dynamical* mean-field, which depends on time, i.e. frequency, and therefore includes temporal quantum fluctuations. These fluctuations are important to capture the metal-insulator transition (cf. Sec. 2.6), which is not possible to explain within static mean-field theory without breaking the symmetry of the lattice. Several ways to obtain the dynamical mean-field equations exist [15], e.g. the cavity method or an expansion around the atomic limit. In the following we discuss the key conceptual points of DMFT, but refer the reader to extensive reviews available in the literature [14–16, 64].

Before we can start, we should note that DMFT is formulated in terms of *single-particle* Green's functions $G(\mathbf{k}, z)$, where $\mathbf{k}$ are elements of the reciprocal space.[6] The Green's functions $G(\mathbf{k}, z)$ (and also the self-energies $\Sigma(\mathbf{k}, z)$) are complex analytic functions defined in the whole complex frequency plane z, with the exception of poles on the real-frequency axis ω. If calculations are carried out for real frequencies $z = \omega + i0^+$, where the positive infinitesimal 0^+ shifts the poles off the real axis into the lower complex half-plane, the result is the retarded Green's function $G(\mathbf{k}, \omega + i0^+)$. For the sake of simplicity, we drop the infinitesimal 0^+ and use $G(\omega)$ to denote the retarded Green's function. This is a pivotal quantity as it is directly related to the $\mathbf{k}$-resolved spectral function of the system $A(\mathbf{k}, \omega)$ via

$$A(\mathbf{k}, \omega) = \frac{i}{2\pi} \mathrm{Tr} \left[G(\mathbf{k}, \omega) - G^\dagger(\mathbf{k}, \omega) \right] \ , \tag{2.18}$$

where the trace is taken over the orbital indices. Only in the case of a single-orbital model Eq. 2.18 reduces to

$$A(\mathbf{k}, \omega) = -\frac{1}{\pi} \Im \left[G(\mathbf{k}, \omega) \right] \ . \tag{2.19}$$

Summing $A(\mathbf{k}, \omega)$ over $\mathbf{k}$ gives the total spectral function[7]

$$A(\omega) = \sum_{\mathbf{k}} A(\boldsymbol{k}, \omega) \ , \tag{2.20}$$

which is equivalent to the density of states (DOS) for a non-interacting system. In some cases the Green's function is easier to compute on the Matsubara axis $z = i\omega_n$ with discrete (fermionic) Matsubara frequencies ω_n defined as

$$\omega_n = \frac{(2n+1)\,\pi}{\beta} \qquad (n \in \mathbb{Z}) \ . \tag{2.21}$$

The Matsubara Green's function $G(\mathbf{k}, i\omega_n)$ is directly connected to a finite temperature ($\beta = 1/T$), however to obtain real-frequency spectral functions an analytic continuation $G(\mathbf{k}, i\omega_n) \rightarrow G(\mathbf{k}, \omega)$ is necessary (see Sec. 2.5).

[6] An introduction on the theory of Green's functions is covered by various textbooks (see, e.g., Refs. [65, 66]). For multi-orbital models the Green's functions and the self-energies are matrices in the orbital indices. We omit the orbital indices for a better readability, hence the notation corresponds to a single-orbital model.

[7] All $\mathbf{k}$ summations in this work imply a normalized summation over the 1$^{\mathrm{st}}$ Brillouin zone (BZ).

The foundation for DMFT was laid (i) by the work of Metzner and Vollhard [12] on the limit of the infinite-dimensional Hubbard model and by (ii) Georges and Kotliar on the self-consistent mapping of the Hubbard model to an effective impurity model [13]. The key concept of DMFT is to approximate the lattice model by a (local) effective dynamical impurity problem (see the sketch in Fig. 2.2) [14]. This auxiliary problem consists of an interacting impurity site coupled to an infinite non-interacting bath. The effective bath models the communication of the impurity site with the residual lattice, and thus represents the dynamical aspect of the theory. In the course of time electrons can come from the bath to occupy the impurity site and eventually jump back again into the bath. Nevertheless, the effective bath is not known a priori and needs to be determined in a self-consistent way.

It is important to point out that the self-energy of the impurity model $\Sigma_{imp}(z)$ is a $\mathbf{k}$-independent quantity. The essential approximation of DMFT is to replace the $\mathbf{k}$-dependent lattice self-energy $\Sigma_{lat}(\mathbf{k}, z)$ by the local one of the effective impurity model

$$\Sigma_{lat}(\mathbf{k}, z) \approx \Sigma_{imp}(z) \ . \tag{2.22}$$

Playing to the strength of the theory, this approximation is exact in three limits [14]:

- **Non-interacting limit ($U = 0$)**
  The self-energy is trivially $\mathbf{k}$-independent as it vanishes ($\Sigma_{lat}(\mathbf{k}, z) = 0$).

- **Atomic limit ($t_{ij} = 0$)**
  This describes the case of disconnected atoms, which reduces the impurity model to an atomic problem. The self-energy is thus a local quantity.

- **Limit of infinite connectivity or infinite dimension ($d \to \infty$)**
  It can be shown that the self-energy becomes a local quantity for a lattice with infinite dimensionality d [12].

Of course, away from these limits the $\mathbf{k}$-independence of the self-energy is only an approximation. The physical interpretation of the DMFT approximation is that spatial correlations are neglected, but on the other hand temporal correlations (fluctuations) are included in the theory. This means that the quantum nature of each individual site is respected, which contrasts with standard mean-field theory where both spatial and temporal correlations are frozen out.

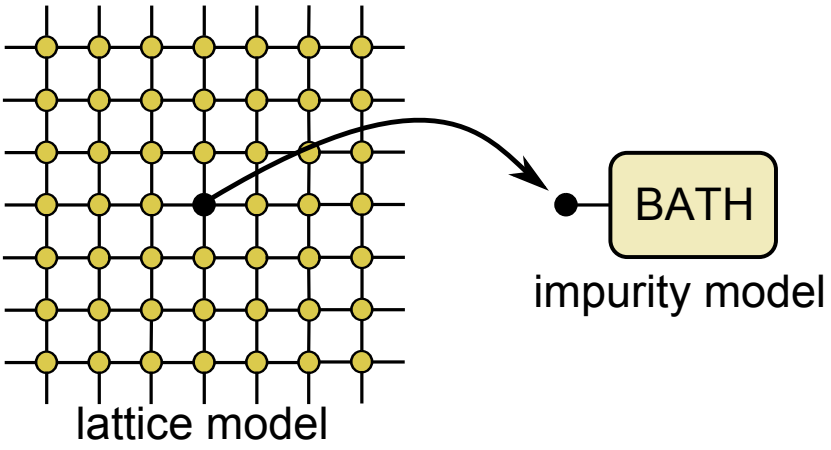

Figure 2.2.: Within DMFT the lattice problem is mapped to a single-impurity site coupled to an effective bath. This sketch is taken from Ref. [47].

The mapping to an impurity model demands equivalence between the local lattice Green's function $G_{loc}(z)$ and the impurity Green's function $G_{imp}(z)$

$$G_{loc}(z) \stackrel{!}{=} G_{imp}(z) \ , \tag{2.23}$$

with $G_{loc}(z)$ defined as the $\mathbf{k}$-summation over the lattice Green's function $G(\mathbf{k}, z)$

$$G_{loc}(z) = \sum_{\mathbf{k}} G(\mathbf{k}, z) = \sum_{\mathbf{k}} \frac{1}{z - \epsilon_{\mathbf{k}} + \mu - \Sigma(z)} \ . \tag{2.24}$$

We have already assumed a given but $\mathbf{k}$-independent self-energy $\Sigma(z)$. In Eq. 2.24 the $\epsilon_{\mathbf{k}}$ represent the eigenenergies of the non-interacting system in the reciprocal space, i.e. the Fourier transform of the hoppings t_{ij} in Eq. 2.10. We point out that Eq. 2.23 is central to DMFT, because it reflects the mapping of a lattice problem to an impurity problem. Via Dyson's equation we can now construct the bath Green's function

$$\mathcal{G}_0(z) = \left[G_{loc}^{-1}(z) + \Sigma(z)\right]^{-1} \ . \tag{2.25}$$

The $\mathcal{G}_0(z)$ is a quantum generalization of the effective Weiss field in standard mean-field theory, and is also known as the effective Weiss Green's function. We note that $\mathcal{G}_0(z)$ is *not* the bare lattice Green's function, but the local Green's function with locally removed interactions.

However, $\mathcal{G}_0(z)$ is exactly the bare Green's function of the impurity model

$$G_{0,imp}(z) = \mathcal{G}_0(z) \ , \tag{2.26}$$

and thus defines the non-interacting part of the impurity system. Commonly, the non-interacting impurity model is described in terms of the bath hybridization function $\Delta(z)$, which is related to $G_{0,imp}(z)$ via

$$G^{-1}_{0,imp}(z) = z + \mu - \Delta(z) \ . \tag{2.27}$$

From Eqs. 2.24, 2.25, 2.26, and 2.27 follows the DMFT self-consistency condition

$$G_{loc}(z) = \sum_{\mathbf{k}} \frac{1}{G^{-1}_{loc}(z) - \epsilon_{\mathbf{k}} + \Delta(z)} \ . \tag{2.28}$$

The task of a DMFT calculation is to determine the hybridization function $\Delta(z)$ such that Eq. 2.28 is fulfilled. This can be done in an iterative way, which includes the crucial step of solving the interacting impurity problem. Usually a simple forward-iteration scheme (DMFT cycle), as shown in Fig. 2.3 and described in the following, is used:

1. An initial starting point for the self-energy $\Sigma(z)$ is required. Often, $\Sigma(z) = 0$ is sufficient, however a self-energy from a related calculation, e.g. with similar U, might also offer an appropriate starting point.

2. The local Green's function $G_{loc}(z)$ is calculated from Eq. 2.24. The chemical potential μ should be adjusted at this point to ensure the desired filling of the lattice.

3. Next, the bath Green's function $\mathcal{G}_0$ is obtained with the Dyson equation (Eq. 2.25).

4. The solution of the impurity problem results in the impurity Green's function $G_{imp}(z)$. A selection of impurity solvers is discussed in Sec. 2.4.

5. Subsequently, the self-energy $\Sigma_{imp}(z)$ can be calculated for the impurity model via Dyson's equation: $\Sigma_{imp}(z) = G^{-1}_{0,imp}(z) - G^{-1}_{imp}(z)$.

6. Finally, $\Sigma_{imp}(z)$ is used as self-energy of the lattice $\Sigma^{\text{new}}(z) = \Sigma_{imp}(z)$ and is set as new input self-energy for the next iteration starting with step 2.

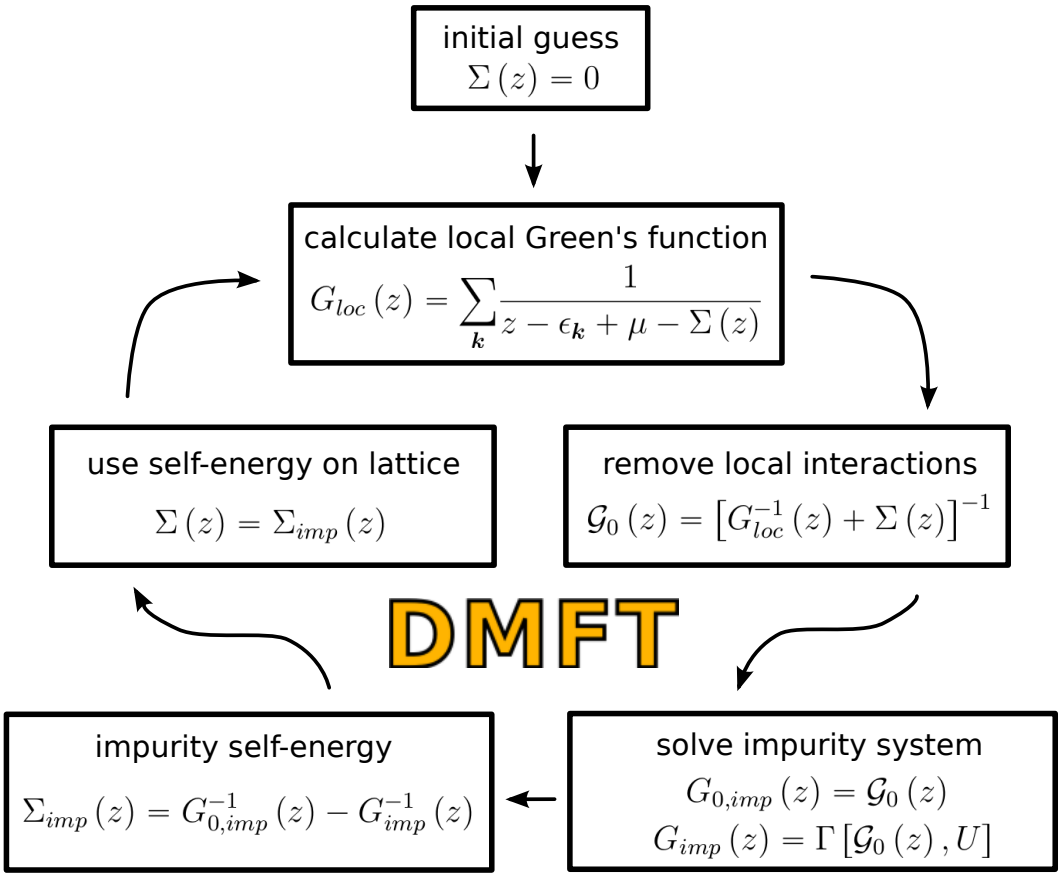

Figure 2.3.: The DMFT self-consistency cycle. Starting from an initial guess for the self-energy $\Sigma(z)$ the local lattice Green's function $G_{loc}(z)$ is obtained in the first step. Next, the bath Green's function $\mathcal{G}_0(z)$ is calculated with Dyson's equation. Solving the impurity model, which is defined by $\mathcal{G}_0(z)$ and the interaction, gives the impurity Green's function $G_{imp}(z)$ and leads via Dyson's equation to a new self-energy $\Sigma(z)$. The whole procedure is iterated until convergence is reached.

The self-consistency cycle stops when convergence is reached. This should be checked on multiple levels, meaning that not just the self-energy $\Sigma_{imp}(z)$, but also $G_{imp}(z)$, $\mathcal{G}_0(z)$ and μ can be assessed. Surprisingly, with this simple forward-iteration scheme convergence can be reached rather quickly. In regimes close to phase transitions, where convergence can be expected to be slower, mixing schemes might be used to enhance the convergence properties of the DMFT cycle.

2.4. Impurity solvers

DMFT transfers the notoriously difficult task of solving the Hubbard model to solving a (multi-orbital) Anderson impurity model (AIM), but this multiple times. For simplicity, we carry out our following considerations mainly for a single-impurity site, i.e. a model with only one orbital.

In second quantization the AIM is given by an interacting impurity site coupled to an infinite number of non-interacting bath sites. In general, there exist an infinite number of bath geometries which can describe the non-interacting bath exactly. An intuitive representation of the impurity system is the so-called star geometry (depicted in Fig. 2.4), where all bath sites i couple only to the impurity site via the hopping t_{0i}. The single-orbital AIM Hamiltonian in star geometry reads [67]

$$H_{AIM} = \underbrace{U n_{0\uparrow} n_{0\downarrow} + \epsilon_0 \sum_{\sigma} n_{0\sigma}}_{H_{loc}} + \underbrace{\sum_{i=1,\sigma}^{\infty} \epsilon_i a_{i\sigma}^{\dagger} a_{i\sigma}}_{H_{bath}} + \underbrace{\sum_{i=1,\sigma}^{\infty} t_{0i} \left(a_{i\sigma}^{\dagger} a_{0\sigma} + \text{h.c.} \right)}_{H_{hyb}} . \tag{2.29}$$

The different parts of the AIM Hamiltonian are the local part H_{loc} describing the impurity site, the bath terms H_{bath} containing all non-interacting bath sites, and the coupling of these two systems H_{hyb}. The parameters of the impurity site (U and the impurity on-site energy ϵ_0) are given by the lattice Hamiltonian. This means that the interaction on the impurity site is exactly the same as the local interaction of the Hubbard model (Eq. 2.10), which is described by the interaction tensor $\tilde{U}_{\alpha\beta\gamma\delta}$ in the case of multi-orbital models (see Eq. 2.11 and the corresponding discussion). The remaining parameters (on-site energies ϵ_i of the bath levels and hoppings t_{0i}) are defined by the hybridization function in star geometry

$$\Delta(z) = \sum_{i=1}^{\infty} \frac{|t_{0i}|^2}{z - \epsilon_i} . \tag{2.30}$$

Obtaining the Green's function of the impurity problem constitutes the computationally demanding part of every DMFT calculation, but fortunately many numerical methods have been developed, both working on the real- and the imaginary-frequency axis. Examples of Hamiltonian-based methods treating the AIM in second quantization are

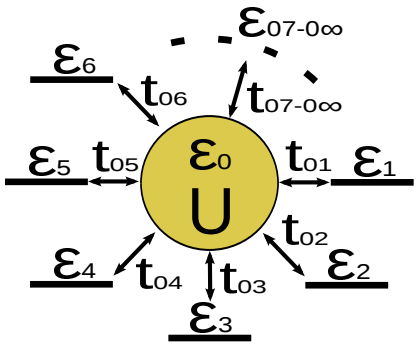

Figure 2.4.: AIM in star geometry. Each bath site couples directly to the impurity site. Within DMFT the parameters ϵ_0 and U are fixed by the lattice model and the bath parameters are defined by the bath Green's function $\mathcal{G}_0(z)$, i.e. the hybridization $\Delta(z)$. This figure is taken from Ref. [47].

exact diagonalization [15, 68, 69] and renormalization group techniques (e.g. NRG [70], DMRG [71]). However, also solvers working directly with the impurity Green's function or the hybridization function like perturbative approaches (e.g. IPT [72], NCA [73]) or quantum Monte Carlo methods (e.g. HFQMC [74], CTQMC [75]) are often employed. All approaches have their advantages and disadvantages, and, of course, the appropriate choice of method depends on the application. Some selected impurity solvers related to this thesis and the work of the author are briefly highlighted in the following.

2.4.1. Exact diagonalization (ED)

The basic approach of impurity solvers based on exact diagonalization (ED) is to restrict the number of sites in the interacting system. Hence, the bath is truncated, such that the remaining system can be numerically diagonalized [15, 68, 69].[8]

Determining the impurity model parameters for a finite-size bath is a delicate step, because no unique procedure exists. Usually, the bath parameters cannot be obtained directly on the real-frequency axis, but have to be determined with a fit procedure on the Matsubara axis [15, 76]. Due to the restriction that only small systems with

[8] If all bath sites are neglected the problem reduces to finding the atomic Green's function. This approximation is known as Hubbard-I [8], which is only justified for strongly-localized systems.

10 to 20 sites in total can be treated in ED, the solution of the AIM will suffer from finite-size artifacts. Various methods improving on ED have been presented in recent years, e.g., the variational ED [77], the distributional ED [78], methods restricting the basis states [79, 80], and methods using the cluster perturbation theory [47, 81, 82].

2.4.2. Iterated perturbation theory (IPT)

One of the first approaches to solve the DMFT self-consistency equations for single-orbital models was the iterated perturbation theory (IPT) [9, 15, 83]. It is based on an expansion up to second order in U and gives an expression for the self-energy $\Sigma(i\omega_n)$ in terms of the non-interacting bath Green's function $\mathcal{G}_0(\tau)$ in imaginary time τ ($0 < \tau < \beta$ with $\beta = 1/T$ as usual)

$$\Sigma(i\omega_n) \simeq \frac{U}{2} + U^2 \int_0^\beta d\tau \; \mathcal{G}_0^2(\tau)\, \mathcal{G}_0(-\tau)\, e^{i\omega_n \tau}. \tag{2.31}$$

The first-order contribution ($U/2$) is only a constant and can be absorbed into the chemical potential μ. IPT in its original form is only suitable for half-filled systems, however extensions for problems away from half-filling and for multi-orbital models have been proposed [72, 84]. We use IPT in Sec. 2.6 to demonstrate the Mott metal-insulator transition with increasing U for the special case of a half-filled Bethe lattice.

2.4.3. Continuous-time hybridization expansion (CTHYB)

Continuous-time Monte Carlo methods (CTQMC), for a comprehensive review see Ref. [85], are based on the expansion of the impurity partition function $\mathcal{Z}$. The advantage of CTQMC solvers is that they can deal with multi-orbital impurity models, solve the impurity model at a finite inverse temperature β, and are, up to statistical errors, exact on the imaginary axis. Different formulations exist, like the weak-coupling interaction expansion (CTINT) [86] or the strong-coupling hybridization expansion (CTHYB) [75, 87]. The business of CTQMC solver development is a whole universe on its own and has lead to very sophisticated and efficient algorithms in recent years.

Specifically, in the context of multi-orbital calculations and the modeling of real materials with DMFT, the CTHYB impurity solver has become one of the most widely used methods. In this section we briefly review the underlying idea on the example of the single-orbital AIM. Extensive descriptions of the CTHYB algorithm, also with regard to the measurement of Green's functions, can be found in Refs. [75, 85, 87, 88]. Throughout this thesis we heavily use the CTHYB implementation of the TRIQS/CTHYB package [88].

We have seen above (Eq. 2.29) that the AIM Hamiltonian can be split into a local, a bath, and a hybridization part:

$$H_{AIM} = H_{loc} + H_{bath} + H_{hyb} = H_0 + H_{hyb}. \tag{2.32}$$

The partition function $\mathcal{Z}$ in the interaction picture for H_{hyb} in imaginary time, $H_{hyb}(\tau) = e^{\tau H_0}\ H_{hyb}\ e^{-\tau H_0}$, reads

$$\begin{aligned}\mathcal{Z} = \mathrm{Tr}\left[e^{-\beta H_{AIM}}\right] &= \mathrm{Tr}\left[e^{-\beta H_0}\mathcal{T}e^{-\int_0^\beta d\tau\ H_{hyb}(\tau)}\right] \\ &= \sum_{q=0}^{\infty}(-1)^q \int_0^\beta d\tau_1\ \cdots \int_{\tau_{q-1}}^\beta d\tau_q\ \mathrm{Tr}\left[e^{-\beta H_0}\mathcal{T}\prod_{i=q}^{1} H_{hyb}(\tau_i)\right],\end{aligned} \tag{2.33}$$

where q is the expansion order and $\mathcal{T}$ the time ordering operator. By writing $H_{hyb}(\tau)$ explicitly with creation and annihilation operators and subsequently integrating out the non-interacting bath operators one ends up with

$$\mathcal{Z} \sim \sum_q \int \prod_{i=1}^{q} d\tau_i\ d\tau_i' \quad \mathrm{Tr}_{imp}\left[e^{-\beta H_{loc}}\mathcal{T}\prod_{i=q}^{1} a_0^\dagger(\tau_i)a_0(\tau_i'))\right] \det_{1\leqslant i,j\leqslant q}\Delta(\tau_i - \tau_j')\ , \tag{2.34}$$

where the operator $a_0(\tau_i)$ destroys an electron at imaginary time τ_i on the impurity and the operator $a_0^\dagger(\tau_i')$ creates an electron at imaginary time τ_i' on the impurity, respectively. Eq. 2.34 can be used in Monte Carlo simulations with configurations defined by the expansion order and the imaginary times $\tau_{1\cdots q}$ and $\tau'_{1\cdots q}$. Besides the parameters to control the Monte Carlo procedure (e.g., number of measurements, number of cycles, thermalization steps,...), the necessary input of a CTHYB solver is the local Hamiltonian H_{loc} and the hybridization function $\Delta(\tau)$.

In the case of multi-orbital systems the demanding part is the evaluation of the trace. However, this effort can be greatly reduced by an (automatic) partition of the local Hilbert space and by the use of a tree structure to reuse parts of the trace calculation which do not change between configurations [88, and the references therein].

In principle, CTHYB allows to treat arbitrary interaction tensors $\tilde{U}_{\alpha\beta\gamma\delta}$ and also off-diagonal hybridization matrices ($\Delta_{ab}(\tau) \neq \delta_{ab}\Delta_{aa}(\tau)$). However, depending on the inverse temperature and the specific forms of the interaction tensor and the hybridization, the sign problem can become severe. This is caused by the fact that the sampled weights can also be negative due to the anti-commutation relation between fermionic operators, which can hinder the simulation of certain models [85]. For example, the spin-flip and pair-hopping terms present in the Slater Hamiltonian do cause a sign problem for the calculations in Chs. 5 and 6, but as it is minor it does not substantially affect the simulations.

As the impurity Green's functions are accumulated in the imaginary domain, an analytic continuation is necessary to obtain real-frequency quantities. Aspects of the analytic continuation are discussed in Sec. 2.5.

2.4.4. Fork tensor product states (FTPS)

Although the quantum Monte Carlo solvers are exact on the imaginary axis (up to statistical noise), the ill-posed nature of the analytic continuation (see Sec. 2.5) does stimulate the development of impurity solvers working directly on the real-frequency axis. Recently, the fork tensor product states (FTPS) multi-orbital impurity solver [89] was presented. The core of this impurity solver is the special tensor network representation of the many-body ground state, particularly suited for the geometry of impurity problems. In the following we give a brief outline of the underlying idea. The author's contribution to Ref. [89] is presented in Ch. 4. However, as the author of this thesis was not directly involved in the development of the impurity solver itself, we refer the interested reader to Ref. [89] for more specific details on the FTPS algorithm.

We start with the definition of matrix product states (MPS), which allow to represent quantum-mechanical states $|\psi\rangle$ of a N-site system as a product of tensors (s_i is an

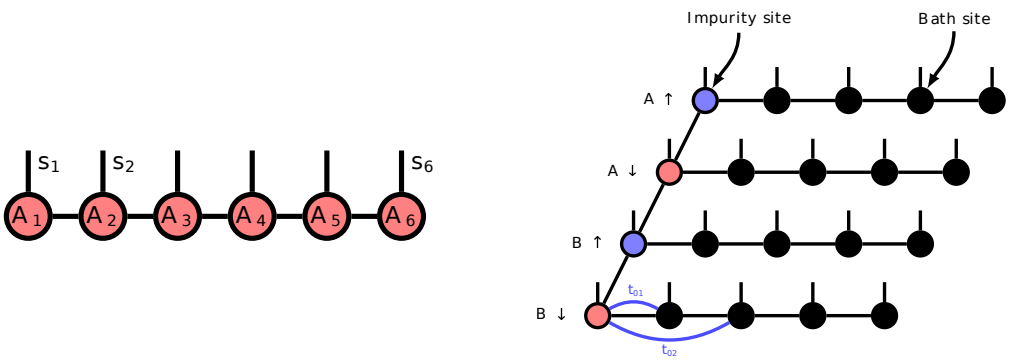

Figure 2.5.: Left: Graphical representation of an MPS. Each circle represents a tensor $A_i^{s_i}$ and each line an index of this tensor. The physical indices are the vertical lines, while the horizontal lines are internal indices (bond dimension). If a line connects two circles, the corresponding indices are summed over. Right: Graphical representation of a fork tensor product state for a two-orbital AIM with four bath sites each. In this figure the orbitals are labeled A and B and the arrows denote the spin. Note that the tensor network geometry of the bath can be linear even if the bath is discretized in star geometry. Two example hoppings t_{01} and t_{02} are drawn. Both figures are taken from Ref. [89].

index corresponding to the local basis state at site i):

$$|\psi\rangle = \sum_{s_1,\cdots,s_N} c_{s_1,\cdots,s_N} |s_1,\cdots,s_N\rangle = \sum_{s_1,\cdots,s_N} A_1^{s_1}\cdots A_N^{s_N} |s_1,\cdots,s_N\rangle \ . \tag{2.35}$$

By employing repeated singular-value decompositions, the large tensor $c_{s_1,\cdots,s_N}$ can be factorized into a product of local tensors $A_i^{s_i}$ [90].[9] The resulting tensors $A_i^{s_i}$ are of rank 3, with the exception of those with index 1 and N, which are of rank 2. In general, a state of the full Hilbert space cannot be stored, but ground states can be represented well by MPS of limited tensor dimension [91]. A graphical representation of an MPS is shown in Fig. 2.5 (left).

Usually, the AIM is treated with MPS by placing the impurity in the middle of the system and the up and down spin degrees of freedom to its left and right, respectively [92, 93]. For a D-orbital model the state space of each site then consists of D degrees of freedom with dimension 2^D. This leads to an exponential growth of the

[9] In the same way, operators can be factorized into tensor products [90].

matrix dimensions, and thus the treatment of more than two orbitals is highly unfeasible. The core idea of FTPS is to separate the bath degrees of freedom as much as possible [89]. The FTPS has impurity tensors for each orbital and spin combination and these are connected to individual bath tensors (see right graph of Fig. 2.5). Hence, not directly coupled degrees of freedom, i.e. the individual bath sites of each orbital, are not combined to a large physical index like in the standard MPS approach.

To solve the impurity problem with FTPS mainly four steps are necessary [89]:

1. Accurate discretization of the AIM directly on the real-frequency axis with a large number, $\mathcal{O}(100)$, of bath sites.

2. Setup of the tensor product operator encoding the many-body Hamiltonian.

3. Search of the variational ground state by minimizing the expectation value

$$E_0 = \min_{|\psi\rangle} \frac{\langle\psi|H|\psi\rangle}{\langle\psi|\psi\rangle} \ . \tag{2.36}$$

   This is achieved, within the density matrix renormalization group (DMRG), by moving trough the network and always updating two neighboring tensors [71, 90].

4. Calculation of the interacting Green's function, e.g. with real-time evolution.

2.5. Analytic continuation

CTQMC-based impurity solvers provide an imaginary-time Green's function $G(\tau)$ as solution to the interacting AIM. The desired physical quantity is usually the real-frequency spectral function $A(\omega)$, i.e. the retarded Green's function $G(\omega)$. Therefore, it is inevitable to perform an analytic continuation. Parts of the discussion here follow the methodology section of our recent work on the extension of the maximum entropy method (MEM) to matrix-valued Green's functions [94]. Again, we omit spin and orbital indices in this section, but note that the following equations are also valid for matrix-valued Green's functions.

We start with the connection between the spectral function $A(\omega)$ and the Green's function $G(z)$, which is explicitly given by the spectral representation

$$G(z) = \int d\omega \ \frac{A(\omega)}{z - \omega} \ , \tag{2.37}$$

which is also valid for Matsubara Green's functions

$$G(i\omega_n) = \int d\omega \ \frac{A(\omega)}{i\omega_n - \omega} \ . \tag{2.38}$$

To obtain the imaginary-time Green's function $G(\tau)$ we perform a discrete Fourier transformation

$$G(\tau) = \frac{1}{\beta} \sum_{\omega_n} e^{-i\omega_n \tau} G(i\omega_n) = \int d\omega \ \frac{1}{\beta} \sum_{\omega_n} e^{-i\omega_n \tau} \frac{A(\omega)}{i\omega_n - \omega} \ . \tag{2.39}$$

The evaluation of the Matsubara-frequency sum results in

$$G(\tau) = \int d\omega \ \frac{e^{-\omega\tau}}{e^{-\beta\omega} + 1} A(\omega) = \int d\omega \ K(\tau, \omega) A(\omega) \ , \tag{2.40}$$

where $K(\tau, \omega) = e^{-\omega\tau}/(e^{-\beta\omega} + 1)$ is the Kernel of the transformation. Eq. 2.40 provides the relationship between the imaginary-time Green's function $G(\tau)$ and the spectral function $A(\omega)$. A discretization of the functions $G(\tau)$ and $A(\omega)$ to vectors $G_n = G(\tau_n)$ and $A_m = A(\omega_m)$ leads to

$$G_n = K_{nm} A_m \ , \tag{2.41}$$

with

$$K_{nm} = \frac{e^{-\omega_m \tau_n}}{1 + e^{-\omega_m \beta}} \Delta\omega_m \ . \tag{2.42}$$

Calculating $G(\tau)$ from $A(\omega)$ is straight forward, but the inversion of Eq. 2.41, i.e. calculating $A(\omega)$ from $A_m = (K^{-1})_{mn} G_n$, is an *ill-posed* problem. To be more specific, the condition number of K is very large due to the exponential decay of K_{nm} with ω_m and τ_n, and therefore the direct inversion of K is not feasible by standard numerical techniques [95]. In practice, this problem exists even for long-running Monte Carlo calculations, as it is sensitive to the slightest noise on the data. Small changes on the Matsubara axis can have a strong effect on the resulting spectral function and influence, e.g., the shape and the position of the Hubbard bands.

The ill-posed nature of the analytic continuation has lead to the development of various methods. The most common ones are series expansions (e.g. the Padé method [95, 96]), statistical approaches such as the MEM [97–99] and stochastic methods [100–102]. Of course, all the mentioned methods have their advantages and drawbacks, and thus the choice of the analytic continuation method depends strongly on the problem at hand. For example, in Sec. 2.6 we use the Padé method together with the IPT solver, because the calculated self-energies are noise-free. For the calculations presented in Chs. 5 and 6 we employ the stochastic method by Beach [101] to continue the CTHYB data. This decision is based on two important points: First, the Padé approximation is known to give unphysical solutions for noisier data, which can violate the positiveness of $A(\omega)$. And second, the MEM spectra tend to exhibit spurious features around the Fermi energy [97], which is problematic considering the calculation of transport properties like the static conductivity and the Seebeck coefficient. Stochastic methods usually provide a better resolution of sharp spectral features and reduce spurious oscillations around the Fermi energy [101, 102], however they are computationally much more demanding then the Padé approximation and the MEM methods.

The stochastic method by Beach [101] is based on a representation of the spectral function as delta-peaks. A Monte Carlo procedure is carried out where the acceptance of new configurations is determined with the Metropolis algorithm to ensure detailed balance and ergodicity. Moves of the "delta function walkers" are shifts of peaks by a certain distance, and weight sharing moves, where the weight of a subset of walkers is redistributed among themselves. Note that these moves are such that the norm of the spectral function is preserved. The energy E of a configuration is given by a misfit. Parallel tempering is performed for multiple inverse temperature layers, where configurations are swapped between layers such that each will settle into thermal equilibrium. To obtain a final spectrum it is proposed to average over all solutions that surpass the fitting threshold $\chi^2(A(\omega)) < E^*$. On a side note, the setup of a fitting threshold can be also understood in terms of an *implicit* regularization parameter, corresponding to the α in MEM procedures.

In the framework of our DFT+DMFT calculations (see Sec. 2.7) it is necessary to perform an analytic continuation of the self-energy to obtain lattice quantities, e.g. the **k**-resolved spectral function $A(\mathbf{k}, \omega)$, Fermi surfaces, or optical properties. However, the self-energy is not a Green's function per se, and thus Eq. 2.37 is not valid correspondingly for self-energies. There are several ways to obtain the self-energy on the real-axis $\Sigma(\omega)$: First, one can perform an analytic continuation for $G_{0,imp}$ and G_{imp} and calculate $\Sigma(\omega)$ from the Dyson equation on the real-axis. Usually, this approach gives unreliable results as there are two analytic continuations and two inversions of Green's functions involved [103]. Another approach is to perform the continuation for $G_{loc}(\omega)$ and solve for $\Sigma(\omega)$ using Eq. 2.24 (with $z = \omega$) [104]. And finally, the most stable method is the construction of an auxiliary Green's function from $\Sigma(i\omega_n)$ [103, 105], which requires the following steps:

1. Construction of $G_{aux}(i\omega_n)$ from the self-energy $\Sigma(i\omega_n)$. A possible way is

$$G^{cor}_{aux}(i\omega_n) = \Sigma(i\omega_n) - \Sigma(i\omega_n \to \infty) \ , \tag{2.43}$$

   where $\Sigma(i\omega_n \to \infty)$ is the constant moment of the tail of $\Sigma(i\omega_n)$. Another option is the inversion method

$$G^{inv}_{aux}(i\omega_n) = (i\omega_n + C - \Sigma(i\omega_n))^{-1} \ . \tag{2.44}$$

   In principle, C is a free parameter, but it is usually set to $C = \Sigma^{DC} + \mu$ with the double-counting correction Σ^{DC} and the chemical potential μ.[10]

2. Analytic continuation of $G_{aux}(i\omega_n)$ to $A_{aux}(\omega)$ with the method of choice.

3. Construction of $G_{aux}(\omega)$ from $A_{aux}(\omega)$ using Eq. 2.37.

4. Calculation of $\Sigma(\omega)$ from $G_{aux}(\omega)$ with the real-frequency analog of Eq. 2.43 or Eq. 2.44, respectively.

In this thesis all analytic continuations of self-energies have been carried out with the construction of an auxiliary Green's function via the inversion method.

[10] We discuss the double-counting correction in Sec. 2.7.

2.6. The Mott transition

The physics of materials is strongly dependent on the competition between the kinetic energy of the electrons and the Coulomb repulsion [16]. This competition is expressed by the Hubbard model (Eq. 2.10). If we start from an artificial crystal with individual atoms separated by a large distance, such that they are only weakly bound together, the movement of the electrons is strongly suppressed and the system will be insulating. In the Hubbard model this corresponds to $U \gg t$. This regime, known as the atomic limit, can be best understood with the picture of localized particle-like electrons. When we move the atoms closer together, the wave functions of the electrons localized at different atoms will start to overlap. This allows the electrons to "hop" to an empty or half-filled orbital of a neighboring atom, turning the system into a metal. Of course, if an orbital is already occupied by one electron, the energy penalty U needs to be payed to maintain the double occupancy. In the itinerant limit $t \gg U$, the material is well described by conventional band theory and a wave-like electron picture.

In other words, with increasing interaction strength the electrons in a metallic material become more and more localized and eventually undergo a transition into an insulator. This interaction-driven transition, referred to as Mott metal-insulator transition [106, 107], is fundamentally different from a conventional band insulator. The characteristic features when approaching the strongly correlated regime is the emergence of low-energy quasiparticles and high-energy incoherent excitations (Hubbard bands) at the same time. The quasiparticles can be still described in a picture of wave-like particles, whereas the development of Hubbard bands is a sign for the importance of atomic-like physics.

Although both limits ($U \gg t$ and $t \gg U$) are fundamentally different, they are well described either in momentum space by band theory or by the atomic limit in real space. Obviously, the challenging task is to capture the transition from the itinerant picture to the localized one, through the $U \approx t$ regime, where electrons are neither fully itinerant nor fully localized. Notably, DMFT captures the essential physics of the Mott transition and is able to provide a bridge between the itinerant and the localized picture [15].

The simplest case to justify this claim is the half-filled single-orbital Hubbard model on the infinitely-coordinated Bethe lattice, which has a non-interacting DOS of semi-circular shape [108] (top left graph in Fig. 2.6). On the Bethe lattice the DMFT self-consistency cycle takes the particularly simple form [15]

$$G_{0,imp}^{-1}(z) = z + \mu - t^2 G_{imp}(z)\,. \tag{2.45}$$

To solve the impurity problem we use the IPT solver on the imaginary axis (Sec. 2.4.2) and perform the analytic continuation with the Padé approximation [95, 96]. The Mott transition can be best visualized by the evolution of the spectral function with increasing interaction strength. In Fig. 2.6 the spectral functions for interaction strengths from $U = 0\,\mathrm{eV}$ to $7\,\mathrm{eV}$ are shown for a non-interacting DOS with half-bandwidth $D = 2\,\mathrm{eV}$. With increasing U a characteristic three-peak structure develops, which is a mixture of emerging Hubbard bands and a quasiparticle peak centered at the chemical potential (see the second and third row in Fig. 2.6). Hence, the transition towards the insulating state appears as a transfer of spectral weight from the quasiparticle peak to the high-energy Hubbard bands. At the phase-transition point, occurring in this example at a critical U_c/D slightly lower than 3, the quasiparticle peak vanishes and only the two Hubbard bands are left. In the insulating regime the centers of the Hubbard bands are separated by an energy difference of approximately U (bottom row of Fig. 2.6).

We note that at low temperatures the Mott transition point is surrounded by a coexistence region where a metallic and an insulating solution can be stabilized [69, 109, 110]. With the IPT solver this coexistence region can be observed on the Bethe lattice between about $U_c'/D = 2.6$ and U_c/D (not shown). To which solution the DMFT cycle converges depends mainly on the starting point.

A quantitative measure for the spectral weight of the quasiparticle peak is the quasiparticle renormalization Z. Within Fermi-liquid theory, excitations created by adding a particle to the system are described by free particles with a long life time and a renormalized mass [48, 65, 66]. In this picture a gas of interacting electrons can be seen as a gas of renormalized non-interacting quasiparticles. Therefore, the quasiparticle picture is only correct if the retarded Green's function of the interacting system is similar to that of non-interacting particles around the Fermi energy. The following derivation is based on the argumentation in Ref. [66].

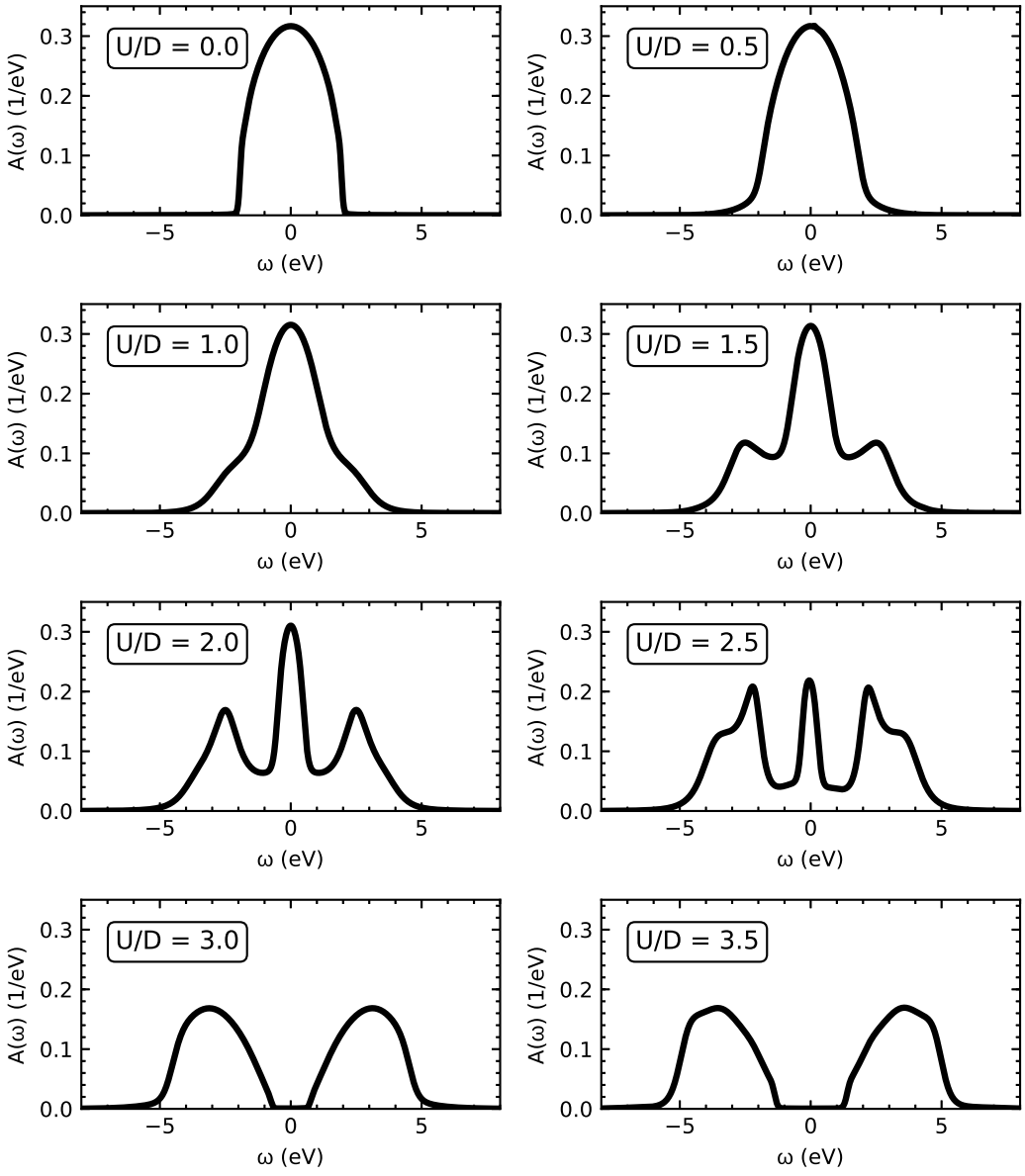

Figure 2.6.: Mott metal-insulator transition on the Bethe lattice with a semi-circular non-interacting DOS. The half bandwidth D is set to 2 eV. With increasing interaction strength U a characteristic three-peak structure emerges. At the phase transition (U_c/D slightly lower than 3) the quasiparticle peak vanishes and only the two Hubbard bands are left. For a comparison to results in the literature see, e.g., Ref. [15].

First, we consider the retarded Green's function $G(\mathbf{k},\omega)$ and separate the self-energy $\Sigma(\omega)$ into its real and imaginary parts[11]

$$G(\mathbf{k},\omega) = \frac{1}{\omega - \epsilon_{\mathbf{k}} + \mu - \Sigma(\omega)} = \frac{1}{\omega - \epsilon_{\mathbf{k}} + \mu - \Re\left[\Sigma(\omega)\right] - i\Im\left[\Sigma(\omega)\right]} \ . \tag{2.46}$$

We now expand the self-energy to the first order in ω

$$G(\mathbf{k},\omega) \approx \left[\omega - \epsilon_{\mathbf{k}} + \mu - \Re\left[\Sigma(0)\right] - \omega \frac{\partial \Re\left[\Sigma(\omega)\right]}{\partial \omega}\bigg|_{\omega=0}\right]^{-1} \ . \tag{2.47}$$

It was shown by Luttinger [111] that in the metallic regime the imaginary part of every diagram contributing to $\Sigma(\omega)$ goes to zero as $(\epsilon_{\mathbf{k}} - \mu)^2$ or faster, and thus we set $\Im\left[\Sigma(\omega)\right]$ to zero for an expansion around $\omega = 0$. Using the definitions

$$Z^{-1} \equiv 1 - \frac{\partial \Re\left[\Sigma(\omega)\right]}{\partial \omega}\bigg|_{\omega=0} \quad \text{and} \quad \tilde{\epsilon}_{\mathbf{k}} \equiv Z\left(\epsilon_{\mathbf{k}} - \Re\left[\Sigma(0)\right]\right) \ , \tag{2.48}$$

we rewrite Eq. 2.47 as

$$G(\mathbf{k},\omega) \approx \frac{Z}{\omega - \tilde{\epsilon}_{\mathbf{k}} + \mu} \ . \tag{2.49}$$

This result effectively describes non-interacting quasiparticles with the following properties provoked by the interaction: First, the spectral weight around the Fermi energy is renormalized by a factor of Z.[12] Second, also the non-interacting dispersion $\epsilon_{\mathbf{k}}$ is renormalized by a factor of Z, which corresponds to electrons gaining an effective mass of $m^* = m/Z$ due to electronic interactions. In general, Z provides a quantitative measure for correlation-induced effects, which can be summarized as:

- $U = 0 \rightarrow Z = 1$
  Uncorrelated system and hence no renormalization of the dispersion $\epsilon_{\mathbf{k}}$. The conventional band-structure picture is valid.

[11] For simplicity and with regard to the DMFT approximation, we assume here a $\mathbf{k}$-independent self-energy $\Sigma(\omega)$.

[12] As the total spectral function is normalized to one, there exists also incoherent spectral weight $(1 - Z)$, which is, however, not described by the quasiparticle approximation. The normalization also implies $1 \geqslant Z \geqslant 0$.

- $0 < U < U_c \rightarrow 1 > Z > 0$
  Renormalization due to electronic correlations. The system is in a metallic phase because of spectral weight at the Fermi energy, but the weight of the quasiparticle peak shrinks with increased U. U_c marks the critical U value of the Mott transition.

- $U \geqslant U_c \rightarrow Z = 0$
  Correlation-induced Mott insulator. The spectral weight at the Fermi energy is zero.

When using impurity solvers working on the Matsubara axis, Z can be evaluated with

$$Z^{-1} = 1 - \left.\frac{\partial \Im \left[\Sigma\left(i\omega_n\right)\right]}{\partial \omega_n}\right|_{w_n \rightarrow 0}, \tag{2.50}$$

which follows from Eq. 2.48 and the Cauchy-Riemann equations for complex functions.

2.7. A successful marriage: DFT+DMFT

One of the most successful approaches to model strongly correlated materials is the DFT+DMFT method (or LDA+DMFT) [14, 18–20]. By now, we have already discussed DFT, DMFT, and aspects related to impurity solvers. However, for DFT+DMFT a few additional ingredients are necessary, which specifically concerns the linking of DFT and DMFT with an interface layer to construct Wannier functions. These provide an appropriate basis of the (multi-orbital) Hubbard model as they resemble localized atomic-like orbitals in real space.

The basic flow chart of DFT+DMFT is schematically shown in Fig. 2.7. After an initial DFT calculation the Kohn-Sham orbitals are used to construct a localized Wannier basis in which the low-energy Hubbard model is set up. Consequently, the Hubbard model is solved with DMFT. Depending on the quantities of interest and the choice of the impurity solver, an analytic continuation might be necessary for the post-processing of the DMFT result (Secs. 2.4 and 2.5).

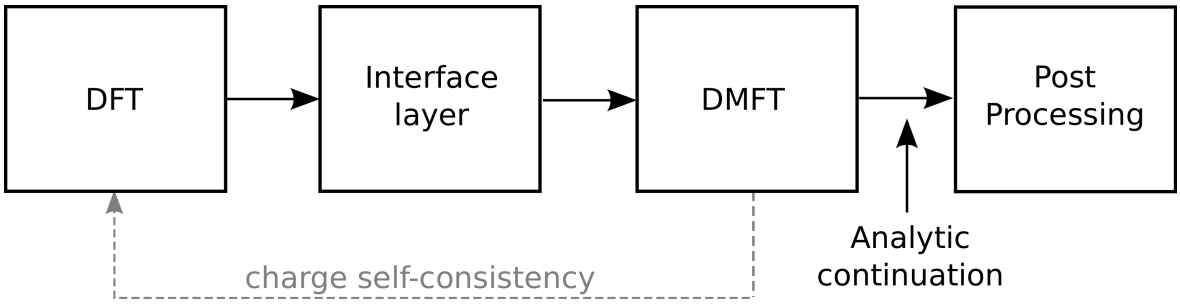

Figure 2.7.: General structure of a (fully charge self-consistent) DFT+DMFT calculation. This sketch is taken from Ref. [112].

Often only one-shot DFT+DMFT calculations are performed, where the described steps are carried out only. However, as correlations alter the charge density $n(\mathbf{r})$, these effects should be also incorporated into the Kohn-Sham potential. To this end, the interacting density matrix of the orbitals described within DMFT can be used to recalculate the DFT ground-state density, leading to a new Kohn-Sham exchange-correlation potential, and consequently also to a new Kohn-Sham eigensystem. This advanced scheme is usually referred to as fully charge self-consistent DFT+DMFT. After initially converging the DFT part, a common way to proceed in fully charge self-consistent calculations is to solve the Kohn-Sham eigensystem (Eq. 2.7) and the impurity model once in each DFT+DMFT cycle. As long as DMFT is the computationally expensive part of the calculation, the individual iterations of fully charge self-consistent DFT+DMFT are generally not much more demanding than those of one-shot calculations. As a rough guide, the additional computational effort due to an increased number of self-consistency loops necessary for convergence is normally around 50% in comparison to the one-shot scheme. Of course, this extra effort depends largely on the problem at hand and on how relevant the DMFT corrections to the charge density are. In this work we use one-shot calculations for $SrVO_3$ in Ch. 4 and for Sr_2RuO_4 in App. B. Fully charge self-consistent calculations are performed for the manganese pnictides discussed in Chs. 5 and 6.

Now we turn our focus to the construction of Wannier functions. In contrast to the Bloch wave functions, these functions are localized in real space, and therefore provide a natural basis to include local interaction. Wannier functions form an orthonormal basis set and usually resemble atomic orbitals, because they are centered on atoms

and decay with increasing distance from the nuclei. They are defined as the Fourier transform of the Bloch states $\varphi_{\mathbf{k}\nu}(\mathbf{r})$[13]

$$w_\alpha^i(\mathbf{r}) = \sum_{\mathbf{k}} e^{-i\mathbf{k}\cdot\mathbf{R}_i} \sum_\nu T_{\alpha\nu}^i \varphi_{\mathbf{k}\nu}(\mathbf{r}) \ , \tag{2.51}$$

where i is the atom index, α the orbital index, and ν the index of the Kohn-Sham band. $T_{\alpha\nu}^i$ is a unitary transformation matrix, which is not uniquely defined. One choice are the so-called *maximally localized* Wannier functions [113, 114]. Here, the elements of T are determined by minimizing the total spread

$$\Omega = \sum_{i\alpha} \left(\langle w_\alpha^i | r^2 | w_\alpha^i \rangle - \langle w_\alpha^i | \mathbf{r} | w_\alpha^i \rangle^2 \right) \ . \tag{2.52}$$

In general, only a subset of the DFT bands have a sizable orbital character of the localized shells of interest. This subset is referred to as the correlated subspace. The rest is assumed to be well described already in DFT. For each DFT+DMFT calculation the correlated subspace has to be identified by the selection of the correlated orbitals. This can be the $3d$-t_{2g} orbitals of $SrVO_3$ (Ch. 4) or the full $3d$ manifold in the case of the manganese pnictides as used in Chs. 5 and 6. The construction of maximally localized Wannier functions for the correlated subspace can be unstable and usually requires some level of user control, especially if the bands of the correlated subspace are strongly entangled with other bands.

An alternative is provided by *projective* Wannier functions, which are simple to construct and therefore beneficial for automatized fully charge self-consistent calculations [115, 116]. Projective Wannier functions are constructed from a *truncated* expansion of a set of orthonormal atomic-like orbitals $|\chi_\alpha^i\rangle$ in the Kohn-Sham basis $|\varphi_{\mathbf{k}\nu}\rangle$

$$|\chi_{\mathbf{k}\alpha}^i\rangle = \sum_{\nu\in\mathcal{W}} \langle \varphi_{\mathbf{k}\nu} | \chi_\alpha^i \rangle \, |\varphi_{\mathbf{k}\nu}\rangle \ . \tag{2.53}$$

The truncation is specified by an energy window $\mathcal{W}$, which restricts the sum over all Kohn-sham states ν to those states with Kohn-Sham energies within $\mathcal{W}$. The matrix elements of the projection operator for the correlated subspace $\nu \in \mathcal{W}$ are

$$P_{\alpha\nu}^i(\mathbf{k}) = \langle \chi_\alpha^i | \varphi_{\mathbf{k}\nu} \rangle \ . \tag{2.54}$$

[13] Again, we drop here and in the following the spin index σ.

By construction, the $|\chi^i_{\mathbf{k}\alpha}\rangle$ form only an orthonormal set if the sum in Eq. 2.53 is not truncated, and thus includes all Kohn-Sham bands. In all other cases the orbitals $|\chi^i_{\mathbf{k}\alpha}\rangle$ have to be orthonormalized, leading to orthonormalized projectors [115, 116]

$$\tilde{P}^i_{\alpha\nu}(\mathbf{k}) = \sum_{j\beta} \left[O(\mathbf{k})^{-1/2}\right]^{ij}_{\alpha\beta} P^i_{\alpha\nu}(\mathbf{k}) \ , \tag{2.55}$$

with the overlap matrix

$$O^{ij}_{\alpha\beta}(\mathbf{k}) = \sum_{\nu\in\mathcal{W}} P^i_{\alpha\nu}(\mathbf{k})\, P^{j*}_{\nu\beta}(\mathbf{k}) \ . \tag{2.56}$$

Note that the projectors $\tilde{P}^i_{\alpha\nu}(\mathbf{k})$ are only square matrices if the number of Kohn-Sham states included in $\mathcal{W}$ is equal to the number of correlated orbitals. In this work we mainly use projective Wannier functions constructed from the Wien2k basis set (linearized augmented plane wave + local orbital, i.e. LAPW+lo) [117, 118] as it is implemented in the TRIQS/DFTTools package [112, 116, 119].

For DFT+DMFT calculations it is convenient to use the Kohn-Sham basis as the complete basis set of the problem. This means that the lattice Green's function of the crystal is evaluated in the Kohn-Sham basis

$$G_{\nu\nu'}(\mathbf{k}, z) = \Big[(z - \varepsilon_{\mathbf{k}\nu} + \mu)\delta_{\nu\nu'} - \Sigma_{\nu\nu'}(\mathbf{k}, z)\Big]^{-1} \ . \tag{2.57}$$

Still, the impurity problem is formulated in the localized Wannier basis. The required local Green's function is obtained by "downfolding" to the localized Wannier basis using the orthonormalized projectors $\tilde{P}^i_{\alpha\nu}(\mathbf{k})$

$$G^i_{loc,\alpha\beta}(z) = \sum_{\mathbf{k}} \sum_{\nu\nu'} \tilde{P}^i_{\alpha\nu}(\mathbf{k}) \Big[(z - \varepsilon_{\mathbf{k}\nu} + \mu)\delta_{\nu\nu'} - \Sigma_{\nu\nu'}(\mathbf{k}, z)\Big]^{-1} \tilde{P}^{i*}_{\beta\nu'}(\mathbf{k}) \ . \tag{2.58}$$

The impurity solver provides a self-energy in the Wannier basis $\Sigma_{imp,\alpha\beta}(z)$. However, the self-energy needed in Eq. 2.57 is the self-energy defined in the Kohn-Sham space $\Sigma_{\nu\nu'}(\mathbf{k}, z)$, which is obtained by "upfolding" the impurity self-energy

$$\Sigma_{\nu\nu'}(\mathbf{k}, z) = \sum_{i,\alpha\beta} \tilde{P}^{i*}_{\alpha\nu}(\mathbf{k}) \left(\Sigma_{imp,\alpha\beta}(z) - \Sigma^{DC}\right) \tilde{P}^i_{\beta\nu'}(\mathbf{k}) \ . \tag{2.59}$$

At this point we encounter an important detail of DFT+DMFT calculations, namely the double-counting correction Σ^{DC}. This correction is necessary to avoid a double contribution of the long-range Hartree and the mean-field exchange-correlation interaction, which have been already taken into account on the level of the DFT functional. In principle, the double-counting term can be understood as an additional term

$$H_{DC} = \sum_{i\alpha} D_{i\alpha} n_{i\alpha} \ , \tag{2.60}$$

which is subtracted from the many-body Hamiltonian (Eq. 2.11). Usually, the double counting is set to be the same for all orbitals ($D_{i\alpha} = D$). Since D cannot be rigorously determined from the DFT functional, only approximative schemes are available [56]. Two common ones are:[14]

1. Around mean field (AMF): The correlations included in DFT are assumed to be of mean-field character, which gives a double-counting correction of [124]

$$D^{AMF} = UN - JN_\sigma - \frac{N_\sigma}{2l+1}\left(U - J\right) \ , \tag{2.61}$$

   where N is the total number of particles in the correlated subspace, N_σ the number of particles per spin, and $2l + 1$ the number of correlated orbitals.

2. Fully localized limit (FLL): This correction is derived from the assumption of atoms separated such that no hybridization between them is present (atomic limit). The exact diagonalization of the atomic Hamiltonian leads to a double-counting correction of [125]

$$D^{FLL} = U(N - \frac{1}{2}) - J(N_\sigma - \frac{1}{2}) \ . \tag{2.62}$$

   Also, a variant of the FLL correction for Kanamori Hamiltonians exists [126].

In models where only correlated bands are taken into account, i.e. when the number of bands in the correlated subspace is equal to the number of Wannier orbitals, the double counting acts as an effective energy shift. This shift can be absorbed into the chemical potential, which is anyhow adjusted to give the desired filling of the system. Notably,

[14] Next to these two schemes some other approximations have been proposed [120–123].

in the case of fully charge self-consistent calculation it was observed that the choice of the double counting is less crucial in comparison to the one-shot scheme [119].

One might be overwhelmed by the zoo of approximations necessary to end up with a method capable of modeling strongly correlated materials. To mention them (without guarantee of completeness): the choice of the DFT functional, the construction of a Hubbard model in a selected Wannier basis, the determination of interaction parameters (U and J), the approximation of the self-energy as a local quantity, the double-counting correction, and the ill-posed analytic continuation when using CTQMC impurity solvers. And yet, these approximations seem to be very reasonable as proven by a wide range of insights into the nature of strongly correlated materials provided by DFT+DMFT calculations. Furthermore, the development of sophisticated computer codes, like the TRIQS software package [88, 112, 127], have drastically simplified the application of DFT+DMFT for the modeling of strongly correlated materials.

3. Transport properties

Preamble

In this chapter we focus on the evaluation of transport quantities within linear response theory. On the example of the optical conductivity, we show in Sec. 3.2 how an expression in the limit of infinite dimensionality can be derived by starting from the Kubo formula (based on the comprehensive discussions in Refs. [66, 128, 129]). Importantly, the resulting formulae prove to be especially useful in the context of real-material calculations, because they provide a simple way to obtain transport quantities in a post-processing step to DFT+DMFT [15, 19, 112, 130, 131].

The author of this thesis is responsible for the implementation of the TRIQS/DFTTools transport code [112], which is in parts based on an earlier work by X. Deng. Details of this transport code are discussed in Sec. 3.4.

3.1. Linear response

We are interested in the response of a system to an external perturbation. If this perturbation is low in magnitude it is usually assumed that the responding signal is directly proportional to the intensity of the perturbation. Here, we focus on the presence of an external electric field E_{ext}, a magnetic field B_{ext}, or a temperature gradient ∇T, which can all lead to a response in the electrical current j. Additionally, external perturbations can cause a redistribution of charge carriers and in turn other (internal) fields are created. We assume that the induced current is proportional to

the *total* fields E and B present in a material. The current response in direction $\alpha \in \{x, y, z\}$ is given in first order of the perturbation, i.e. in linear response, by

$$j^{\alpha} = \sigma^{\alpha\alpha'} E^{\alpha'} + \sigma^{\alpha\beta} S^{\beta\alpha'} \nabla^{\alpha'} T + \sigma_H^{\alpha\alpha'\alpha''} E^{\alpha'} B^{\alpha''} \ , \tag{3.1}$$

where σ is the conductivity tensor, S the Seebeck tensor (or thermoelectric power), and σ_H the Hall conductivity tensor. A sum over double indices, here α', α'' and β, is implied. In principle, σ and S are tensors of rank 2 and σ_H is a rank-3 tensor, however crystal symmetries can impose a restriction on the individual entries. For example, in a cubic system the response is isotropic and rank-2 tensors are diagonal with $\sigma^{\alpha\alpha'} = \delta_{\alpha\alpha'}\sigma_0$.

Of course, also time-dependent perturbations can be considered. For an electric field with a single $(\mathbf{q}, \Omega)$-mode

$$E^{\alpha'}(\mathbf{r}, t) = E_0^{\alpha'} e^{i(\mathbf{q}\mathbf{r} - \Omega t)} \ , \tag{3.2}$$

the current in linear response theory is given by ($\nabla T = 0$ and $B = 0$)

$$j^{\alpha}(\mathbf{r}, t) = \int dr' \int_{-\infty}^{t} dt' \ \sigma^{\alpha\alpha'}(\mathbf{r} - \mathbf{r}', t - t') \, E^{\alpha'}(\mathbf{r}', t') \ , \tag{3.3}$$

or correspondingly in Fourier space

$$j^{\alpha}(\mathbf{q}, \Omega) = \sigma^{\alpha\alpha'}(\mathbf{q}, \Omega) \, E^{\alpha'}(\mathbf{q}, \Omega) \ . \tag{3.4}$$

Here, we have already assumed that the response is a function of $\mathbf{r} - \mathbf{r}'$, i.e. $\sigma^{\alpha\alpha'}(\mathbf{r}, \mathbf{r}', t - t') = \sigma^{\alpha\alpha'}(\mathbf{r} - \mathbf{r}', t - t')$. This is justified if we average over many unit cells and if the perturbation wavelength is large in comparison to the typical length scales in a solid [128]. In other words, we are only interested in the limit of long wavelength excitations ($\mathbf{q} \to 0$), also know as the dipole approximation. Then, the optical conductivity tensor dependents only on the external frequency Ω

$$j^{\alpha}(\Omega) = \sigma^{\alpha\alpha'}(\Omega) \, E^{\alpha'}(\Omega) \ . \tag{3.5}$$

In the optical-frequency regime this is a well-justified approximation, since photons do not transfer momentum to the electrons. We would like to mention that other optical

quantities, e.g. the dielectric function or the reflectivity, can be directly derived from the optical conductivity [48, 66, 128].

We stated in Eq. 3.1 that a temperature gradient ∇T induces an electric current. This can be made plausible by the following simple picture [48]: Imagine a material with a hot end and a cold end. At the hot end thermal fluctuations of electrons will be stronger in comparison to the cold end. Consequently, more electrons occupy energy levels above the Fermi energy on the hot end and these "high-energy" electrons will start to diffuse from the hot end to the cold one. However, electrons occupying levels below the Fermi energy will be drawn from the cold end towards to hot end. These are two competing processes and a total current can only flow if one is stronger than the other. For this to be possible, an asymmetry has to be present on a microscopical level, which might be found in the density of states (DOS), the scattering times or the velocities of the charges.[15] Under open-circuit conditions no net current can flow, and thus the electrons will only diffuse until enough charge has accumulated on one end of the sample to build up a counteracting electric field. We realize that, when this steady-state is reached, the result of the temperature gradient is a thermoelectric field, which was experimentally first observed nearly 200 years ago by T. Seebeck [132]. By setting the current j^α and the magnetic field $B^{\alpha''}$ to zero in Eq. 3.1, we obtain

$$E^\alpha = -S^{\alpha\alpha'}\nabla^{\alpha'}T \ . \tag{3.6}$$

Without an external current flowing, i.e. without external electric field, the Seebeck tensor connects an (applied) temperature gradient to the induced electric field. Note that, within thermodynamics, the Seebeck coefficient can be understood as the entropy transported per charge carrier [133].

The third term in Eq. 3.1 is responsible for the Hall effect, which describes the induced electric field observed when an electrical current flows through a material under the presence of a magnetic field [48, 134]. Due to the magnetic field the charge carriers experience the Lorentz force, which bends their, otherwise straight, path between scattering events. The consequence is an asymmetric distribution of carriers across the sample with charges accumulating on one side. In the steady-state no current can flow

[15] In our work we focus only on electronic effects, but of course also the lattice degrees of freedoms can have an influence on the heat transport in a material.

in the direction perpendicular to the applied current and the magnetic field, which results, like in the case of a temperature gradient, in a counteracting electric field caused by the charge separation. Given a current applied in x direction and a magnetic field pointing in z direction, the Hall number R_H is defined as

$$R_H^{xyz} = \frac{E^y}{j^x B^z} \ , \tag{3.7}$$

with the induced electric field in y direction E^y. Eq. 3.7 can be expressed in terms of σ and σ_H (following from Eq. 3.1 with $j^y = 0$)

$$R_H^{xyz} = \left(\sigma^{-1}\right)^{iy} \sigma_H^{jiz} \left(\sigma^{-1}\right)^{xj} \ . \tag{3.8}$$

When the crystal symmetry demands $\sigma^{xy} = 0$, the Hall number R_H reduces to

$$R_H = \frac{\sigma_H^{xyz}}{\sigma^{xx}\sigma^{yy}} \ . \tag{3.9}$$

We will not further elaborate on the Hall effect in the main part of this thesis, but we point the reader to App. B on Sr_2RuO_4, where we discuss the temperature dependent sign of R_H observed in this compound.

3.2. Optical conductivity in d $\rightarrow \infty$

In this section we review the derivation of the optical conductivity $\sigma^{\alpha\alpha'}(\Omega)$ in the limit of infinite dimensionality ($d \rightarrow \infty$). The first part (up to Eq. 3.23) follows the derivation presented in Refs. [129, 135]. We directly start from the explicit expression for the "paramagnetic" contribution[16] to the optical conductivity within the Kubo formalism [136] (see, e.g., the textbooks by Mahan [128] or Bruus and Flensberg [66] for a derivation of the Kubo formula)[17]

$$\sigma^{\alpha\alpha'}(\mathbf{q},\Omega) = \frac{1}{V\Omega} \int_{-\infty}^{t} dt' \ e^{i\Omega(t-t')} \left\langle \left[j^{\alpha}\left(-\mathbf{q},t\right), j^{\alpha'}\left(\mathbf{q},t'\right) \right] \right\rangle \ . \tag{3.10}$$

[16] The "diamagnetic" term is given by $\sigma_{dia}^{\alpha\alpha'}(\Omega) = i\frac{n_0}{\Omega}\delta_{\alpha\alpha'}$, where n_0 is the average electron density [128]. We omit this term as it does not contribute to the real part of the optical conductivity.

[17] Like in the previous chapter we use again atomic units.

The symbol $\langle \cdots \rangle$ denotes the thermal expectation value of the unperturbed system and V is the unit cell volume. Basically, the Kubo formula expresses the optical conductivity $\sigma^{\alpha\alpha'}(\mathbf{q},\Omega)$ in terms of a current-current correlation function. Using the homogeneity of time and the previously discussed long wavelength limit $\mathbf{q} \to 0$, we obtain

$$\sigma^{\alpha\alpha'}(\Omega) = \frac{1}{V\Omega} \int_0^\infty dt\ e^{i\Omega t} \left\langle \left[j^\alpha(t), j^{\alpha'}(0) \right] \right\rangle \ . \tag{3.11}$$

By defining the current-current correlation function as

$$\chi^{\alpha\alpha'}(t) = -\frac{i}{V} \left\langle \left[j^\alpha(t), j^{\alpha'}(0) \right] \right\rangle \ , \tag{3.12}$$

we rewrite the optical conductivity as

$$\sigma^{\alpha\alpha'}(\Omega) = \frac{i}{\Omega} \int_0^\infty dt\ e^{i\Omega t} \chi^{\alpha\alpha'}(t) = \frac{i}{\Omega} \chi^{\alpha\alpha'}(\Omega) \ , \tag{3.13}$$

and hence the real part of the optical conductivity is

$$\sigma_R^{\alpha\alpha'}(\Omega) := \Re \left[\sigma^{\alpha\alpha'}(\Omega) \right] = -\frac{1}{\Omega} \Im \left[\chi^{\alpha\alpha'}(\Omega) \right] \ . \tag{3.14}$$

Now we switch to imaginary time τ, where the current-current correlation function reads

$$\chi^{\alpha\alpha'}(\tau) = -\frac{1}{V} \left\langle \mathcal{T} j^\alpha(\tau)\ j^{\alpha'}(0) \right\rangle \ . \tag{3.15}$$

To proceed, we shall define the current operator in imaginary time as [66, 128]

$$j^\alpha(\tau) = \sum_{\mathbf{k},\nu\nu',\sigma} v^\alpha_{\nu\nu',\sigma}(\mathbf{k})\, c^\dagger_{\nu,\sigma}(\mathbf{k},\tau)\, c_{\nu',\sigma}(\mathbf{k},\tau) \ . \tag{3.16}$$

The velocities $v^\alpha_{\nu\nu',\sigma}$ are matrices in the band indices ν, ν' given by

$$v^\alpha_{\nu\nu',\sigma}(\mathbf{k}) = \langle \varphi^\sigma_{\mathbf{k}\nu} | p^\alpha | \varphi^\sigma_{\mathbf{k}\nu'} \rangle = -i \langle \varphi^\sigma_{\mathbf{k}\nu} | \nabla^\alpha | \varphi^\sigma_{\mathbf{k}\nu'} \rangle \ , \tag{3.17}$$

with p^α being the α-component of the momentum operator. The $|\varphi^\sigma_{\mathbf{k}\nu}\rangle$ are a complete set of one-electron basis functions, in our cases the Kohn-Sham bands. We continue, in the following, with the evaluation of Eq. 3.15 by using the definition of the current

operator (Eq. 3.16) to obtain

$$\chi^{\alpha\alpha'}(\tau) = -\frac{1}{V}\sum_{\mathbf{k},\nu\nu',\sigma}\sum_{\mathbf{k}',\kappa\kappa',\sigma'} v^{\alpha}_{\nu\nu',\sigma}(\mathbf{k})\, v^{\alpha'}_{\kappa\kappa',\sigma'}(\mathbf{k}') \times \left\langle \mathcal{T} c^{\dagger}_{\nu,\sigma}(\mathbf{k},\tau)\, c_{\nu',\sigma}(\mathbf{k},\tau)\, c^{\dagger}_{\kappa,\sigma'}(\mathbf{k}',0)\, c_{\kappa',\sigma'}(\mathbf{k}',0)\right\rangle \ . \quad (3.18)$$

In general, $\chi^{\alpha\alpha'}(\tau)$ is a two-particle quantity, because the expectation values comprise four fermionic operators. Nevertheless, it can be shown that in the single-orbital case and in the limit of infinite dimensionality ($d \to \infty$), the current-current correlation function $\chi^{\alpha\alpha'}(\tau)$ reduces to a product of two single-particle Green's functions defined (in imaginary time) as $G_{\nu\nu',\sigma}(\mathbf{k},\tau) = -\left\langle c_{\nu,\sigma}(\mathbf{k},\tau)\ c^{\dagger}_{\nu',\sigma}(\mathbf{k},0)\right\rangle$ [15, 137–139].[18] Or to put it differently, all vertex corrections drop out in the evaluation of $\mathbf{q} = 0$ correlation functions in infinite dimensions and only the particle-hole bubble diagram gives a contribution. This observation is not strictly true in the multi-orbital case, however in the interest of practicability, vertex corrections are usually neglected in the context of realistic DFT+DMFT calculations [135]. If we take only the bubble diagram into account in Eq. 3.18, we end up with [15, 129]

$$\chi^{\alpha\alpha'}(\tau) = -\frac{1}{V}\sum_{\mathbf{k}}\sum_{\nu\nu'\kappa\kappa'}\sum_{\sigma} v^{\alpha}_{\nu\nu',\sigma}(\mathbf{k})\, G_{\nu'\kappa,\sigma}(\mathbf{k},\tau)\, v^{\alpha'}_{\kappa\kappa',\sigma}(\mathbf{k})\, G_{\kappa'\nu,\sigma}(\mathbf{k},-\tau) \ , \quad (3.19)$$

or in matrix formulation

$$\chi^{\alpha\alpha'}(\tau) = -\frac{N_\sigma}{V}\sum_{\mathbf{k}} \mathrm{Tr}\left(v^{\alpha}(\mathbf{k})\, G(\mathbf{k},\tau)\, v^{\alpha'}(\mathbf{k})\, G(\mathbf{k},-\tau)\right) \ . \quad (3.20)$$

We imply with the trace that the velocities $v^{\alpha}(\mathbf{k})$ and the Green's functions $G(\mathbf{k},\tau)$ are matrices in the band indices ν, ν'. The factor N_σ takes into account the spin degeneracy in the case of non-spin-polarized calculations. A Fourier transform of Eq. 3.20 leads to (see Ref. [129] for the detailed steps)

$$\chi^{\alpha\alpha'}(i\Omega_n) = -\frac{N_\sigma}{V}\sum_{\mathbf{k}}\int d\omega \int d\omega' \frac{f(\omega') - f(\omega)}{\omega - \omega' + i\Omega_n} \times \mathrm{Tr}\left(v^{\alpha}(\mathbf{k})\, A(\mathbf{k},\omega')\, v^{\alpha'}(\mathbf{k})\, A(\mathbf{k},\omega)\right) \ , \quad (3.21)$$

[18] Here, and in the following, we assume that the Green's function does not have off-diagonal elements in the spin indices.

where $f(\omega)$ is the Fermi function and $A(\mathbf{k}, \omega)$ the $\mathbf{k}$-resolved spectral function as defined in Eq. 2.18. After an analytic continuation ($i\Omega_n \to \Omega + i0^+$) of Eq. 3.21, we finally obtain from Eq. 3.14 the real part of the frequency-dependent optical conductivity

$$\sigma_R^{\alpha\alpha'}(\Omega) = N_\sigma \pi \int d\omega \; \Gamma^{\alpha\alpha'}(\omega + \Omega, \omega) \; \frac{f(\omega) - f(\omega + \Omega)}{\Omega} \; . \tag{3.22}$$

In Eq. 3.22 we have used the transport distribution $\Gamma^{\alpha\alpha'}$ defined as

$$\Gamma^{\alpha\alpha'}(\omega_1, \omega_2) = \frac{1}{V} \sum_k \mathrm{Tr} \left(v^\alpha(\mathbf{k}) A(\mathbf{k}, \omega_1) v^{\alpha'}(\mathbf{k}) A(\mathbf{k}, \omega_2) \right) \; . \tag{3.23}$$

The spectral function $A(\mathbf{k}, \omega)$ is the interacting (correlated) spectral function; this is also where the $\mathbf{k}$-independent self-energy from DFT+DMFT enters. The velocities $v^\alpha(\mathbf{k})$ are unchanged by the interaction. With those two quantities at hand, the transport distribution (Eq. 3.23) can be evaluated in a post-processing step to DFT+DMFT (see Sec. 3.4). It should be kept in mind that in multi-band systems the velocities $v^\alpha_{\nu\nu'}(\mathbf{k})$ and the spectral function $A_{\nu\nu'}(\mathbf{k}, \omega)$ are Hermitian matrices in the Kohn-Sham band indices ν, ν'.

The approximations required to derive Eq. 3.22 are (i) the use of linear response theory, i.e. the Kubo formalism, (ii) the assumption of a homogeneous system $\sigma(\mathbf{r}, \mathbf{r}') = \sigma(\mathbf{r} - \mathbf{r}')$, (iii) the dipole approximation $\mathbf{q} = 0$ and (iv) the neglect of vertex corrections. In principle, the formalism is not limited to local self-energies and could be generalized to $\mathbf{k}$-dependent $\Sigma(\mathbf{k}, \omega)$. In such cases one would need to take vertex corrections to the particle-hole bubble into account.

In the limit $\Omega \to 0$ (using L'Hospital) Eq. 3.22 reduces to the static conductivity[19]

$$\sigma_R^{\alpha\alpha'} = N_\sigma \pi \int d\omega \; \left(-\frac{\partial f(\omega)}{\partial \omega} \right) \Gamma^{\alpha\alpha'}(\omega, \omega) \; . \tag{3.24}$$

This static transport integral can be generalized with the kinetic coefficients

$$K_n^{\alpha\alpha'} = N_\sigma \pi \int d\omega \; (\beta\omega)^n \left(-\frac{\partial f(\omega)}{\partial \omega} \right) \Gamma^{\alpha\alpha'}(\omega, \omega) \; . \tag{3.25}$$

[19] In practice, the derivative of the Fermi function is expressed as $\partial f(\omega)/\partial\omega = -\beta f(\omega) f(-\omega)$.

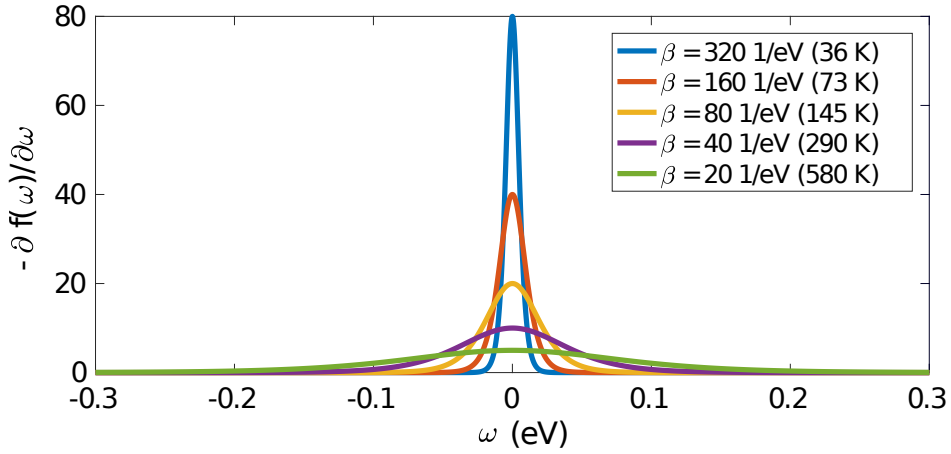

Figure 3.1.: Dependence of the Fermi function derivative $-\partial f(\omega)/\partial\omega$ on the inverse temperature β.

Then, the conductivity $\sigma_R^{\alpha\alpha'}$ and the Seebeck tensor $S^{\alpha\alpha'}$ are defined as [128]

$$\sigma_R^{\alpha\alpha'} = K_0^{\alpha\alpha'} \qquad \text{and} \qquad S^{\alpha\alpha'} = -\left(K_0^{-1}\right)^{\alpha\gamma} K_1^{\gamma\alpha'} \,. \tag{3.26}$$

We note that the coefficient K_1 follows from a current-heat-(current) correlation function. For a crystal symmetry demanding diagonal rank-2 tensors, like it is the case for all materials studied in this work, the Seebeck coefficient in direction α is given by

$$S^{\alpha} = -\frac{K_1^{\alpha\alpha}}{K_0^{\alpha\alpha}} = -\frac{K_1^{\alpha\alpha}}{\sigma_R^{\alpha\alpha}} \,. \tag{3.27}$$

We have pointed out previously that the Seebeck coefficient is a result of asymmetries in the properties of the electronic carriers. This fact is reflected by Eq. 3.26, because $K_1^{\alpha\alpha'}$ is nothing else but the first moment of the transport distribution $\Gamma^{\alpha\alpha'}(\omega,\omega)$, and thus measures its degree of electron-hole asymmetry. As the velocities $v^{\alpha}(\mathbf{k})$ and the spectral function $A(\mathbf{k},\omega)$ enter $\Gamma^{\alpha\alpha'}(\omega,\omega)$, such an asymmetry can be present in either or both of them. The Seebeck coefficient can have either sign, where the sign indicates the charge of the conducting carriers.[20]

[20] In multi-band systems holes and electrons can contribute to the Seebeck coefficient, and then the sign is the result of averaging the individual contributions (see App. B).

For the Hall conductivity σ_H no multi-band formalism has been derived so far. However, a single-band version exists, which we discuss in App. B.

Finally, we point out that the static transport quantities are sensitive to the details of the Fermi surface, as the Fermi function in Eq. 3.25 selects a temperature-dependent energy window around the Fermi energy (Fig. 3.1). We also see, depending on the temperature, that the information of the spectral function in an energy window around the Fermi energy will have an influence on the static transport quantities. When lowering the temperature this energy window narrows until only the Fermi surface becomes the decisive factor in the limit $T \to 0\,\mathrm{K}$.

3.3. Connection to Boltzmann theory

In this section we show that the kinetic coefficients (Eq. 3.25) reduce to Boltzmann transport theory, when we (i) use the constant scattering time τ_s (const.-τ_s) approximation, i.e. set $\Sigma_{\nu\nu'}(\mathbf{k},\omega) = -i/\tau_s$, and (ii) approximate the general velocity matrices $v^{\alpha}_{\nu\nu'}(\mathbf{k})$ by the simpler group velocities $\tilde{v}^{\alpha}_{\nu\nu'}(\mathbf{k}) = \partial\epsilon^{\nu}_{\mathbf{k}}/\partial k^{\alpha}$ obtained from the derivative of the dispersion $\epsilon^{\nu}_{\mathbf{k}}$.

First, we discuss the relation between $v^{\alpha}_{\nu\nu'}(\mathbf{k})$ and $\tilde{v}^{\alpha}_{\nu\nu'}(\mathbf{k})$. Using the Bloch theorem $|\varphi_{\mathbf{k}\nu}\rangle = e^{i\mathbf{kr}}\,|u_{\mathbf{k}\nu}\rangle$ the elements of the full velocity matrices $v^{\alpha}_{\nu\nu}(\mathbf{k})$ are given by (cf. 3.17)

$$\begin{aligned} v^{\alpha}_{\nu\nu'}\left(\mathbf{k}\right) &= -i\langle u_{\mathbf{k}\nu}|e^{-i\mathbf{kr}}\nabla^{\alpha}e^{i\mathbf{kr}}|u_{\mathbf{k}\nu'}\rangle = \\ &= \langle u_{\mathbf{k}\nu}|\left(-i\nabla^{\alpha}+k^{\alpha}\right)|u_{\mathbf{k}\nu'}\rangle = \langle u_{\mathbf{k}\nu}|\frac{\partial H_0\left(\mathbf{k}\right)}{\partial k^{\alpha}}|u_{\mathbf{k}\nu'}\rangle\ , \end{aligned} \tag{3.28}$$

where we have used $H_0\left(\mathbf{k}\right) = \frac{1}{2}\left(-i\nabla+\mathbf{k}\right)^2$ for the single-particle Hamiltonian. Rewriting the right hand expression of Eq. 3.28 leads to

$$\begin{aligned} \langle u_{\mathbf{k}\nu}|\frac{\partial H_0\left(\mathbf{k}\right)}{\partial k^{\alpha}}|u_{\mathbf{k}\nu'}\rangle &= \frac{\partial\langle u_{\mathbf{k}\nu}|H_0\left(\mathbf{k}\right)|u_{\mathbf{k}\nu'}\rangle}{\partial k^{\alpha}} \\ &\quad -\langle\partial u_{\mathbf{k}\nu}/\partial k^{\alpha}|H_0\left(\mathbf{k}\right)|u_{\mathbf{k}\nu'}\rangle - \langle u_{\mathbf{k}\nu}|H_0\left(\mathbf{k}\right)|\partial u_{\mathbf{k}\nu'}/\partial k^{\alpha}\rangle\ . \end{aligned} \tag{3.29}$$

In this equation we identify the first term on the right hand side as $\tilde{v}^{\alpha}_{\nu\nu'}(\mathbf{k})$, because it simplifies to

$$\frac{\partial \langle u_{\mathbf{k}\nu} | H_0(\mathbf{k}) | u_{\mathbf{k}\nu'} \rangle}{\partial k^{\alpha}} = \delta_{\nu\nu'} \frac{\partial \epsilon^{\nu}_{\mathbf{k}}}{\partial k^{\alpha}} = \tilde{v}^{\alpha}_{\nu\nu'}(\mathbf{k}) \ . \tag{3.30}$$

The $|u_{\mathbf{k}\nu}\rangle$ are the eigenstates and the $\epsilon^{\nu}_{\mathbf{k}}$ are the eigenenergies of $H_0(\mathbf{k})$. As $\tilde{v}^{\alpha}_{\nu\nu'}(\mathbf{k})$ is diagonal, possible inter-band elements are neglected, which are given by the terms in the second line of Eq. 3.29. As a consequence of the Hellmann–Feynman theorem [140] these terms are zero for the diagonal elements ($\nu = \nu'$), and thus we find $v^{\alpha}_{\nu\nu}(\mathbf{k}) = \tilde{v}^{\alpha}_{\nu\nu}(\mathbf{k})$. On a side note, the velocities $\tilde{v}^{\alpha}_{\nu\nu'}(\mathbf{k})$ can be directly obtained from the dispersion $\epsilon^{\nu}_{\mathbf{k}}$ without an explicit knowledge of the basis functions.

Within the two approximations given above, the matrices in the transport distribution (Eq. 3.23) are diagonal and the matrix multiplications and the trace reduce to a sum over band indices ν. The kinetic coefficients are written as

$$\tilde{K}^{\alpha\alpha'}_{n} = \frac{N_{\sigma}\pi}{V} \int d\omega \ (\beta\omega)^n \left(-\frac{\partial f(\omega)}{\partial \omega} \right) \sum_{\nu} \sum_{\mathbf{k}} \frac{\partial \epsilon^{\nu}_{\mathbf{k}}}{\partial k^{\alpha}} \frac{\partial \epsilon^{\nu}_{\mathbf{k}}}{\partial k^{\alpha'}} A_{\nu\nu}(\mathbf{k}, \omega)^2 \ . \tag{3.31}$$

For a single-band model Eq. 3.31 and Eq. 3.25 are equivalent. For multi-band systems, Eq. 3.31 only takes into account the intra-band transitions but neglects possible inter-band contributions.

In principle, the scattering time τ_s depends on the band index and the $\mathbf{k}$-direction. However, in the simplest approximation, often used in practice (e.g. by the BoltzTraP code [141]), τ_s is assumed to be direction-independent (isotropic) and constant.[21] Within the const.-τ_s approximation, the spectral function reads

$$A_{\nu\nu}(\mathbf{k}, \omega) = \frac{1}{\pi} \frac{\frac{1}{\tau_s}}{\left(\omega - \epsilon^{\nu}_{\mathbf{k}}\right)^2 + \frac{1}{\tau_s^2}} \ , \tag{3.32}$$

where we have set the chemical potential to $\mu = 0$. For each $\mathbf{k}$-point $A_{\nu\nu}(\mathbf{k}, \omega)$ is described by a Lorentzian centered at $\epsilon^{\nu}_{\mathbf{k}}$. For a large τ_s the Lorentzian becomes narrow in energy, and therefore we further approximate the kinetic coefficient (Eq. 3.31) as

$$\tilde{K}^{\alpha\alpha'}_{n} \approx \frac{N_{\sigma}\pi}{V} \sum_{\nu} \sum_{\mathbf{k}} (\beta\epsilon^{\nu}_{\mathbf{k}})^n \left(-\frac{\partial f(\omega)}{\partial \omega} \right)\Bigg|_{\omega=\epsilon^{\nu}_{\mathbf{k}}} \frac{\partial \epsilon^{\nu}_{\mathbf{k}}}{\partial k^{\alpha}} \frac{\partial \epsilon^{\nu}_{\mathbf{k}}}{\partial k^{\alpha'}} \int d\omega \ A_{\nu\nu}(\mathbf{k}, \omega)^2 \ . \tag{3.33}$$

[21] This approximation is usually not justified for strongly correlated systems, where the self-energy can show a substantial dependence on the orbitals and ω.

The remaining ω-integral over $A_{\nu\nu}(\mathbf{k},\omega)^2$ is

$$\begin{aligned}\int d\omega\ A_{\nu\nu}(\mathbf{k},\omega)^2 &= \frac{1}{\pi^2\tau_s^2}\int d\omega\ \frac{1}{\left(\left(\omega-\epsilon_{\mathbf{k}}^{\nu}\right)^2+\frac{1}{\tau_s^2}\right)^2} \\ &= \frac{1}{\pi^2\tau_s^2}\int dx\ \frac{1}{x^2+\frac{1}{\tau_s^2}} = \frac{1}{\pi^2\tau_s^2}\frac{\pi\tau_s^3}{2} = \frac{\tau_s}{2\pi}\ ,\end{aligned} \tag{3.34}$$

which brings us to the final equation for the kinetic coefficient

$$\tilde{K}_n^{\alpha\alpha'} \approx \frac{N_\sigma}{2V}\sum_{\nu}\sum_{k}\left(\beta\epsilon_{\mathbf{k}}^{\nu}\right)^n\left(-\frac{\partial f\left(\omega\right)}{\partial\omega}\right)\Big|_{\omega=\epsilon_{\mathbf{k}}^{\nu}}\frac{\partial\epsilon_{\mathbf{k}}^{\nu}}{\partial k^{\alpha}}\frac{\partial\epsilon_{\mathbf{k}}^{\nu}}{\partial k^{\alpha'}}\ \tau_s\ . \tag{3.35}$$

Eq. 3.35 is equivalent to the kinetic coefficients obtain within Boltzmann transport theory (see, e.g., Refs. [142–145, and the references therein]). We emphasize that the Seebeck coefficient is independent of τ_s in the const.-τ_s approximation, since τ_s cancels in $\tilde{K}_1/\tilde{K}_0$.

3.4. TRIQS/DFTTools transport code

The TRIQS (Toolbox for Research on Interacting Quantum Systems) project provides high-level, efficient and simple-to-use core libraries, written in C++ and wrapped in Python, to study interacting quantum systems [127]. Based on the library full-fledged applications, like the TRIQS/CTHYB solver [88], the TRIQS/HubbardI solver, TRIQS/SOM for stochastic analytic continuation, and the TRIQS/DFTTools [112] have been developed. The TRIQS library itself and its applications are open-source and distributed under the GPLv3 license.

Specifically, the TRIQS/DFTTools package provides methods to combine DFT band-structure calculations with DMFT. To this end, the TRIQS/DFTTools package defines a common interface to DFT codes, constructs projective Wannier functions and implements converters for Wien2k [117, 118, 146], VASP [147–150], Wannier90 [151], and generic $H(\mathbf{k})$. The package provides the necessary tools to perform the DMFT self-consistency cycle, and additionally offers multiple post-processing tools, such as

$A(\mathbf{k}, \omega)$ plotting or the calculation of transport properties. Putting the provided tools together to a working script is the task of the user; luckily, performing a simple DMFT calculation only requires a few lines of Python code. Additionally, an extensive user guide, a reference guide and tutorials are available online.[22]

An important part of this thesis was the embedding of a transport code into the TRIQS/DFTTools package, which allows for the calculation of optical conductivities and Seebeck coefficients based on the formalism presented in Sec. 3.2. The core task of this code is to evaluate the transport distribution (Eq. 3.23) directly in the Bloch basis, which has two important advantages: First, as outlined in Sec. 2.7, we use the Bloch basis already as a complete basis set for our DFT+DMFT calculations, and thus we can easily obtain the spectral function $A_{\nu\nu'}(\mathbf{k}, \omega)$ from Eqs. 2.18, 2.57, and 2.59. Second, we can make use of the velocity matrices provided by some DFT codes. At the moment their computation is based on the Wien2k *optics* package [146], which evaluates the elements of the momentum operator (Eq. 3.17) in the LAPW+lo basis set.[23] It should be emphasized that evaluating transport properties requires a considerably denser **k**-mesh than the one found to be sufficient for the convergence of the corresponding DFT calculation. The convergence in the number of **k**-points should be checked carefully, best on the level of the transport distribution (Eq. 3.23). To reduce the computational cost, the TRIQS/DFTTools transport code makes use of the crystal symmetries.

In the spirit of the TRIQS project, evaluating transport properties after a successful DFT+DMFT calculation is kept extremely simple. Before executing the transport code, as shown in Lst. 3.1, it is necessary to perform one Wien2k iteration on a denser **k**-grid and to run the Wien2k *optics* code. After defining the imports (lines 1-7), we set up the Converter (line 10) and read the required data of the Wien2k output (line 11 and 12), which is written into the case.h5 file. Next, we load this h5-file (line 14) and also read and set the real-frequency self-energy (lines 16 to 18). With the function `transport_distribution()`, the transport distribution is calculated (line 20 and 21), here in x direction for the frequencies $\Omega = [0.0, 0.2]\,\mathrm{eV}$ at an inverse temperature of $\beta = 40\,\mathrm{eV}^{-1}$. When using an impurity solver on the Matsubara axis at a certain inverse temperature β, one should also use the same β in the calculation of the

[22] https://github.com/TRIQS/dft_tools and https://triqs.ipht.cnrs.fr/1.x/applications/dft_tools

[23] A recent implementation published as the *woptic* package [131] also uses full velocity matrix elements, but is implemented in the framework of maximally localized Wannier functions.

transport properties. To obtain results at a different temperature, the corresponding DFT+DMFT calculation has to be performed, because also the spectral function depends on β. Finally, the function `conductivity_and_seebeck()` (line 23) evaluates the optical conductivity on the given Ω mesh (Eq. 3.22). Additionally, the Seebeck coefficient (Eqs. 3.25 and 3.26) is calculated if $\Omega = 0.0\,\mathrm{eV}$ is included in the mesh.

Listing 3.1: Code snippet showing the use of the TRIQS/DFTTools transport code (with TRIQS version 1.3).

```
1  # Necessary imports
2  from pytriqs.gf.local import *
3  from pytriqs.archive import HDFArchive
4  from pytriqs.applications.dft.converters.wien2k_converter \
5    import Wien2kConverter
6  from pytriqs.applications.dft.sumk_dft import SumkDFT
7  from pytriqs.applications.dft.sumk_dft_tools import SumkDFTTools
8
9  # Create Converter object and convert Wien2k optics files
10 Converter = Wien2kConverter(filename='case')
11 Converter.convert_dft_input()
12 Converter.convert_transport_input()
13 # Create Sumk object
14 SK = SumkDFTTools(hdf_file='case.h5')
15 # Set Sigma in SK object
16 ar = HDFArchive('Sigma.h5','r')
17 SK.set_Sigma(Sigma_imp = [ar['Sigma_w']])
18 del ar
19 # Calculate transport distribution
20 SK.transport_distribution(direction=['xx'], Om_mesh=[0.0,0.2], \
21   with_Sigma=True, beta=40)
22 # Evaluate transport integration
23 SK.conductivity_and_seebeck(beta=40)
24 # Save results to h5 file
25 SK.save(['seebeck','optic_cond'])
```

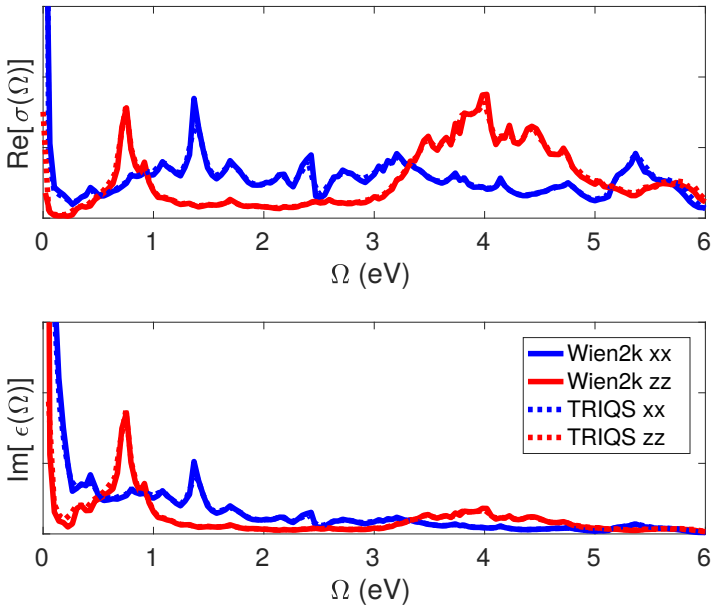

Figure 3.2.: Real part of the optical conductivity $\sigma(\Omega)$ (top graph) and the imaginary part of dielectric function $\epsilon(\Omega)$ (bottom graph) of a non-spin-polarized DFT calculation for $BaMn_2As_2$ in the x (blue) and z (red) directions. The results obtained directly with the Wien2k *joint* program (full lines) are compared to the TRIQS/DFTTools transport code (dotted lines).

In Fig. 3.2 the real part of the optical conductivity and the imaginary part of the dielectric function calculated form a non-spin-polarized DFT calculation for $BaMn_2As_2$ are shown in x direction (blue) and z direction (red).[24,25] The full lines show the result obtained with the Wien2k *joint* program, which calculates the optical conductivity for the inter-band transitions and assumes a Drude model to take the intra-band contributions into account. As Drude broadening $\Gamma = 0.02$ was used, such that the low-Ω part of the dielectric function is in good agreement with the TRIQS/DFTTools transport code. For the TRIQS/DFTTools transport results (dotted lines) we set the self-energy to zero, but use a numerical broadening of $0^+ = 0.005\,\text{eV}$ to calculate $A(\mathbf{k}, \omega)$. In both calculations we use the full velocity matrices calculated with the Wien2k *optics* program and a total number of 150 000 $\mathbf{k}$-points in the full BZ. As expected, the evaluation of the optical conductivity and the dielectric function with the TRIQS/DFTTools transport code is in perfect agreement with the results of the Wien2k *joint* program.

[24] We refer the reader to Ch. 5 for details on $BaMn_2As_2$.

[25] The optical conductivity $\sigma(\Omega)$ and the dielectric function $\epsilon(\Omega)$ are related via $\Re[\epsilon(\Omega)] = \Im[\sigma(\Omega)]/(4\pi\Omega)$.

4. A prototypical example - $SrVO_3$

Preamble

On the example of the "benchmark" material $SrVO_3$, we discuss various aspects of the DFT+DMFT framework in this chapter. Secs. 4.2.1, 4.2.2, and 4.2.3 are mainly an excerpt of the material covered in the TRIQS/DFTTools publication [112]. The author's contribution comprises the implementation, documentation, and maintenance of the TRIQS/DFTTools transport code. Specifically, the author of this thesis was involved in writing the manuscript and provided the results and discussions presented in Sec. 6 of Ref. [112].

The last part of this chapter (Sec. 4.2.4) is devoted to the atomic multiplet structure of $SrVO_3$. Therein, we adapt figures and texts from the publication on the FTPS solver [89]. With the exception of the solver development itself, which was *entirely* carried out by D. Bauernfeind, the author of this thesis contributed to all other parts. This includes the adaptation of the TRIQS/DFTTools package for DMFT calculations on the real-frequency axis, the embedding of the FTPS solver into the DFT+DMFT framework, the interpretation of the multiplet structure, the CTQMC calculations for $SrVO_3$, and the writing of the manuscript. R. Triebl contributed to the analysis of the results and the analytic continuation study.

4.1. Introduction

The transition metal oxide $SrVO_3$ has a cubic perovskite crystal structure ($Pm\overline{3}m$) with an open V-3d shell and a nominal electronic configuration of $3d^1$ (Fig. 4.1) [152]. The V atoms are encaged by O atoms and under the influence of the electric fields

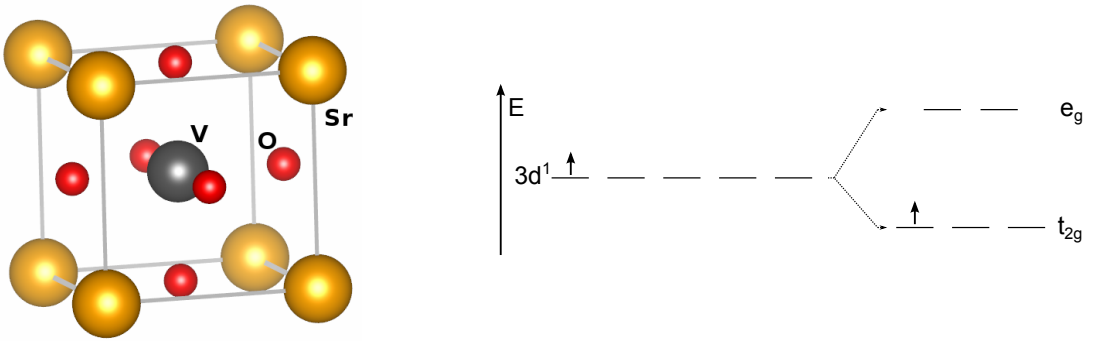

Figure 4.1.: Left: $SrVO_3$ crystal structure. Golden spheres: strontium; grey sphere: vanadium; red spheres: oxygen. The size of the atoms is not to scale. The crystal structure was drawn with VESTA [154]. Right: Lifted degeneracy of the $3d$ orbitals into two e_g and three t_{2g} orbitals due to the crystal-field splitting introduced by the encaging oxygen atoms. This drawing is taken from Ref. [47].

of this octahedral environment the degeneracy of the V-$3d$ states is lifted. Orbitals pointing towards the O ions (z^2 and $x^2 - y^2$) have a higher energy than those pointing between them (xy, xz and yz). This crystal-field, acting on the V-$3d$ states, splits them into the two-fold degenerate e_g states and the lower lying three-fold degenerated t_{2g} states (right plot of Fig. 4.1) [153].

The reason for the popularity of $SrVO_3$ as a prototypical material in the DMFT community is based on the fact that $SrVO_3$, on one hand, requires to solve a multi-orbital Hubbard model to describe the correlated subspace appropriately, but has, on the other hand, very beneficial properties like its paramagnetic ground state and degenerate V-t_{2g} orbitals at the Fermi energy. Next to DFT+DMFT calculations [155], $SrVO_3$ was recently investigated within the GW+DMFT framework [156, 157] and was also used with regard to the development of impurity solvers [89]. Concerning transport calculations, $SrVO_3$ served as benchmark material for the *woptic* package [131] and also in the study of the Peierls approximation for the optical conductivity [158]. As we will see in the next sections, the "standard" DFT+DMFT picture is that $SrVO_3$ is a correlated metal with a spectral function exhibiting a lower Hubbard band, a quasiparticle peak and a upper Hubbard band, which is a structure we have already observed for the half-filled Bethe lattice in Sec. 2.6. Both, in theory and experiment the quasiparticle weight is between $Z = 0.5$ and 0.6 [155, 159]. How-

ever, it should also be noted that very recent GW+EDMFT calculations indicate a much lower screened interaction of the V-t_{2g} orbitals than the one usually assumed in DFT+DMFT calculations [160, 161]. This would point towards a picture where the spectral weight initially attributed to the upper Hubbard band is actually generated by a plasmonic excitation.

We do not elaborate on this fact further, but rather use $SrVO_3$ as a benchmark material to (i) show the necessary procedures for a DFT+DMFT calculations and (ii) show the benefits of the recently developed FTPS solver [89] over the CTHYB+MEM approach. For the second point, we focus on the analysis of the observed multiplet structure in the upper Hubbard band, which has, so far, not been resolved by other impurity solvers.

4.2. Results

4.2.1. DFT and projective Wannier functions

The first step of every DFT+DMFT calculation is to carry out the DFT part and analyze the resulting DOS to identify the correlated shells, which define the correlated subspace for the DMFT calculation. Here we use Wien2k [117, 118] for the DFT calculation. We set the unit cell length of the cubic crystal to $a = 3.8425\,\text{Å}$ [162] and converge the DFT total energy with a set of 969 $\mathbf{k}$-points in the irreducible BZ.

The total and atom resolved DFT DOS of $SrVO_3$ is shown in the top and middle graph of Fig. 4.2. The projection on the Sr shells does only show noticeable weight above about 5.0 eV. More important, we do not observe a considerable hybridization of the V orbitals with Sr, and therefore those are irrelevant for our further discussion. As elaborated in Sec. 4.1, the Fermi level cuts through the V-t_{2g} manifold, which has a nominal filling of one electron. Below the V-t_{2g} bands, the O-2p orbitals show their main contribution from $-7.0\,\text{eV}$ to $-2.0\,\text{eV}$. Additionally, there is a weak hybridization of the V-t_{2g} orbitals and the O-2p orbitals. The V-e_g states form a broad band from about 1.3 eV to 5.5 eV and are well separated in energy from the V-t_{2g} bands. Therefore, it is justified to neglect both, the nominally empty V-e_g orbitals and the filled O-2p orbitals, and consider only the three partially filled V-t_{2g} bands for the construction of the low-energy multi-orbital Hubbard model.

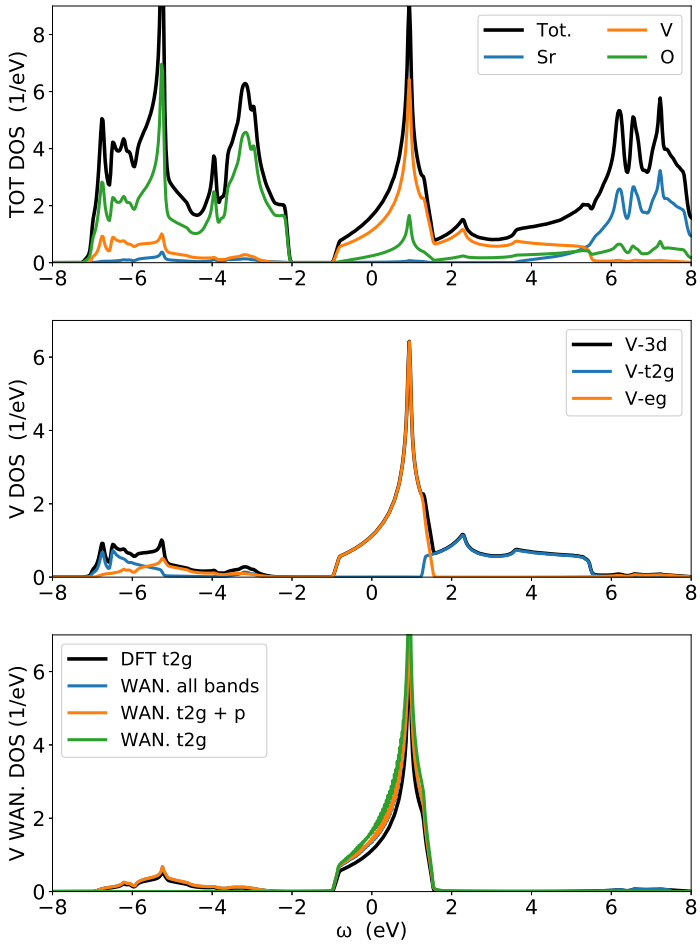

Figure 4.2.: Top: Total DFT DOS of $SrVO_3$ (black) and atom projected DOS of Sr (blue), V (orange) and O (green). Middle: Partial DOS of V-3d (black) and its t_{2g} (blue) and e_g (orange) contributions. Bottom: V-t_{2g} DFT DOS (black) compared to t_{2g}-like Wannier functions generated for three different choices of projective energy windows $\mathcal{W}$. Green line: only V-t_{2g} bands, $\mathcal{W} = [-1.5, 1.9]\,\text{eV}$. Orange line: V-$t_{2g}$ and O-2p bands, $\mathcal{W} = [-8.0, 1.9]\,\text{eV}$. Blue line: even larger window, $\mathcal{W} = [-8.0, 7.5]\,\text{eV}$. Note the small additional weight around 7 eV in the latter case. A numerical broadening of 0.01 eV was used to calculate the Wannier DOS. The Fermi energy is set to $\omega = 0\,\text{eV}$ in all graphs.

The next step is the construction of the projection onto the orbitals of the correlated subspace. To this end, the TRIQS/DFTTools package provides methods to construct projective Wannier functions within a given energy window $\mathcal{W}$ (see Refs. [112, 116, 119] and Sec. 2.7). The dependence of the DOS in the Wannier basis on the choice of $\mathcal{W}$ is presented in the bottom graph of Fig. 4.2. The projection onto the V-t_{2g} bands in an energy window of $\mathcal{W} = [-1.5, 1.9]\,\mathrm{eV}$ is shown in green. A so called *d-dp* model, with an energy window of $\mathcal{W} = [-8.0, 1.9]\,\mathrm{eV}$ that comprises V-t_{2g} states and their hybridized weight on the O-2p bands, is shown in orange. The blue line is the DOS for a projection using the V-t_{2g} weights on all DFT bands up to 7.5 eV. The difference in the latter two is primarily in the transfer of some minor spectral weight to large energies around 7 eV. The density of the projected DOS is equal to the nominal filling of exactly one electron for the smallest energy window, but is 1.7 electrons for the larger windows due to the inclusion of the V-t_{2g} hybridizations on the O-2p bands.

For all three Wannier constructions discussed above 34 220 **k**-points in the irreducible BZ were used. This rather high number of **k**-points is necessary for solvers working directly on the real-frequency axis, e.g. the FTPS solver (Secs. 2.4.4 and 4.2.4), where a sufficiently dense **k**-mesh is crucial to avoid oscillations in the Wannier DOS. These would also be present in the Weiss field $\mathcal{G}_0(\omega)$, which is essentially the input of the impurity solver. Further, for the calculation of the lattice Green's function $G(\mathbf{k}, \omega)$ within each DMFT cycle (Eq. 2.57 with $z = \omega + i0^+$) a dense **k**-grid is beneficial to keep the numerical broadening ($i0^+$) small. This is not necessary when the DMFT cycle is performed on the Matsubara axis, and thus far less **k**-points are required. For the DMFT results shown in the next section only 969 **k**-points in the irreducible BZ have been used.

4.2.2. Correlated spectral function

In this section we show the result of a one-shot DFT+DMFT calculation for $SrVO_3$. Projective Wannier functions constructed within the largest energy window ($\mathcal{W} = [-8.0, 7.5]\,\mathrm{eV}$) are used. We describe the V-t_{2g} correlated subspace with the Kanamori Hamiltonian (Eq. 2.17) and set the interaction parameters to $U_K = 6.0\,\mathrm{eV}$ and $J_K = 0.65\,\mathrm{eV}$. The impurity problem is solved with the TRIQS/CTHYB solver [88] at an inverse temperature of $\beta = 40\,\mathrm{eV}^{-1}$ with a total number of $3.2 \cdot 10^7$ measurements.

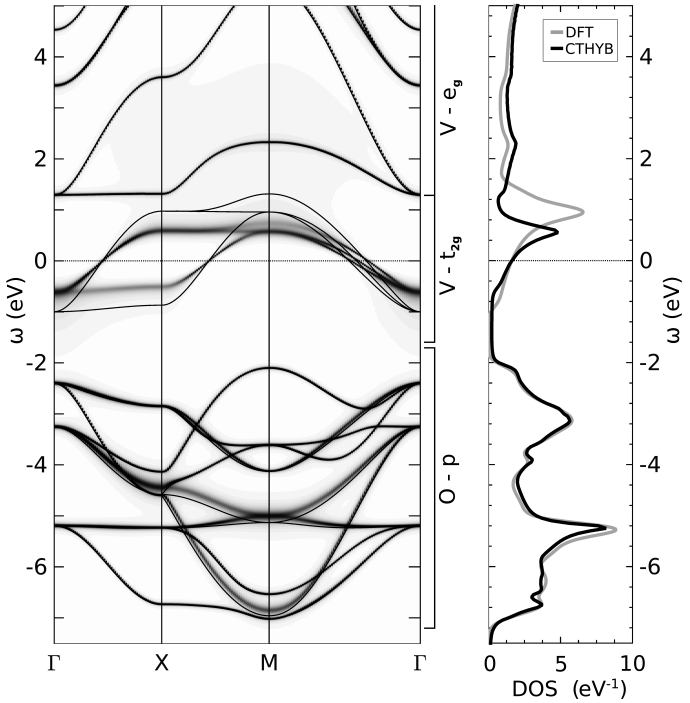

Figure 4.3.: Left: Correlated band structure $A(\mathbf{k}, \omega)$ of $SrVO_3$ (grey-shaded plot) compared to the DFT band structure (black lines) on the Γ-X-M-Γ path. Right: Correlated local spectral function $A(\omega)$ (black line) and DFT DOS (grey line). The Fermi level is set to $\omega = 0\,\text{eV}$. This figure is taken from Ref. [112].

The analytic continuation is performed with the stochastic method by Beach [101]. On the lattice level, the chosen energy window includes states with strong O character, and therefore a double-counting correction is necessary, which effectively shifts the correlated subspace with respect to the O-2p states. We employ a variant of the FLL method constructed for Kanamori Hamiltonians [126].

Including the spin degrees of freedom, the interacting impurity problem for the V-t_{2g} Wannier functions is described by 6×6 self-energy and Green's function matrices. Due to the fact that the V-t_{2g} orbitals are degenerate in $SrVO_3$, these matrices are diagonal and independent of orbital and spin index. This allows for a symmetrization of the solver output in each DMFT iteration. Such a symmetrization usually stabilizes the DMFT loop and leads to a faster convergence. For $SrVO_3$ DMFT is already well converged after 10 to 15 iterations.

In Fig. 4.3 (left graph) we show a comparison of the DFT and the DFT+DMFT spectral functions $A(\mathbf{k}, \omega)$ on the Γ-X-M-Γ path through the BZ. The thin black lines are the DFT results. One can clearly identify the mass renormalization of the V-t_{2g} bands, which is a bit smaller than two in our calculation.[26] In the correlated band structure incoherent weight between about 1 eV and 4 eV is present (gray-shaded area), which can be attributed to the upper Hubbard band. The O-2p and the V-e_g states are only marginally altered by the self-energy. However, due to the hybridization of the V-t_{2g} orbitals with the O-2p orbitals, some bands between -7 eV and -2 eV acquire a finite width, noticeable by the gray shades of certain bands in this energy range. In general, bands with a stronger V-t_{2g} character will be more affected by the self-energy in the upfolding procedure.

The total correlated spectral function $A(\omega)$ compared to the total DOS is shown in the right graph of Fig. 4.3. Although the renormalization of the quasiparticle peak is clearly visible, the expected lower and upper Hubbard bands cannot be identified on this level. The reason is that the lower Hubbard band is covered by the O-2p and the upper Hubbard band is covered by the V-e_g states, respectively. Nevertheless, we will see in Sec. 4.2.4 that the characteristic structure of a quasiparticle peak and two Hubbard bands is clearly visible on the level of the local (impurity) spectral function.

4.2.3. Transport calculations

We turn now to the calculation of transport properties using the formalism described in Ch. 3. We apply the same setup as used for the calculation of the $SrVO_3$ band structure, hence we consider all optical transitions between states in the largest energy window ($\mathcal{W} = [-8.0, 7.5]$ eV). The number of $\mathbf{k}$-points in the irreducible BZ is increased to 4495 for the results presented in this section.

In Fig. 4.4 we compare the optical conductivity $\sigma(\Omega)$ calculated with DFT+DMFT and Eq. 3.22 (black solid line) to experimental data [163] (blue dotted line). To show the effect of electronic correlations, we also present results without frequency-dependent self-energy (red dashed line), where we instead set the imaginary part of the self-energy

[26] Although the mass renormalization is apparent in $A(\mathbf{k}, \omega)$, in practice it can be estimated directly from the slope of the imaginary part of the Matsubara self-energy for $i\omega \to 0$ (see Sec. 2.6).

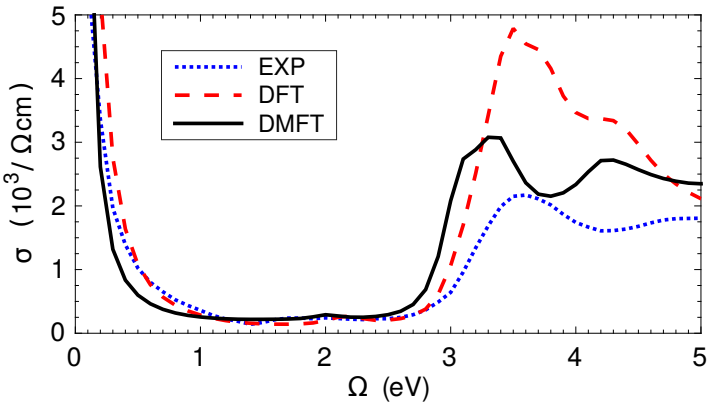

Figure 4.4.: Optical conductivity $\sigma(\Omega)$ of $SrVO_3$ calculated with DFT+DMFT (black solid line) and directly from DFT within the const.-τ_s approximation (red dashed line) compared to experimental data from Ref. [163] (blue dotted line). This figure is taken from Ref. [112].

to a constant value of $-0.05\,\text{eV}$. This corresponds to evaluating the optical conductivity directly from DFT within the const.-τ_s approximation (see Sec. 3.3).

As expected for a metal, the optical conductivity exhibits a Drude peak visible for $\Omega < 0.5\,\text{eV}$ in the DFT+const.-τ_s, the DFT+DMFT, and the experimental data. Additionally, all three show a strong enhancement of the optical conductivity in a frequency range from roughly 2.8 eV to 3.5 eV, which originates from transitions from the occupied O-2p orbitals to the unoccupied part of the V-t_{2g} orbitals. Importantly, the renormalization of the t_{2g} states results in a smaller Drude weight and in a reduction of the optical weight above 3 eV. Further, in the DFT+DMFT optical spectra a subtle peak around 2.0 eV, stemming from transitions within the V-3d manifold (cf. Ref. [158]), is present. Overall, the DFT+DMFT optical conductivity shows a better agreement with the experimental data than the DFT+const.-τ_s result. As also observed in Refs. [131, 158], the peak between 3.0 eV and 4.0 eV is found about 0.3 eV lower in DFT+DMFT. This could be caused by O-2p states positioned slightly too high in energy already on the DFT level. We think that the better agreement of the peak position in the DFT+const.-τ_s optical spectra with the experiment is the result of an error cancellation between the missing renormalization and a slightly wrong position of the O-2p bands.

For the static transport quantities we obtain at $T = 290\,\mathrm{K}$ a resistivity ($\sigma(0)^{-1}$) of $47\,\mu\Omega\,\mathrm{cm}$, which compares reasonably well with the experimental value of $70\,\mu\Omega\,\mathrm{cm}$ [164]. The Seebeck coefficient, $-8\,\mu\mathrm{V\,K}^{-1}$ in our calculation, agrees remarkably well with the experimental room temperature value of about $-11\,\mu\mathrm{V\,K}^{-1}$ [165]. We emphasize that sometimes scattering processes not included in plain DFT+DMFT calculations (e.g. phonons, impurities, or non-local fluctuations) can become important. In such cases, the calculated resistivity constitutes a lower bound to the expected experimental value.

4.2.4. Atomic multiplet structure

Finally, we turn to the discussion of new insights on the spectral function of $SrVO_3$ provided by the real-frequency FTPS solver (see Ref. [89] and the brief overview in Sec. 2.4.4). In this section all shown quantities are per orbital and per spin. For the results presented here, we use 34 220 **k**-points in the irreducible BZ and a small numerical broadening of only $0^+ = 0.005\,\mathrm{eV}$. The projective Wannier functions were constructed in the energy window $\mathcal{W} = [-1.5, 1.9]\,\mathrm{eV}$. Like in the previous sections, we use the Kanamori Hamiltonian as defined in Eq. 2.17, but owing to the smaller effective bandwidth in comparison to the *d-dp* calculations, we decrease the Coulomb interaction to $U_K = 4.0\,\mathrm{eV}$ and the Hund's coupling to $J_K = 0.6\,\mathrm{eV}$. These interaction values lead to a quasiparticle renormalization of $Z = 0.6$. The time-evolution is usually the most demanding part of the FTPS calculation, but due to the degeneracy of the V-t_{2g} orbitals, it is only necessary to perform it for one Green's function, e.g. $G_{xy,\uparrow}$. First, we discuss results where we neglect the spin-flip and pair-hopping terms (density-density Hamiltonian), but we show the resulting spectra including those terms at the end of this section.

In the left graph of Fig. 4.5 we compare the converged impurity spectral function $A(\omega)$ of a DFT+DMFT calculation with FTPS as impurity solver to the one obtained with the CTHYB solver ($\beta = 200\,\mathrm{eV}^{-1}$) and analytic continuation to the real-frequency axis using the Ω-MEM [166]. In both methods the well known features of the $SrVO_3$ spectral function [167, 168] are present. These are a hole excitation at around $-2\,\mathrm{eV}$ (lower Hubbard band), the quasiparticle peak at zero energy and a upper Hubbard band with its maximum around 3 eV. Next to the stronger pronounced lower Hubbard in the

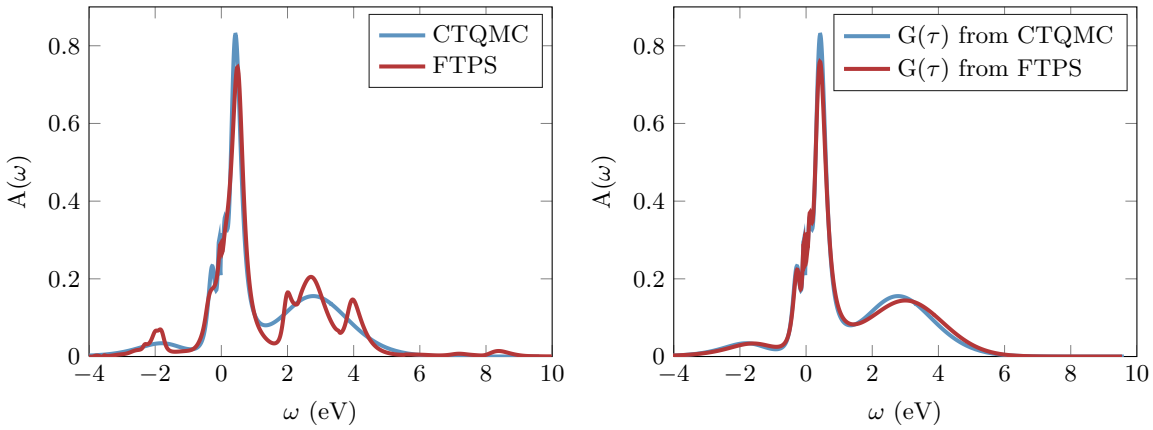

Figure 4.5.: Left: DFT+DMFT impurity spectral functions $A(\omega)$ from CTHYB+MEM (blue line) with $\beta = 200\,\mathrm{eV}^{-1}$, and from FTPS (red line). The FTPS result shows a distinctive three-peak structure in the upper Hubbard band. Right: Spectral functions from analytically continued imaginary-time Green's functions $G(\tau)$ calculated with CTHYB (blue line) and with FTPS (red line). The Fermi level is set to $\omega = 0\,\mathrm{eV}$ and both graphs are taken from Ref. [89].

FTPS spectrum, the most striking feature is the three-peak structure in the upper Hubbard band, which is not present in the CTHYB+MEM spectrum. Also, the use of the stochastic analytic continuation methods by Beach [101] and Mishchenkov [102] did not show a distinct peak structure in the upper Hubbard band.

However, apart from statistical error the CTHYB solver provides an exact solution of the AIM on the imaginary-time axis, and thus the peak structure has to be contained also in the CTHYB result. From the FTPS spectral function we construct an imaginary-time Green's functions $G(\tau)$ for an artificial inverse temperature $\beta = 200\,\mathrm{eV}^{-1}$ with Eq. 2.40. A comparison of the resulting Green's function to the "exact" $G(\tau)$ of the CTHYB solver is shown in Fig. 4.6. The good agreement suggest that the analytic continuation might prohibit the resolution of the peak structure in the upper Hubbard band.

To proof this statement, we use the $G(\tau)$ calculated from the FTPS spectrum and add noise of the order of the CTHYB error. Then, we perform an analytic continuation of this "artificially noisy" FTPS $G(\tau)$ back to the real-frequency axis. As shown in the right graph of Fig. 4.5, the peak structure in the upper Hubbard band vanishes in this

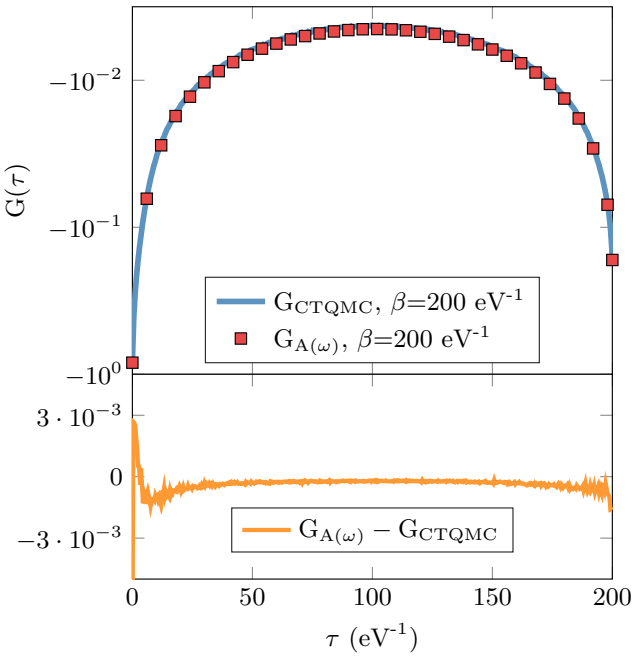

Figure 4.6.: Comparison of the imaginary-time Green's functions $G(\tau)$ from CTHYB (blue line) and an artificial $G(\tau)$ constructed from the FTPS $A(\omega)$ (red squares). The agreement is equally good also for $\beta = 100\,\mathrm{eV}^{-1}$ and $\beta = 400\,\mathrm{eV}^{-1}$ (not shown). This figure is taken from Ref. [89].

process. This test confirms that the analytic continuation is not able to resolve the sharp features present in the upper Hubbard band. Nevertheless, the shape and the position of the quasiparticle peak is well captured also by the analytic continuation (left graph of Fig. 4.5), which underlines that the analytic continuation performs best in the low-energy region of the spectrum.

Next, we discuss the three peaks observed in the upper Hubbard band, which can be understood as the multiplet structure of the underlying atomic problem. For the analysis of this multiplet structure we consider the interaction part of the density-density Kanamori Hamiltonian. The local one-particle part of the Hamiltonian is governed by the on-site energy of the impurity ϵ_0. For the density-density only case the interaction term is already diagonal in the orbital basis, and thus the eigenvalues of the Hamiltonian can be easily read off. For $SrVO_3$ the ground state lies in the $N = 1$ sector.

Table 4.1.: Relevant states of the atomic problem of Hamiltonian 2.17 without spin-flip and pair-hopping terms. This table is an excerpt of Tab. 1 in Ref. [89].

type	states	energy difference to GS
$N = 1$, ground state (GS)	$\|\uparrow,0,0\rangle$ $\|\downarrow,0,0\rangle$ $\|0,\uparrow,0\rangle\cdots$	0
$N = 0$	$\|0,0,0\rangle$	$-\epsilon_0$
$N = 2$, same spin	$\|\uparrow,\uparrow,0\rangle$ $\|\uparrow,0,\uparrow\rangle$ $\|0,\uparrow,\uparrow\rangle\cdots$	$U_K - 3J_K + \epsilon_0$
$N = 2$, different spin	$\|\uparrow,\downarrow,0\rangle$ $\|\uparrow,0,\downarrow\rangle$ $\|\downarrow,\uparrow,0\rangle\cdots$	$U_K - 2J_K + \epsilon_0$
$N = 2$, double occ.	$\|\uparrow\downarrow,0,0\rangle$ $\|0,\uparrow\downarrow,0\rangle$ $\|0,0,\uparrow\downarrow\rangle$	$U_K + \epsilon_0$

Tab. 4.1 shows the relevant atomic states and their corresponding energies. The atomic model has a hole excitation at energy $-\epsilon_0$ and three single-electron excitations with energies $U_K+\epsilon_0$, $U_K-2J_K+\epsilon_0$, and $U_K-3J_K+\epsilon_0$ relative to the ground state (GS). If we measure the energy differences between the three peaks present in the upper Hubbard band in our result (left graph of Fig. 4.5), we find values of 1.27 eV and 0.69 eV, which is close to the atomic energy differences of 1.2 eV and 0.6 eV ($J_K = 0.6\,\text{eV}$). In the calculation the hole excitation is at -2.0 eV.

The analysis of the spectral structure suggests that we can understand the positions of the observed peaks by atomic physics with effective parameters $\bar{\epsilon}_0$, $\bar{U}_K$, and $\bar{J}_K$. We can determine $\bar{U}_K = 5.97\,\text{eV}$ (where $U_K = 4.0\,\text{eV}$) from the energy difference of the peak highest in energy to the hole excitation. The higher value of $\bar{U}_K$ compared to U_K is plausible, if we consider the coupling of the impurity to the bath. Then, electrons have additional degrees of freedom to avoid each other by jumping into unoccupied bath states. This will result in a decrease of the double occupancy $\langle n_\uparrow n_\downarrow \rangle$. To model this situation using atomic physics, it is necessary to assume an increased interaction strength. Finally, J_K is known to be more atomic-like and less affected by the surrounding of the atom than U_K, since the latter is screened significantly stronger [58].

Further evidence that the observed peak structure is indeed a result of atomic physics is provided by the analysis of the influence of J_K on the position of the peaks. The left graph of Fig. 4.7 shows a closeup of the upper Hubbard band for three different values of J_K. Indeed, by increasing J_K the peaks are shifted away from each other, which also increases the total width of the Hubbard band. For all used J_K values the energy distances are approximately J_K and $2J_K$.

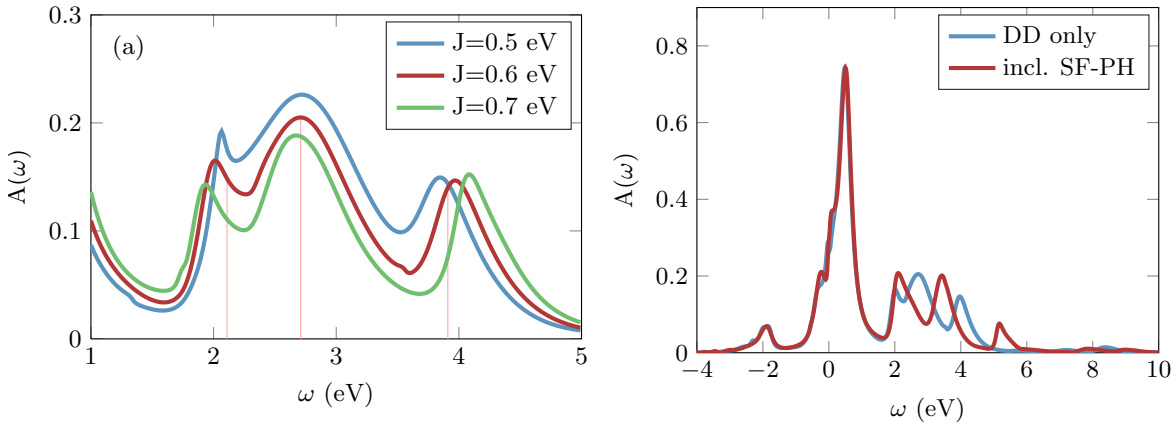

Figure 4.7.: Left: Closeup of the three-peak structure for various values of J_K. Additionally, we show vertical lines for the $J_K = 0.6\,\text{eV}$ spectrum at energies ω_M (position of the middle peak) and at $\omega_M + 2J_K$ and $\omega_M - J_K$. We see that the width of the upper Hubbard band is close to $3J_K$. Right: Spectral functions $A(\omega)$ for density-density (DD) interactions only (blue line), and with spin-flip and pair-hopping terms included (red line). Both spectra show a three-peak structure in the upper Hubbard band and additional features at high energies at around 8 eV. The Fermi level is set to $\omega = 0\,\text{eV}$ and both graphs are taken from Ref. [89].

We also want to point the reader to the small peaks observed at energies around 8.0 eV (Fig. 4.5). These additional structures can again be explained by atomic physics, namely by excitations into states with 3 electrons on the impurity. These excitations originate from small admixtures of $N = 2$ states to the ground state. For the detailed investigation of the $N = 3$ peak structure we refer the reader to Ref. [89].

When we include the spin-flip and pair-hopping terms in the impurity Hamiltonian (see right graph of Fig. 4.7), the positions of the three peaks in the upper Hubbard band are shifted. Again, we can understand the spectrum by an analysis of the underlying atomic physics. First, the spin-flip and pair-hopping terms can only have an effect if there are two or more particles present, and therefore the quasiparticle peak and the hole excitation remain unchanged. However, the atomic $N = 2$ sector, which is responsible for the peak structure in the upper Hubbard band, does change. Diagonalizing the full local Kanamori Hamiltonian gives eigenstates with energy differences of $2J_K = 1.2\,\text{eV}$ and $3J_K = 1.8\,\text{eV}$. This is in perfect agreement with the energy differences in the

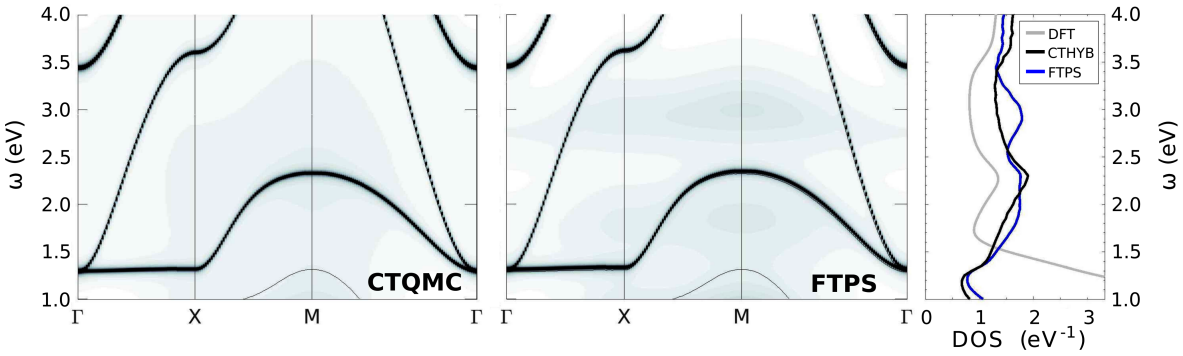

Figure 4.8.: Left: Excerpt of the correlated band structure $A(\mathbf{k}, \omega)$ on the Γ-X-M-Γ path through the BZ as shown in Fig. 4.3. Center: Same detail, but the FTPS solver is used to solve the impurity problem. Right: Total DFT DOS (gray line) compared to the DFT+DMFT spectral function calculated with the CTHYB solver (black) and the FTPS solver (blue). Note the three times smaller scale on the x axis in comparison to the scale in Fig. 4.3. For the sake of a proper analysis all results in this figure are calculated using the largest projective window ($\mathcal{W} = [-8.0, 7.5]\,\text{eV}$) in contrast to all other results of this section. The Fermi level is set to $\omega = 0\,\text{eV}$.

right graph of Fig. 4.7, which are $2\bar{J}_K = 1.32\,\text{eV}$ and $3\bar{J}_K = 1.75\,\text{eV}$. Like for the density-density calculation, we again observe high energy excitations at around 8 eV to states of the atomic $N = 3$ sector.

Up to now, we have only analyzed the impurity spectral function of the V-t_{2g} orbitals. Although the resolution of the atomic multiplet structure demonstrates the capabilities of the FTPS solver, we have seen already in Sec. 4.2.2 that the upper Hubbard band coincides in energy with the unoccupied V-e_g states. To this end, we perform a DFT+DMFT calculation with the FTPS solver using the largest projective energy window ($\mathcal{W} = [-8.0, 7.5]\,\text{eV}$) and the same interaction values as in Sec. 4.2.2. In the energy range of the upper Hubbard band from 1 eV to 4 eV the resulting correlated band structure $A(\mathbf{k}, \omega)$ on the Γ-X-M-Γ path through the BZ is shown in the middle graph of Fig. 4.8. In comparison to the $A(\mathbf{k}, \omega)$ obtained with the CTHYB solver (left graph) a peak structure is indeed visible (gray-shaded weights) and especially pronounced at the M point. The multiplet peak positions are in this case again different, because now the impurity model has not a filling of $N = 1.0$, but rather $N = 1.7$ due to the O-2p hybridization.

In the total spectral function, shown in the right graph of Fig. 4.8, the influence of the multiplet structure is only distinctively apparent around 3 eV. Note that we have used here a three times smaller scale on the x axis in comparison to the scale used in Fig. 4.3. It is questionable if insights on this subtle differences can be gained with ellipsometry measurements or inverse photoemission spectroscopy (PES). However, in multiple measurements of optical conductivities in other transition metal oxides multiplet structures were reported. Explicitly, materials where excitations to the Hubbard bands are clearly visible in the optical conductivity are the related transition-metal perovskites $YTiO_3$ and $YSmO_3$ [169], $LaCuO_3$ and $LaNiO_3$ [170], $CeVO_3$, YVO_3, and $GdVO_3$ [171], or also 5-band systems like $LaSrMnO_4$ [172] and $LaSrFeO_4$ [173]. These materials constitute examples where the strengths of the FTPS solver could be exploited in the future and pushed to new limits in terms of including orbital off-diagonal elements in the Weiss field $\mathcal{G}_0(\omega)$ or performing calculations for 5-band models.

4.3. Conclusion

In this chapter we presented various DFT+DMFT calculations for the prototypical material $SrVO_3$. We have shown how the projective Wannier DOS depends on the choice of the energy window, discussed the resulting correlated spectral function, and analyzed the optical conductivity and the Seebeck coefficient. An emphasis was put on the FTPS solver, which allows to carry out DFT+DMFT entirely on the real-frequency axis. For $SrVO_3$ the solver is able to resolve a multiplet structure in the upper Hubbard band that has not been accessible by CTHYB impurity solvers. It turns out that the necessary analytic continuation prohibits the resolution of fine structures at higher energies. The observed multiplet structure can be well understood from an analysis of the atomic spectrum associated with the local part of the Hamiltonian.

5. Importance of effective dimensionality in manganese pnictides

Preamble

In the following chapter we investigate the two manganese pnictides $BaMn_2As_2$ and LaMnAsO, using fully charge self-consistent DFT+DMFT. To keep this chapter self-contained we mainly adopted the same texts and figures as used for the publication [174]. In addition to Chs. 2 and 3 we dedicate Sec. 5.2 to a brief outline of the methods and parameters we use. In Sec. 5.3 our results on the electronic structure, magnetic, and optical properties are presented and compared to experimental values where available. Additionally, a comparison to (angle-resolved) photoemission spectroscopy (ARPES) measurements, published soon after our work, is provided in Sec. 5.3.5.

The author of this thesis has contributed to all stages of the project discussed in this chapter, which includes an extensive literature search, performing the calculations, the discussion and analysis of the results, and the writing of the manuscript. An improved version of the TRIQS/CTHYB impurity solver was provided by P. Seth and I. Krivenko. E. Assmann and M. Aichhorn contributed to the analysis of the results and the writing of the manuscript. Additionally, we also refer the reader to the Master's thesis of S. Erker [175] who has performed an analysis of the studied compounds on the DFT level and undertook the first steps towards a DFT+DMFT solution in the paramagnetic phase.

5.1. Introduction

The Mott phenomenon (see Sec. 2.6), the occurrence of an insulating state solely due to electronic correlations, is among the most intensively studied effects in correlated solid state physics [17]. This insulating state can occur in situations where simple band theory would not allow it, e.g. for an odd number of electrons per unit cell in the absence of symmetry breaking. It is interesting not only in its own right but also as it is the host for other fascinating phenomena, the best-known example being high temperature superconductivity in cuprate oxides. There, injecting charge carriers into this Mott insulating state by chemical doping creates a non-Fermi-liquid state which becomes superconducting at low temperatures [5].

In recent years another class of high-temperature superconductors, the iron-based pnictide and chalcogenide materials, has been identified [176]. In contrast to the cuprates, they are intrinsically multi-band systems with the whole 3*d* manifold being relevant for the electronic properties [116, 177]. These iron-based materials share common building blocks, the iron-pnictogen or iron-chalcogen layers, and a nominal electronic configuration of six electrons in the five Fe-3*d* bands, which places them in the "Hund's metal" regime [62, 178, 179]. As a result of this band filling, these materials have very low coherence scales and sizable correlations, without, however, being close to a Mott metal-insulator transition.

Since superconductivity arises from quantum fluctuations in the normal state, we must understand the physical properties of the relevant parent compounds before we can hope to understand superconductivity. In this chapter we therefore investigate the two manganese pnictide compounds $BaMn_2As_2$ and LaMnAsO, which are isostructural to the iron-based superconductors $BaFe_2As_2$ and LaFeAsO, but host only five electrons in the five Mn-3*d* bands. These systems can be seen as the pnictide analog of the undoped parent compounds of the cuprate high-temperature superconductors [180, 181]. The half-filled Mn-3*d* shells of these compounds promote Mott physics [21–23]. Efforts to induce metallicity by pressure [28] or doping [29, 30, 182–186] have been to some extent successful. While no superconducting state has been demonstrated conclusively [28], the manganese pnictides still feature fascinating properties such as giant magnetoresistance [31, 187], large Seebeck coefficients [25, 27, 41, 188], and strongly enhanced

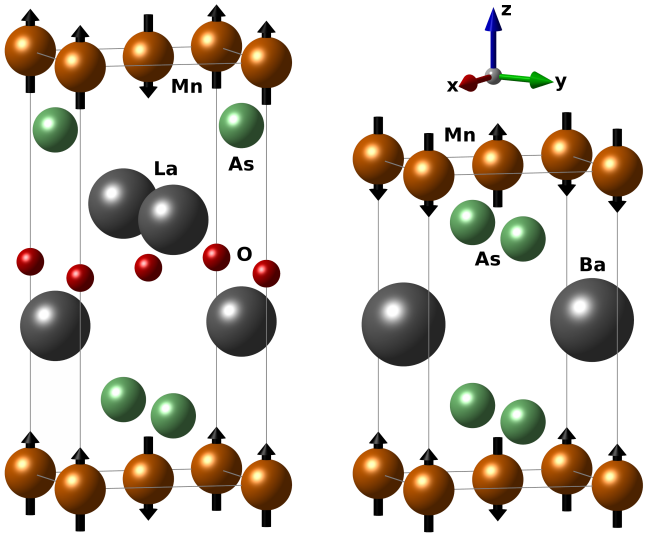

Figure 5.1.: Crystal and magnetic structure of LaMnAsO (left) and $BaMn_2As_2$ (right) drawn with VESTA [154]. The black arrows represent the Mn spins in the antiferromagnetic states of LaMnAsO [31] (C-type: ferromagnetically stacked antiferromagnetic planes) and $BaMn_2As_2$ [32] (G-type: alternating in all directions). We choose a coordinate system where the x and y axes point towards the nearest-neighbor Mn atoms. This figure is taken from Ref. [174].

magnetism with antiferromagnetic (AFM) order persisting up to elevated temperatures [31, 32]. In contrast to the related iron pnictides, both manganese pnictides investigated here are semiconductors, as shown in optical and conductivity measurements [21, 24–29, 188, 189].

When considering an insulating state in a half-filled system the question arises whether this state occurs due to electronic correlations alone (Mott mechanism) or because of symmetry breaking such as magnetism (Slater mechanism). In many correlated materials both mechanisms are at work and sometimes are of similar importance. Furthermore, it has been shown that the proximity to a Mott transition can strongly increase the magnetic ordering temperature [190]. For instance, 1111 manganese pnictides including LaMnAsO ($T_N \approx 350\,K$ [35, 41, 187]) and some 122 manganese pnictides, like $BaMn_2P_2$ ($T_N > 750\,K$ [191]) and $BaMn_2As_2$ ($T_N = 625\,K$ [32]), remain ordered well above room temperature. Néel temperatures of this order naturally call for a closer investigation of the underlying mechanisms.

We will show that LaMnAsO and $BaMn_2As_2$ are both close to a metal-insulator transition. However, there are differences in the effective dimensionality of the two compounds, which will turn out to be decisive for their properties. Specifically, $BaMn_2As_2$ crystallizes in a $ThCr_2Si_2$-type structure and shows G-type AFM (antiferromagnetic in all directions, see Fig. 5.1 right) and a large magnetic moment of $3.9\,\mu_B$/Mn [32]. LaMnAsO, with its ZrCuSiAs structure, features antiferromagnetic Mn planes with a magnetic moment of $3.6\,\mu_B$/Mn [31, 192], but the coupling between planes is ferromagnetic (C-type AFM, shown in Fig. 5.1 left). Although both compounds share Mn-As layers with comparable Mn-Mn distances, the different layer stacking and the larger Mn interlayer spacing turn LaMnAsO into a quasi-two-dimensional compound [33–35], while $BaMn_2As_2$ is much more three dimensional [27, 36]. A dependence of the physical properties on the effective dimensionality has also been observed, e.g. in the iron pnictides [193, 194].

5.2. Methods

DFT+DMFT (Sec. 2.7) is used as a theoretical framework for the electronic structure calculations presented in this chapter. Unless otherwise stated, calculations were carried out with the fully charge self-consistent implementation of the TRIQS/DFTTools package [112, 116, 119]. We use crystal structures measured at 300 K for $BaMn_2As_2$ [32] and 290 K for LaMnAsO [187]. The same crystal structures are used for antiferromagnetic and paramagnetic calculations as no structural phase transition accompanies the magnetic transition in either compound [31, 32]. For the antiferromagnetic calculations we use the experimentally determined magnetic orderings (Fig. 5.1), which are also predicted by total-energy DFT calculations [27, 33, 175]. Note that due to the G-type ordering the magnetic unit cell is doubled in the z direction in $BaMn_2As_2$. For the DFT part of the fully charge self-consistent calculations we use 10 000 $\mathbf{k}$-points in the full Brillouin zone (BZ) and employ the standard Perdew-Burke-Ernzerhof (PBE) [52] generalized gradient approximation (GGA) for the exchange-correlation functional.

From the DFT Bloch states we construct projective Wannier functions for the Mn-3d orbitals in an energy window from $-5.00\,\mathrm{eV}$ to $3.40\,\mathrm{eV}$ for $BaMn_2As_2$. Likewise, we choose an energy window from $-5.50\,\mathrm{eV}$ to $3.25\,\mathrm{eV}$ for LaMnAsO. Using such a large energy window for the projections results in a much better localization of the Mn-3d Wannier functions [112, 116, 195], which plays to the strengths of the DMFT approximation.

In DMFT we work with a full rotationally invariant Slater Hamiltonian (see Sec. 2.2) for the five Mn-3d orbitals with a Coulomb interaction $U = F^0$ of $5.0\,\mathrm{eV}$ and a Hund's coupling $J = (F^2 + F^4)/14$ of $0.9\,\mathrm{eV}$ ($F^4/F^2 = 0.625$). We estimate our interaction parameters from the values used in iron pnictide calculations [119, 177, 196], increasing them slightly to account for the stronger correlations expected in Mn compounds. It is established that the physics of the nominally half-filled Mn-3d shells is strongly governed by J [62, 179]. We find that our J is consistent with values used in other recent works on manganese pnictides [21, 22, 197]. Due to the localized nature of the compounds and the substantial electron-electron correlations, we choose the fully localized limit (FLL) as double-counting correction [125]. In general the choice of the double counting is less crucial in fully charge self-consistent calculations [119].

The TRIQS/CTHYB solver [88] is used to obtain the solution of the impurity model on the Matsubara axis at an inverse temperature $\beta = 40\,\mathrm{eV}^{-1}$, corresponding to room temperature. We use the stochastic method by Beach [101] for the analytic continuation of the self-energy to the real-frequency axis. In the antiferromagnetic case the DFT part is performed without spin polarization; thus the magnetic splitting of the Mn-3d spins is purely introduced by DMFT. To describe the desired antiferromagnetic state, the same self-energy is taken for both Mn atoms in the unit cell, but with swapped spins.

We calculate the optical properties within the Kubo formalism, neglecting vertex corrections, as implemented in the TRIQS/DFTTools package [112] and discussed in Ch. 3. For the optical calculations we increase the number of $\mathbf{k}$-points to 150 000 for $BaMn_2As_2$ and 100 000 for LaMnAsO in the full BZ. To analyze the influence of structural differences, we construct maximally localized Wannier functions (Sec. 2.7) and real-space Hamiltonians with wien2wannier [198] and Wannier90 [151].

5.3. Results

5.3.1. Electronic structure

In this section we present our DFT+DMFT results. While we focus on the antiferromagnetic (AFM) phase, we also consider the paramagnetic (PM) solution to gain insight into the origin of the insulating state (Mott or Slater mechanism).

We start our discussion with the PM spectral functions in Fig. 5.2 (top). In DFT, the total non-spin-polarized DOS (light gray lines) in both compounds are clearly metallic, in contrast to DFT+DMFT, where the weight at the Fermi level is drastically reduced, nearly opening a gap. The structure of the correlated Mn-3d spectral function (shaded areas in Fig. 5.2) is very similar in both compounds and consists of a heavily smeared-out contribution below the Fermi energy, which shows strong hybridization with the As-4p bands along its full width of about 5.0 eV, and a sharp peak ranging from 0.0 eV to about 2.0 eV. On the other hand, the total spectral functions (thick lines in Fig. 5.2) differ below -2.0 eV due to oxygen states present in LaMnAsO but not in $BaMn_2As_2$.

The strong electron-electron correlations in the half-filled Mn-3d shells place both compounds near the metal-insulator transition. This is also seen in the **k**-resolved paramagnetic spectral function in Fig. 5.3. At the Fermi energy, no remnants of DFT bands are observable, indicating that the spectral weight is solely introduced by the imaginary part of the self-energy. This picture is supported by the quasiparticle weights, which are below 0.15 for the x^2-y^2 and the z^2 orbitals.[27] For the other orbitals the estimation of the quasiparticle weights is not meaningful as they show a too strong deviation from the linear Fermi-liquid behavior of $\Im\left[\Sigma(i\omega_n \to 0)\right]$. In the orbital-resolved PM spectral functions of the Mn-3d shell (Fig. 5.4 top row), we observe orbital-selective behavior: While the x^2-y^2 orbital is still unequivocally metallic, electronic correlations drive the z^2 and xz/yz orbitals close to the insulating phase. The xy orbital is even more correlated.

[27] We estimate the quasiparticle weights with a polynomial fit of the self-energies on the Matsubara axis. It should be noted that these are quasiparticle weights in the Wannier basis, and cannot be directly understood as the renormalization of the spectral function in the Bloch basis, where bands are influenced proportionally to their Mn character.

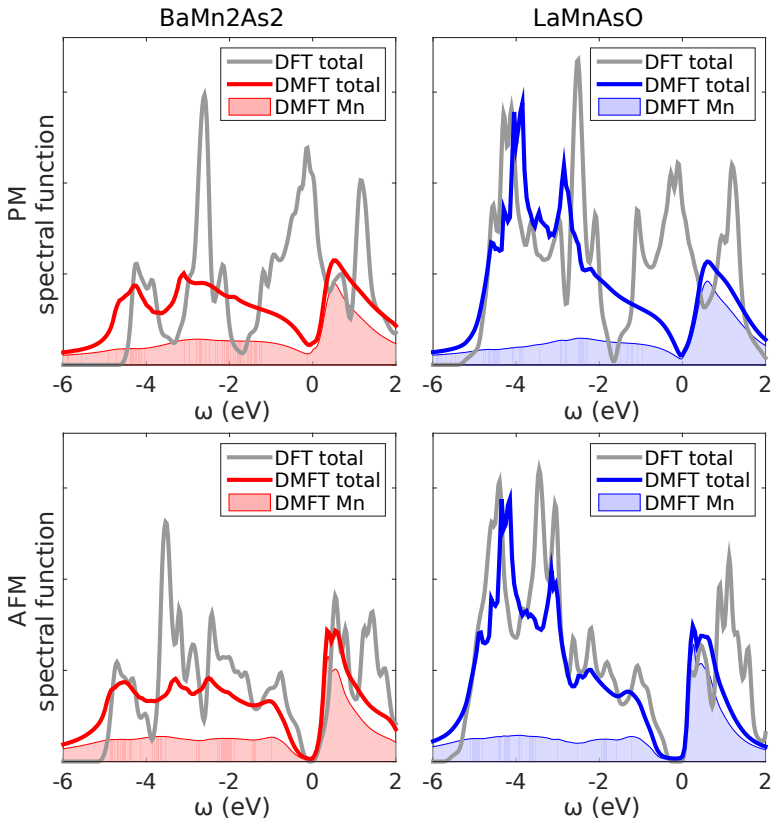

Figure 5.2.: DFT+DMFT paramagnetic (top row) and antiferromagnetic (bottom row) spectral functions of $BaMn_2As_2$ (red) and LaMnAsO (blue) compared to DFT (gray). The shaded areas correspond to the Mn-3d projected spectral functions. The Fermi level is set to $\omega = 0\,\mathrm{eV}$. This figure is taken from Ref. [174].

To substantiate our claim that the investigated compounds are close to a Mott transition we perform additional calculations for LaMnAsO. At room temperature and an interaction strength of $U = 6.0\,\mathrm{eV}$ and $J = 1.0\,\mathrm{eV}$ it remains metallic. However, both lower temperature ($\beta = 100\,\mathrm{eV}^{-1}$) and stronger interactions ($U = 7.0\,\mathrm{eV}$ and $J = 1.1\,\mathrm{eV}$) are independently sufficient to drive the material into the insulating phase. Hence, we conclude that our compounds are indeed close to an insulating phase. Additionally, it was shown that LaMnAsO is Mott-insulating for $U = 2.2\,\mathrm{eV}$ and $J = 0.5\,\mathrm{eV}$ in a d-only model ($\mathcal{W} = [-1.6, 2.2]\,\mathrm{eV}$) [175].[28]

[28] In this calculation the spin-flip and pair-hopping terms of the Hamiltonian were neglected. The d-only model does not take the ligand As/O-p states into account, and thus charge transfer and hybridization effects are not captured.

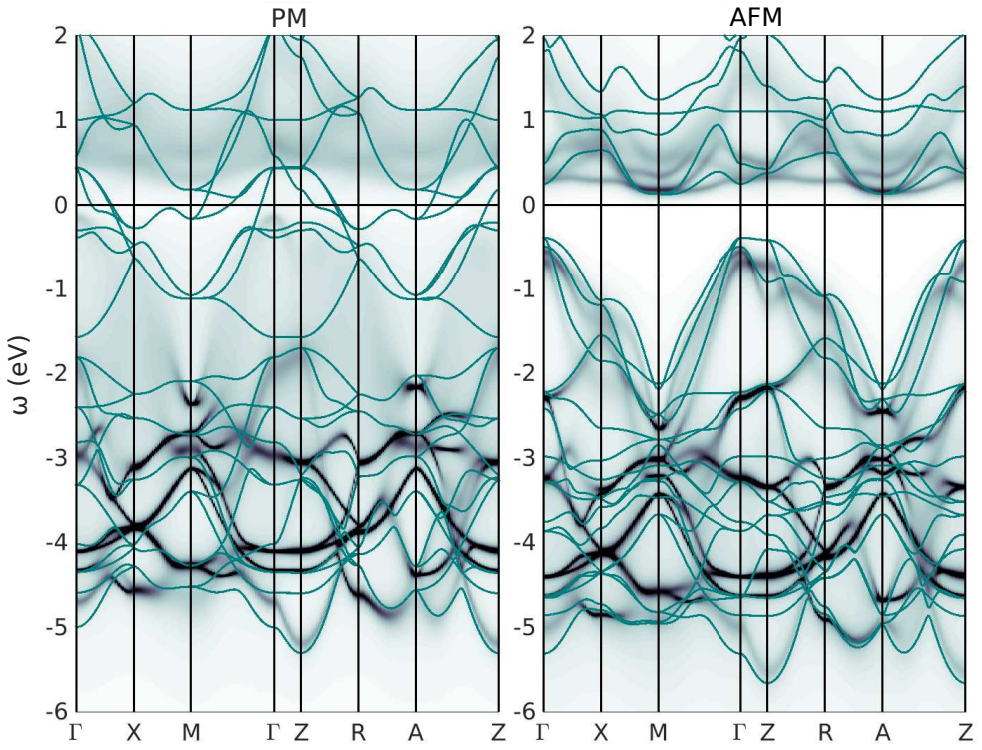

Figure 5.3.: Spectral function $A(\mathbf{k}, \omega)$ for the paramagnetic (left) and antiferromagnetic (right) state of LaMnAsO. The thin solid lines show the DFT bands, while the shading shows the DFT+DMFT spectral weight. For the $\mathbf{k}$-path connecting the high symmetry points of the BZ zone see Fig. A.3. The Fermi level is set to $\omega = 0\,\text{eV}$. This figure is taken from Ref. [174].

It has been pointed out before that in comparison to $BaFe_2As_2$ electronic correlations have a stronger effect in $BaMn_2As_2$, placing the latter significantly closer to the Mott localization picture [23, 199]. Our paramagnetic DFT+DMFT results confirm this observation and extend it to LaMnAsO, which is also more localized than its itinerant Fe relative [116].

Conversely, the AFM spectral functions do feature a gap (Fig. 5.2 bottom). DFT predicts small gaps of 0.1 eV for $BaMn_2As_2$ and 0.5 eV for LaMnAsO (see also App. A), consistent with earlier theoretical results [24, 27, 29, 33, 175]. In DFT+DMFT, the gap remains similar in $BaMn_2As_2$ but is somewhat enlarged in LaMnAsO, to about 0.6 eV.

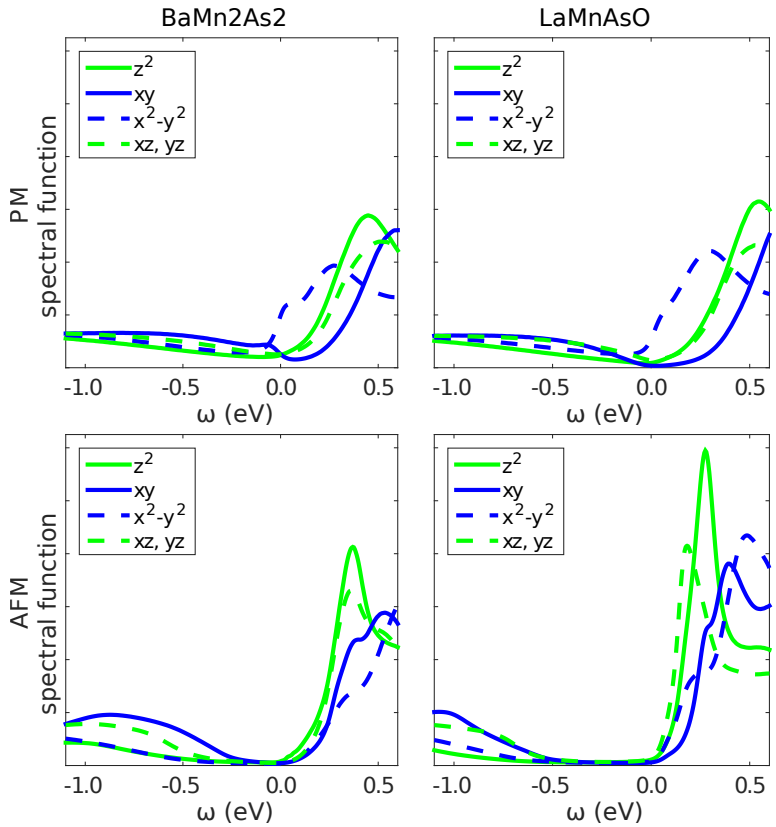

Figure 5.4.: DFT+DMFT orbital-resolved paramagnetic (top row) and antiferromagnetic (bottom row) spectral functions of the correlated manganese atom for $BaMn_2As_2$ (left) and LaMnAsO (right). The Fermi level is set to $\omega = 0.0\,\text{eV}$. This figure is taken from Ref. [174].

In the case of $BaMn_2As_2$, the strong incoherence, the finite temperature, and the influence of the analytic continuation prohibit the statement of an exact value for the band gap. Nevertheless, the gap is clearly very narrow in $BaMn_2As_2$ and of the same order as the DFT result. Although the increase in the band gaps, due to the DFT+DMFT treatment, is smaller than 0.1 eV, electronic correlations lead to important differences in the spectral functions relative to DFT: First, a strong renormalization of the bandwidth of the unoccupied Mn states, and second, a substantial smearing of the occupied Mn spectral weight (see Figs. 5.2 and 5.3). We note that a one-shot DFT+DMFT calculation for LaMnAsO in the AFM phase, where DMFT is converged without updating the DFT charge density, leads to a stronger static spin splitting and in turn to a gap enlarged by about 0.4 eV.

Experiments indicate that $BaMn_2As_2$ has, at least at low temperatures, an indirect band gap of about 0.03 eV [26, 28, 188, 189]. To our knowledge, the only experimental results for the LaMnAsO gap are 1.1 eV from resistivity measurements of a polycrystalline sample at high temperatures [24] and 1.4 eV for LaMnAsO thin films, deduced from optical absorption spectra [25]. In both materials the fundamental gap is indirect, and the smallest direct gap occurs at the Γ point. For $BaMn_2As_2$, this direct gap is about 0.7 eV, close to the recently published value of 0.8 eV [21]. For LaMnAsO, we find a direct gap of about 0.8 eV (see also Fig. 5.3). Unsurprisingly, the AFM **k**-resolved spectral function and the indirect/direct gaps of LaMnAsO agree well with DFT+DMFT calculations for the closely related manganese pnictide LaMnPO [197].

Since both compounds share the structure of the Mn-As layers (Fig. 5.1), it is natural to ask why the band gap of $BaMn_2As_2$ is narrower. The orbital-resolved AFM DFT+DMFT spectral functions projected on the Mn-3d states (Fig. 5.4 bottom) reveal that the gap is between the z^2 orbital on the unoccupied side and the xy orbital on the occupied side in $BaMn_2As_2$. On the other hand, in LaMnAsO the xy gap is considerably wider. Therefore, within the assumptions of our calculation, we can attribute the narrower band gap of $BaMn_2As_2$ to the different spectral contributions of the xy and the z^2 orbitals. Interestingly, the structural difference between the investigated compounds mainly impacts those two orbitals, as we will see in the next section.

5.3.2. Maximally localized Wannier functions

To understand the influence of the structural differences on the Mn-3d orbitals, and on the resulting physical properties, we construct an effective real-space Hamiltonian for both compounds. For the present section, we set aside the projective Wannier functions we use in DFT+DMFT and construct ten maximally localized Wannier functions from the non-spin-polarized Mn-3d bands. This model has the advantage that it directly provides the effective hopping between Mn atoms, including all hopping paths over intermediate atoms (Ba, La, As, O). Thus, it allows us to compare the two compounds on the same footing. The maximally localized Wannier functions for the Mn-3d orbitals are shown in Fig. 5.6.

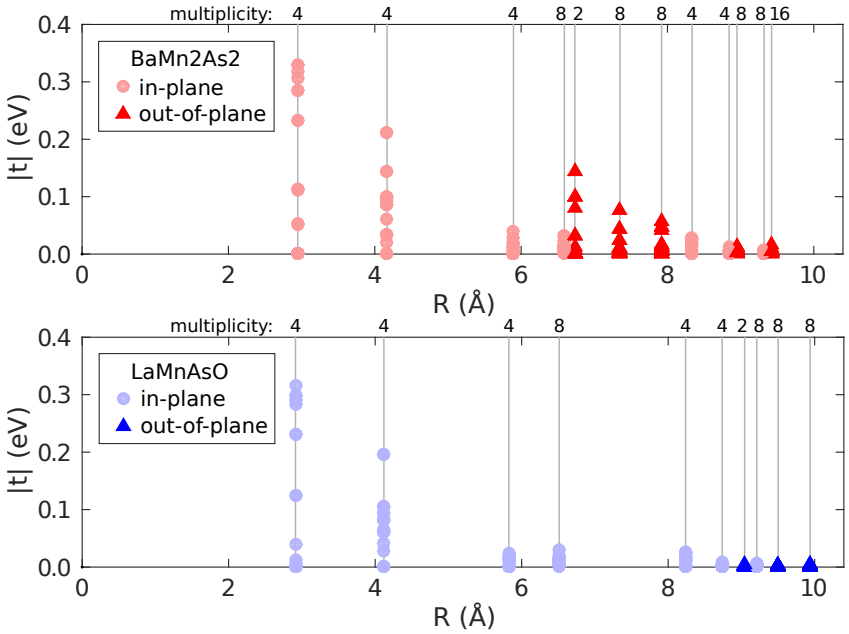

Figure 5.5.: Real-space Hamiltonian matrix elements $|t|$ for $BaMn_2As_2$ (red) and LaMnAsO (blue) from a Wannier90 construction of the Mn-3d orbitals. Shown are all hoppings between Mn atoms separated by the distance R. The given multiplicities correspond to the number of neighbors at that distance. This figure is taken from Ref. [174].

The matrix elements of the resulting effective real-space Hamiltonian as a function of distance are plotted in Fig. 5.5. For each pair of Mn atoms all 25 matrix elements between their five Mn-3d orbitals are shown. Considering the in-plane hopping first (circles), both materials are described by a very similar Hamiltonian, which is expected due to the shared structure of the Mn-As layers and the comparable Mn-Mn distance within those layers. Turning to the interlayer hoppings (triangles), a completely different picture emerges. The Mn atoms in $BaMn_2As_2$ couple substantially to their respective neighbors on adjacent planes, in contrast to LaMnAsO, where the interlayer coupling is on average more than 25 times lower and not visible on the shown scale. From this it follows that LaMnAsO is built up by quasi-two-dimensional Mn-As layers coupled only very weakly to each other, whereas $BaMn_2As_2$ shows much stronger interlayer coupling.

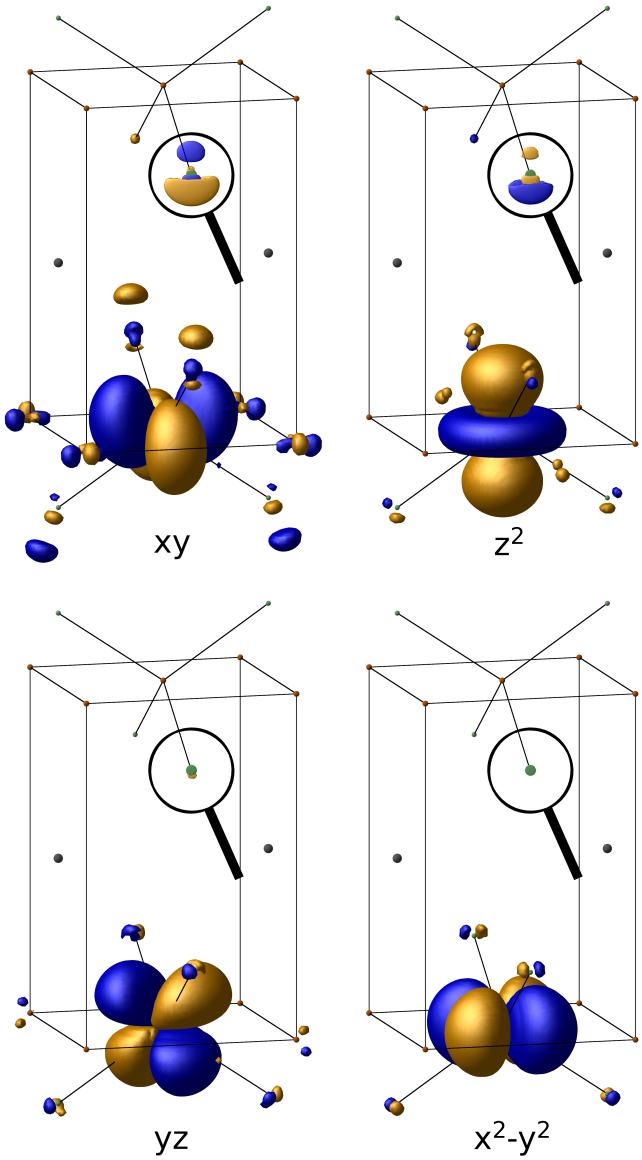

Figure 5.6.: Real-space representation of the maximally localized Wannier orbitals for the Mn-3d shell of $BaMn_2As_2$ constructed with wien2wannier [198] and Wannier90 [151] and visualized in VESTA [154]. The xz orbital, which is not shown here, is related to the yz orbital by crystal symmetry. The thin lines connect the central Mn atoms to the four nearest As atoms. The xy and z^2 orbitals have significant weight also on the As atoms of the neighboring Mn-As layers. To emphasize this contribution, in the magnifier symbols we show it enlarged both by applying a zoom and selecting a smaller isovalue (by a factor of ten). By contrast, in LaMnAsO, no weight would be seen on the adjacent Mn-As layers at these isovalues. This figure is taken from Ref. [174].

It bears mentioning that in $BaMn_2As_2$ the interlayer hoppings follow a different decay than the in-plane hoppings with distance, as visible in the much stronger coupling for similar atomic distances. The responsible hoppings for the interlayer coupling can be nearly exclusively attributed to the xy and z^2 orbitals, as the coupling of the xz, yz orbitals is already below 0.05 eV. The $x^2 - y^2$ orbitals practically do not contribute to the interlayer coupling. The largest hopping strength is found between the xy orbitals, followed by xy to z^2 and z^2 to z^2.

The difference in the interlayer coupling of the Mn-As layers can be traced back to multiple factors. First, the distance between the Mn-As layers is much shorter in $BaMn_2As_2$ (6.73 Å versus 9.04 Å), where they are separated only by the rather narrow Ba layer in contrast to the thicker La-O layer in LaMnAsO (see Fig. 5.1). The fact that the in-plane coupling on distances comparable to the interlayer distance is substantially smaller than the out-of-plane coupling indicates that the spatial distance between the layers is not enough to fully explain the enhanced out-of-plane coupling. The second important difference is the stacking inversion of the Mn-As layers in $BaMn_2As_2$. In LaMnAsO the As atoms do not sit directly above each other as they do in $BaMn_2As_2$, where the small As-As distance leads to a simple hopping path via the As atoms. In the maximally localized Wannier functions, this can be seen in the electronic weight of the xy and z^2 orbitals on the As atoms in the adjacent layer (Fig. 5.6 magnifier symbol).

5.3.3. Néel temperature

The highest Néel temperature T_N in a class of compounds is usually found close to the Mott transition. This was first shown for the single-band Hubbard model on the Bethe lattice [9] and the same argument was recently found to be valid for the $4d$ perovskite $SrTcO_3$ [190] with its exceptionally high transition temperature of 1000 K. When starting from an itinerant picture, for a model with bandwidth W, where the interactions of order U are treated on a mean-field level, the transition temperature scales as $T_N \sim \exp(-W/U)$. On the fully localized side, the adequate picture is the Heisenberg model, where the scaling is $T_N \sim W^2/U$. Between these two extreme cases

we can expect a crossover around $U \approx W$, which coincides with the crossover from an itinerant to a localized system. These qualitative considerations identify the Mott transition as a hotspot for magnetism, and hence materials in this critical region are prone to higher transition temperatures.

From the paramagnetic DFT+DMFT spectral function and the quasiparticle weights, we have seen that $BaMn_2As_2$ and LaMnAsO are close to a Mott transition, and their experimental Néel temperatures are indeed high, with reports of 317 K to 360 K in LaMnAsO [31, 35] and even 625 K in $BaMn_2As_2$ [32]. In Fig. 5.7 we present our DFT+DMFT results for the ordered moment as a function of temperature. For $BaMn_2As_2$ we find an ordering temperature of around 1350 K. The overestimation of the transition temperature by a factor of more than two is not unusual and can be expected due to the mean-field character of DMFT [120, 190]. Under the assumption of a $S = 2$ Heisenberg model the reduction of the mean-field Néel temperature for $BaMn_2As_2$ was estimated to a factor of 2.75 [36]. Considering these aspects, the prediction of the Néel temperature in our calculation is in reasonable agreement with the experimental value. Also, the ordered moment at low temperatures agrees well with the experimental result of 3.9 μ_B/Mn [32].

The situation is different for LaMnAsO. There, the experimental ordering temperature is a factor of two smaller than for $BaMn_2As_2$. However, the DFT+DMFT result is smaller only by about 150 K. The reason is that in quasi-two-dimensional systems, as it is the case for LaMnAsO, spatial fluctuations become important. They in turn decrease the ordering temperature significantly. In the same way, DFT+DMFT yields a saturated magnetic moment of 4.0 μ_B/Mn in contrast to the measured 3.6 μ_B/Mn [31, 192]. We note in passing that the one-shot DFT+DMFT calculation for LaMnAsO does result in an even higher magnetic moment of 4.4 μ_B/Mn.

Our observations are very similar to recent studies in technetium oxides. In the cubic case ($SrTcO_3$) the local DMFT approximation works well [190], but for the layered counterpart Sr_2TcO_4 it overestimates the ordering temperature substantially [200].

The claim that the overestimation of the Néel temperature is tied to the mean-field character of DMFT was quantified for the 3D Hubbard model. It was shown that taking diagrammatic extensions of the theory into account leads to a sizable reduction of the Néel temperature (by more than 30%) in comparison to single-site DMFT [201,

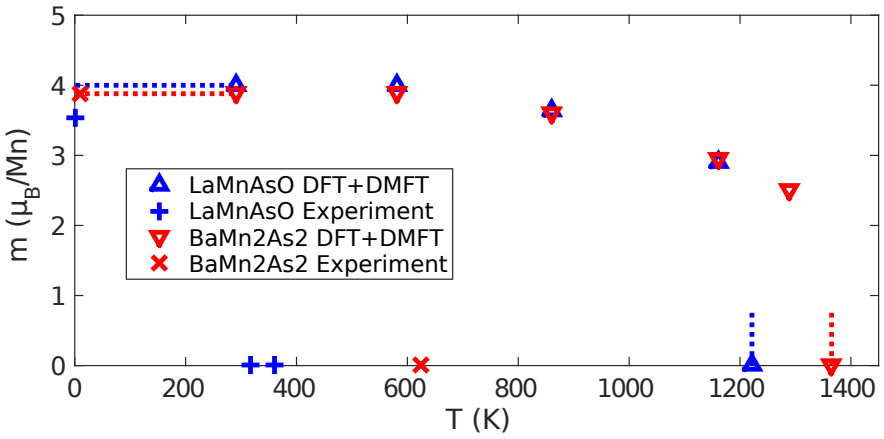

Figure 5.7.: Magnetic moment m versus temperature T from fully charge self-consistent DFT+DMFT for $BaMn_2As_2$ (red triangles) and LaMnAsO (blue triangles). Experimental points are taken from Refs. [31, 35, 192] for LaMnAsO (blue crosses) and from Ref. [32] for $BaMn_2As_2$ (red crosses). The horizontal dotted lines mark the saturated magnetic moments and the vertical dotted lines the approximate Néel temperatures. This figure is taken from Ref. [174].

202]. Furthermore, for the 2D Hubbard model single-site DMFT yields a finite Néel temperature, which is in contradiction to the Mermin-Wagner theorem. Again, this can be cured by the inclusion of spatial correlations [201]. To give an example, it was shown for La_2NiTiO_6, which nominal hosts two electrons in the e_g orbitals, that the mean-field solution of a corresponding $S = 1$ Heisenberg model yields Néel temperatures very similar to the DFT+DMFT result [203].[29]

From another point of view, it is well known that the strength of the interlayer coupling is a crucial factor influencing the magnetic properties of layered materials [204], for instance in the copper oxides [205, 206]. In such compounds, the crossover from a three-dimensional to a layered system leads to a suppression of the Néel temperature as a function of the interlayer exchange coupling $J_\perp$. As we have observed above, the strong decrease of dimensionality in LaMnAsO is confirmed by a reduction of the hopping in the z direction (by a factor larger than 25). This will also be reflected in an

[29] In the same work a careful analysis of the dependence of the Néel temperature on the interaction U was provided. A $1/U$ behavior was observed, which is expected as La_2NiTiO_6 is a Mott-insulator located far in the strong-coupling limit; thus the adequate picture is the one provided by the Heisenberg model.

effective $J_\perp$. Band theoretical estimates and experiments suggest that $J_\perp/J_\parallel < 0.015$ in LaMnAsO [33] and $J_\perp/J_\parallel \approx 0.1$ in $BaMn_2As_2$ [36], with $J_\parallel$ being the in-plane nearest neighbor exchange coupling. This supports the conclusion that the reduced Néel temperature in LaMnAsO can be attributed to the lower dimensionality of the system.

5.3.4. Optical properties

Finally, we turn to the optical conductivity $\sigma^{\alpha\beta}(\Omega)$, Eq. 3.22, which will not only exemplify the dimensional differences of the investigated compounds but also allow a comparison with experimental observations.

Starting with $BaMn_2As_2$ (Fig. 5.8 red lines), we observe only a weak anisotropy in the optical conductivity. Besides the depression around $\Omega \approx 2.5\,\mathrm{eV}$, there is not much of a difference between the in-plane and out-of-plane contributions. This illustrates the more isotropic nature of $BaMn_2As_2$. A small Drude peak present in the in-plane component is in accordance with the observation of a weak metallic behavior at room temperature in Refs. [26, 189]. On the contrary, there is no Drude peak in the out-of-plane component, indicating that $BaMn_2As_2$ is insulating along the z direction, in agreement with the optical experiments of Ref. [26]. The optical conductivity of LaMnAsO (Fig. 5.8 blue lines) in the x direction shows a similar trend, but is reduced by about 1/3 in comparison to $BaMn_2As_2$. Since $\sigma^{zz}(\Omega)$ is strongly suppressed in LaMnAsO, the total optical conductivity becomes largely dominated by the in-plane contribution. The similar in-plane conductivity of both compounds originates from the common Mn-As layer structure, though the effect of the structural differences becomes apparent in the distinct optical properties in the z direction. We emphasize that the dimensional difference is also visible in the static conductivity ($\Omega \to 0$). The ratio $\sigma^{xx}(0)/\sigma^{zz}(0)$, an indicator for the anisotropy, is 17 in LaMnAsO but only 7 in $BaMn_2As_2$.

For LaMnAsO the optical conductivity was measured using ellipsometry for a polycrystalline sample [24]. To compare the experimental results to our calculations, we average our theoretical results over all Cartesian directions to obtain a “polycrystalline

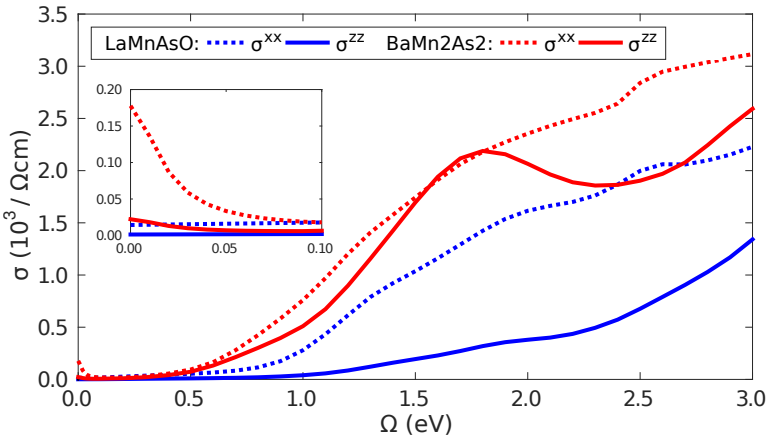

Figure 5.8.: Optical conductivity tensor components $\sigma^{zz}(\Omega)$ (solid lines) and $\sigma^{xx}(\Omega)$ (dotted lines) of $BaMn_2As_2$ (red) and LaMnAsO (blue) from fully charge self-consistent DFT+DMFT including uncorrelated bands outside the projective window. The inset shows the low frequency region of the optical conductivity in the same units as the main panel. This figure is taken from Ref. [174].

conductivity" (Fig. 5.9). In general, the spin-polarized DFT result (solid gray line) follows the trend of the experimental data (black circles), but it severely overestimates the optical conductivity, at some points by more than a factor of two. Similarly, the one-shot DFT+DMFT calculation (dashed blue line) cannot explain the experimental data. As discussed above, the static spin splitting leads to a larger gap, which is clearly visible in the suppressed optical conductivity below 1.5 eV. Additionally, the unoccupied Mn states are less correlated due to smaller electron-electron scatterings as compared to the fully charge self-consistent DFT+DMFT result. The consequence is a different distribution of the optical weight. On the other hand, in the fully charge self-consistent treatment, the optical results are not only influenced by the modified spectral function but also by the altered velocities of the updated Kohn-Sham bands. Indeed, the fully charge self-consistent DFT+DMFT calculations correctly reproduce the experimental result over a wide range of frequencies (dotted blue line).

The upper limit of our projective energy window is at 3.25 eV, but the chemical potential ($\mu = 1.6$ eV) effectively shifts this level down to 1.65 eV. If we also consider that the Fermi energy is close to the unoccupied states, we see that there can be transitions at $\Omega \approx 2$ eV, which are already not captured with our energy window. Of

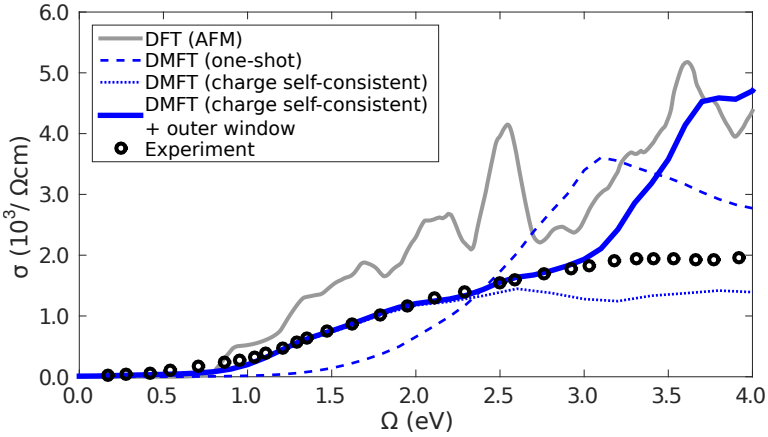

Figure 5.9.: Optical conductivity of LaMnAsO calculated with DFT (solid gray line), fully charge self-consistent DFT+DMFT in the correlated window (dotted blue line) and including uncorrelated bands (solid blue line) as well as one-shot DFT+DMFT (dashed blue line); compared to experimental data (black circles) from Ref. [24]. Above 3 eV DFT+DMFT (including the outer window) starts to deviate from the experimental data due to the onset of the La-4f bands, which are placed much too low in energy by DFT [125]. This figure is taken from Ref. [174].

course, this effect sets in very slowly as there are still many other transitions possible at $\Omega \approx 2\,\text{eV}$. To this end, we extend the trace in Eq. (3.23); now, the spectral function is a matrix built by a block A_{ij} for the correlated bands, as well as blocks for uncorrelated bands below and above the correlated subspace, $A_{\nu\nu'}$. Note that $A_{\nu\nu'} \sim \delta_{\nu\nu'}$ is a non-interacting DFT spectral function. The resulting optical conductivity yields excellent agreement with the experimental data up to about 3 eV (solid blue line). The strong increase above 3 eV is caused by the onset of the La-4f bands, which are known to be placed much too low in energy by DFT [125].

The remarkable agreement with experimental data underlines the importance of the fully charge self-consistent approach and suggests that our choice of the parameters U and J is appropriate. Furthermore, the experimental and theoretical results indicate that the direct band gap of bulk LaMnAsO may be well below the 1.4 eV obtained from thin-film measurements [25].

5.3.5. Further comparisons to experiments

Due to two recent publications on $BaMn_2As_2$ [207] and LaMnAsO [208], we supplement this chapter with a further comparison to this new experimental data.

We start our discussion with the valance-band photoemission (PE) spectrum for LaMnAsO measured at room temperature with a photon energy of $h\nu = 7.6\,\mathrm{keV}$ [208]. In Fig. 5.10 we compare the experimental spectrum[30] (dashed green line) to the total DFT+DMFT spectral function in the AFM phase (black line) and the total DFT DOS (blue line). Additionally, the projected DFT DOS of the O-2p orbitals (blue area), which are the determining states from $-5.5\,\mathrm{eV}$ to $-3.0\,\mathrm{eV}$, is shown. A notable discrepancy between experiment and theory is the difference in the total band width. If we assume that the small kink in the experimental data at about $-3.8\,\mathrm{eV}$ originates from the onset of the O-2p states, we might deduce that this discrepancy is caused by O-2p orbitals located approximately $0.8\,\mathrm{eV}$ too high in energy by DFT. We believe that this could be corrected in the DFT+DMFT calculation by treating the double counting as an effective parameter, adjusted such that the experimental spectrum is best reproduced (cf. Refs. [209, 210]).

Now we turn to ARPES measurements for $BaMn_2As_2$ single crystals [207]. In Fig. 5.11 we show the DFT+DMFT $\mathbf{k}$-resolved spectral function along the Γ to M high symmetry path, plotted in consistency with Fig. 3b of Ref. [207]. The different graphs illustrate the contribution of the Mn and As orbitals (left column) and the influence of the imaginary part of the self-energy (right column). At the used photon energy of $h\nu = 46.6\,\mathrm{eV}$ the ARPES measurement probes for the most part the Mn-3d orbitals due to the low cross section of the As-4p orbitals (see Fig. 4b of Ref. [207]). Thus, mainly the Mn-3d spectral function (middle left plot of Fig. 5.11) should be considered for the comparison to the experiment.

Overall, the DFT+DMFT result agrees extremely well with what is found in the experiment. All dispersive features of the spectral function are captured in the full energy range. Especially important is the good representation of the strongly pronounced bands close to the chemical potential at the Γ point. In this region the highest intensities are observed along the considered $\mathbf{k}$-path. Other high intensity regions are also

[30] We scaled the area of the PE spectrum such that it has the correct filling.

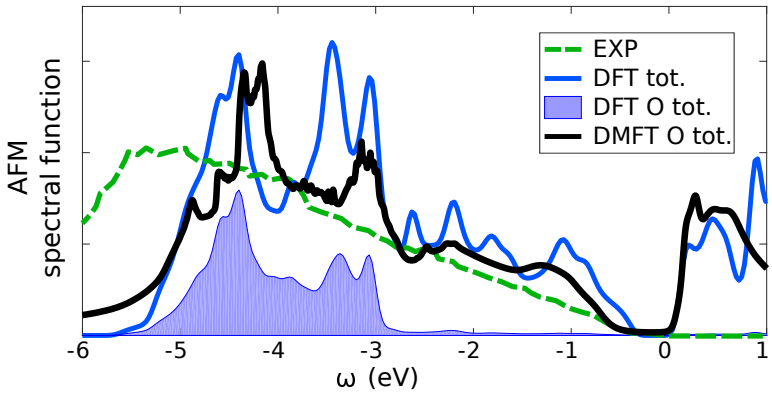

Figure 5.10.: Antiferromagnetic DFT+DMFT spectral function $A(\omega)$ (black line), total spin-polarized DFT DOS (blue line) and O-2p projected DFT DOS (filled blue area), compared to a recent room temperature valance-band PE measurement at $h\nu = 7.9\,\mathrm{keV}$ (dashed green line) [208]. The Fermi level is set to $\omega = 0\,\mathrm{eV}$.

found at the Γ point at $-2.6\,\mathrm{eV}$ and around the M point between $-3.0\,\mathrm{eV}$ and $-2.0\,\mathrm{eV}$. Even the lowest band with its bottom at the Γ point at approximately $-5.0\,\mathrm{eV}$ is present in experiment and theory.

One additional band, visible only in the experiment, with its bottom at the Γ point near $-1.7\,\mathrm{eV}$ cannot be explained with the DFT+DMFT spectral function. As this band is also not present in spin-polarized DFT calculations, it is argued in Ref. [207] that its likely origin are surface effects, which can be either caused by a magnetic or a crystal structure distortion. Of course, surface effects are not captured by our bulk DFT+DMFT calculations.

The little kink present in all graphs of Fig. 5.11, at about a quarter of the path from Γ to M, is an artifact of the projective Wannier function construction. Such kinks can occur if a band enters or leaves the (**k**-independent) energy window. In our case this is related to the fact that bands crossing the upper energy boundary still possess some minor Mn-3d character. Due to the already large energy window it is only a small artifact, however if this concerns bands with a strong character of the correlated orbitals the choice of the energy window should be reconsidered.

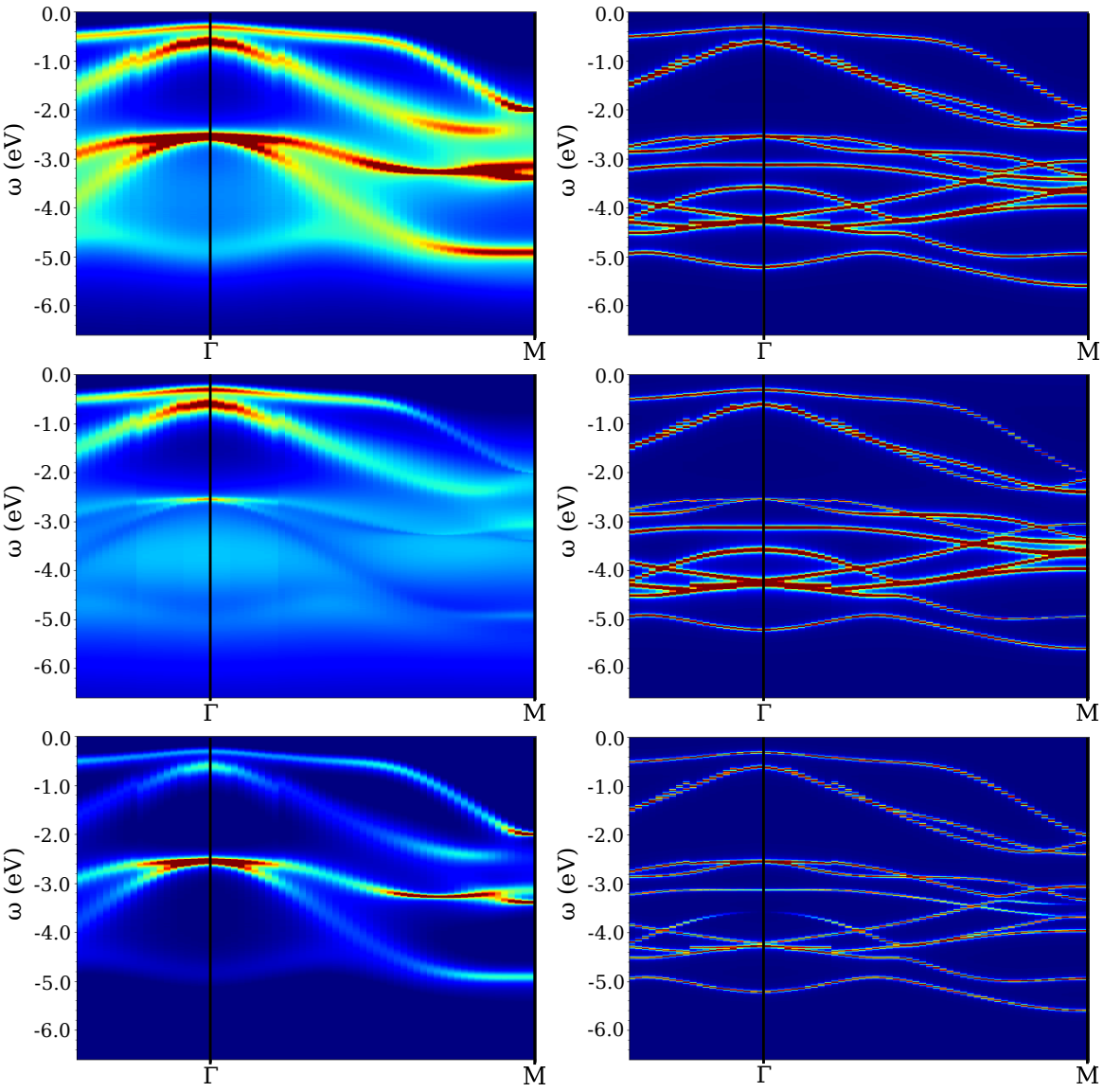

Figure 5.11.: Antiferromagnetic spectral functions $A(\mathbf{k}, \omega)$ for the occupied states of $BaMn_2As_2$ on the high symmetry $\mathbf{k}$-path between Γ and M. Left column: Full DFT+DMFT self-energy. Right column: Only the frequency-dependent real part of the self-energy is used and the imaginary part is set to $-0.015\,\text{eV}$. Top row: Total spectral function. Middle row: Mn-3*d* projected spectral function. Bottom row: As-4*p* projected spectral function. All figures are plotted with the same color range and color map. The limits of the energy axis and the $\mathbf{k}$-path are selected in accordance with the ARPES intensity plot ($h\nu = 46.6\,\text{eV}$) shown in Fig. 3b of Ref. [207]. The Fermi level is set to $\omega = 0\,\text{eV}$ in all graphs.

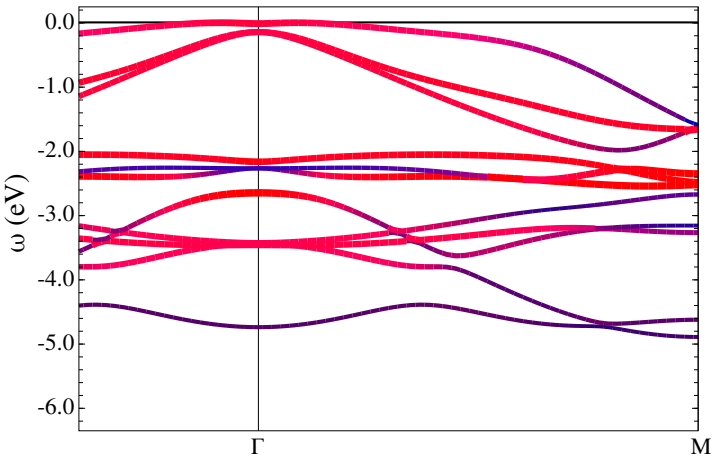

Figure 5.12.: Detail of the spin-polarized (antiferromagnetic) DFT band structure (cf. Fig. 5.11). The bands with Mn-3*d* character are colored in red and with As-4*p* character in blue, respectively. The Fermi energy is set to $\omega = 0.0\,\text{eV}$. The prima Wien2k add-on [211] was used to create this figure.

The right column of Fig. 5.11 shows the same information as the corresponding graphs on the left, but with the imaginary part of the self-energy set to $-0.015\,\text{eV}$ in the calculation of $A(\mathbf{k}, \omega)$. At first sight, this "band structure" is very similar to the spin-polarized (AFM) DFT band structure (shown in Fig. 5.12 for comparison). However, important difference of the top right plot in Fig. 5.11 and the band structure in Fig. 5.12 are, for example, apparent at the Γ point in the Mn-like bands. We observe that the bands below $-2.0\,\text{eV}$ are located about $1.0\,\text{eV}$ lower in energy in the DFT+DMFT result. The Mn-3*d* band slightly below $-2.0\,\text{eV}$ in the DFT band structure, is shifted below the two bands with As-4*p* character. This shows the importance of dynamical effects present in the real part of the self-energy. The weakly dispersing bands between $-4.5\,\text{eV}$ and $-3.0\,\text{eV}$ possess a strong Mn-3*d* character (middle right plot of Fig. 5.11) and exactly these bands are completely washed out if the imaginary part of the self-energy is restored (middle left plot of Fig. 5.11). In this energy region the imaginary part of the self-energy is about $-1.5\,\text{eV}$.

We have seen in Sec. 5.3.1 that the DFT and DFT+DMFT spectral functions differ quite substantially in the PM phase of $BaMn_2As_2$ and LaMnAsO. Certainly, non-spin-polarized DFT cannot correctly describe the localized nature of the corre-

lated compounds under investigation. This is not so much the case in the AFM ground state, where the DFT band structure fits relatively well to the DFT+DMFT results (see also Fig. 5.3). Overall, the occupied states show only a negligible band renormalization in DFT+DMFT, which would also indicating that the magnetism-induced static spin splitting (captured already in DFT) is the fundamental ingredient determining the spectrum. The authors of Ref. [207] attribute the negligible band renormalization of the occupied states in $BaMn_2As_2$ to this rather simple insight, and speculated that also the Hund's coupling could be strongly suppressing charge and spin-fluctuations in the Mn-3d shells. For the related 122-compound $BaCr_2As_2$ one-shot DFT+DMFT calculations show that the formation of ordered moments reduces the degree of correlations [212]. Subsequently, lower quasiparticle renormalizations in the AFM than in the PM phase are observed. In our calculations the estimated quasiparticle renormalizations in the AFM state, with Z ranging between 0.3 and 0.5 for the majority spin and between 0.6 and 0.7 for the minority spin, are still substantial, but also show the less correlated nature in comparison to the PM state. We want to add here that also the strong Mn-As hybridization of the occupied states is an important factor, as it might be responsible for a "pinning" of the band structure. On the other hand, the unoccupied states, which hybridize only very weakly with ligand orbitals (see Fig. A.2), are considerably renormalized in our DFT+DMFT calculation (Fig. 5.3).

In Ref. [212] it was shown for $BaCr_2As_2$ that using only density-density terms in the Hamiltonian does considerably alter the imaginary part of the self-energy (for $i\omega_n \rightarrow 0$). The standard outcome for the PM phase, where calculations without spin-flip and pair-hopping terms show stronger correlations due to the lower degeneracy of the atomic ground state, is reversed in the AFM case. Neglecting the spin-flip and pair-hopping terms reduces local spin fluctuations, which ultimately leads to a higher magnetic moment and reduced dynamic correlations [212]. We performed a density-density calculations for $BaMn_2As_2$ in the PM phase and observed an enhancement of dynamic correlations. Anyhow, this discussion points out the importance of the spin-flip and pair-hopping terms, which we take fully into account in all DFT+DMFT calculations for the manganese pnictides.

We want to emphasize that the experimental works [207, 208] addressed in this section were published after our work [174]. Therefore, the presented comparisons illustrate the capabilities of fully charge self-consistent DFT+DMFT.

5.4. Conclusion

We investigated the manganese pnictides $BaMn_2As_2$ and LaMnAsO in their paramagnetic and antiferromagnetic phases. These manganates represent two points along the dimensional crossover: While $BaMn_2As_2$ is quite isotropic with comparable couplings within and between the Mn-As layers, LaMnAsO is effectively two dimensional with only a weak residual interlayer coupling. This difference, which is already visible in the crystal structure, is substantiated, and its origins are accounted for by the maximally localized Wannier functions for the Mn-3d bands and their hopping amplitudes. We demonstrated that differences in physical properties such as the Néel temperature, the band gap, and the static as well as the optical conductivity can be traced back to a large extent to the difference in the effective dimensionality.

Our fully charge self-consistent DFT+DMFT calculations yield good agreement with experimental measurements of the optical conductivity and ARPES spectra. Our confidence in the applicability of the method to our compounds thus confirmed, we established that both materials are near a metal-insulator transition, which helps explain their high Néel temperatures. Our results constitute an important example where fully charge self-consistent DFT+DMFT is demonstrably superior to the one-shot approximation.

6. Thermopower of electron-doped LaMnAsO

Preamble

In this chapter we use DFT+DMFT to simulate electron-doped LaMnAsO. Methodical details, especially with respect to DFT+DMFT calculations under doping, are provided in Sec. 6.2. In Sec. 6.3 we first discuss the applicability of the virtual crystal approximation and then present the DFT and DFT+DMFT electronic structure of electron-doped LaMnAsO in the antiferromagnetic phase. Finally, we discuss the origin of the calculated Seebeck coefficients and put our results in the context of experimental observations.

G. Kraberger contributed the VASP super-cell DFT calculations. All other calculations, the analysis of the results, a literature study, and the discussion presented in this chapter were solely carried out by the author of this thesis.

6.1. Introduction

In times of a drastic increase in energy consumption alternative sources of electric energy become increasingly important. Thermoelectric materials can intrinsically convert heat into electric energy, and therefore they are often considered as an alternative source of power generation [45, 46]. Otherwise wasted heat, e.g. from car engines or power plants, can be utilized in an environmentally friendly way. The fact that the

power conversion through the Seebeck effect is essentially a material property opens the possibility of designing reliable, maintenance-free and long-living devices. Under these aspects, the investigations carried out in the following are not only of purely academic interest.

Studying the underlying microscopic mechanisms that promote high thermoelectricity is a pivotal aspect not only in the search of new thermoelectric materials, but also in view of tuning and improving existing ones by targeted structural modifications, e.g. chemical substitution, external deformation or even heterostructure design [44]. Although semiconductors are already used for certain applications (with Bi_2Te_3 [213] being the most famous one), there is still an urge to increase the efficiency of thermoelectric materials. The efficiency of a thermoelectric device is measured with the figure of merit $ZT = S^2T\sigma/\kappa$ [133], where T is the operating temperature, S the Seebeck coefficient, σ the electric conductivity, and κ is the thermal conductivity.[31] We will mainly focus on the Seebeck coefficient in the following.

Regarding the class of manganese pnictides, experiments have repeatedly reported remarkable thermoelectric properties. For example, a Seebeck coefficient of about $220\,\mu V\,K^{-1}$ was measured in $BaMn_2Sb_2$ single crystals at room temperature [37, 38]. This value further increased to $520\,\mu V\,K^{-1}$ by Zn doping of the Mn atoms ($BaMn_{1.7}Zn_{0.3}Sb_2$) [38]. On the other hand, $BaMn_2Bi_2$ crystals show a lower – but still high – Seebeck coefficient of $120\,\mu V\,K^{-1}$ at 300 K [39]. In polycrystalline samples of 1111 manganese pnictides similar values were measured. For example, hole doping in LaMnPO was experimentally achieved by a substitution of La with Ca or by a substitution of Mn with Cu [40]. These samples, with doping levels between 5% and 10%, exhibit a positive Seebeck coefficient in the range of 100 to $300\,\mu V\,K^{-1}$. Similarly, $S = 240\,\mu V\,K^{-1}$ for $La_{0.9}Sr_{0.1}MnAsO$ was reported at room temperature [41]. A negative Seebeck coefficient of $-350\,\mu V\,K^{-1}$ was measured for an oxygen-deficient $SmMnAsO_{0.925}$ sample [42]. Polycrystalline $LaMnAsO_{1-\delta}F_\delta$ samples with $\delta = 0.03$, 0.05, 0.07 and 0.1 were synthesized in Ref. [43]. The room temperature Seebeck coefficient of these samples increases from about $-290\,\mu V\,K^{-1}$ at 3% doping to about $-190\,\mu V\,K^{-1}$ at 7% doping and jumps to only $-30\,\mu V\,K^{-1}$ for a doping level of 10%.

[31] Optimizing ZT is a difficult task due to interdependencies of S, σ and κ [45]. Take for example the Wiedemann-Franz law for metals [48], $\sigma \sim \kappa T$; hence a high electric conductivity is usually accompanied by a high thermal conductivity.

These experimental findings call for an investigation of the thermoelectric properties exhibited by manganese pnictides. Still, fairly little work on the theoretical side is available in the literature. Only for $BaMn_2As_2$ the Seebeck coefficient was calculated within DFT and the const.-τ_s approximation, which resulted in values of around $200\,\mu V\,K^{-1}$ for hole doping and $-150\,\mu V\,K^{-1}$ for electron doping at 300 K [27].

In the same way, we will show for LaMnAsO that also in this manganese pnictide high Seebeck coefficients can be obtained already in the const.-τ_s approximation on the level of DFT calculations. Our subsequent analysis attributes the resulting values to a good extent to the peculiar properties of the band structure. However, these calculations have to be taken with care, as DFT+DMFT shows that the high Seebeck coefficient is actually a consequence of the special properties of the spectral function.

6.2. Methods

Besides the details stated in the following, our simulations were performed with the same settings and tools as used in Ch. 5. For each doping level we consider the same number of Bloch states by adjusting the (**k**-independent) energy window of the projective Wannier function construction for the Mn-3*d* orbitals. To be consistent with the previous chapter, we use for all doping levels the crystal structure of the undoped compound measured at 290 K [187]. The lattice parameters are only weakly influenced by the doping, and a test calculation performed with the experimental values of Ref. [43] for 10% electron doping showed no qualitative change in our results. Except stated otherwise, calculations in this chapter are carried out at room temperature ($\beta = 40\,eV^{-1}$). In all magnetic calculations we use the C-type AFM ordering as determined experimentally for the undoped compound [31].

We take the doping already into account on the DFT level. In Wien2k [117, 118] this can be accomplished with the virtual crystal approximation (VCA) [214], where the atomic numbers of the substituted atoms are modified according to the desired doping level. Additionally, we perform super-cell calculations using VASP 5.4.1 [147–150] with the projector augmented wave (PAW) method [215, 216] and pseudopotentials

v.54.[32] A plane wave energy cutoff of 400 eV is employed, consistent with the VASP default value for these pseudopotentials. Like in the Wien2k calculations, the PBE density functional [52] is used. The VASP super-cell calculations are performed with the same crystal structure parameters as used for the Wien2k calculations, apart from the modifications to achieve the doping effect in the super-cell. We obtain all results with the same lattice parameters, and thus possible doping-induced structural distortions are not taken into account. The full BZ of the super-cell is sampled with a $10 \times 10 \times 12$ Γ-centered Monkhorst-Pack [217] **k**-grid, whereas for the Wien2k calculation 10 000 **k**-points in the BZ of the initial cell, which is 9 times smaller in real space, are used.

6.3. Results

6.3.1. Virtual crystal approximation (VCA)

In practice, doping is often achieved by replacing a fraction of the open-shell atom (here Mn) by a similar element, preferentially to the left or right in the periodic table. Successful doping in LaMnAsO was accomplished by changing the charge of the La-O layers, which are sandwiched between the Mn-As layers, by a fractional replacement of the La atoms with Ca or Sr [41, 43], or by the fractional replacement of the O atoms with F or H [43, 186, 218]. The additional (or missing) charge on the La-O layers becomes a valence charge of the Mn-As layers, which in turn shifts the Fermi energy of the band structure. One could, thus, approximately model the effect of doping using a rigid energy shift of all bands without modifying the shape of the non-interacting DOS; this is the simplest way to take doping into account. Although appropriate in specific cases on the DFT level, it does not mean that shifting the correlated DFT+DMFT spectral function is justified.

A more advanced way of incorporating the effect of doping in band-structure methods is the virtual crystal approximation (VCA) [214]. The VCA neglects charge localization and assumes that there is a virtual atom on all possible sites which interpolates

[32] The pseudopotentials are: La 06Sep2000, Mn 06Sep2000, As 22Sep2009, O 08Apr2002, F 08Apr2002, Sr_sv 07Sep2000.

between the original atom and the dopant. In other terms, the VCA can be seen as a "delocalized" distribution of the additional carriers, where short-range order and local distortions are neglected. This approach is a mean-effect picture where no information specific to the dopant atom is incorporated. The picture of a virtual atom is only adequate for atoms with similar radii and the same number of core electrons. Therefore, the VCA is only believed to give reliable results for low doping levels and if the dopant is a neighboring atom in the periodic table. Computationally the VCA is an efficient way to simulate doping, because calculations can be carried out at the same cost as for the corresponding undoped structure.

Another possibility to incorporate doping effects is the super-cell approach, where the doped atoms are directly replaced by the dopant in a larger unit cell. Therefore, the dopants are incorporation in a translationally invariant way, which can be described as "maximally ordered" doping. Super-cells assume a long-range order of the dopants in the crystal matrix. Using this approach within DFT+DMFT is certainly feasible for high enough doping levels, however it would be much too demanding for the low doping levels used in this work due to the huge super-cells needed.

To be consistent with the experiment, we replaced the O atoms by F atoms for the electron doping case in a $3 \times 3 \times 1$ super-cell, which corresponds to a doping level of $11.\overline{1}\%$ (see inset of Fig. 6.1 top). Hole doping of the same level is taken into account by replacing La atoms in the same super-cell by Sr atoms (inset of Fig. 6.1 bottom). In Wien2k the electron doping is incorporated with the VCA by adjusting the atomic number of the O atoms to $Z = 8.11$. Likewise, the atomic number of La is adjusted to $Z = 56.89$ for hole doping.

In Fig. 6.1 we compare the VCA Wien2k DOS for electron- and hole-doped LaMnAsO to the super-cell calculations carried out with VASP. The agreement of VCA and the super-cell calculations is especially good in the energy region with no or only weak hybridization of the La-O and Mn-As layers, which is roughly between $-3\,\text{eV}$ and $2\,\text{eV}$. It should be also noted that the Mn-3d projected DOS are in even better agreement than the total DOS. The former is the more important quantity as only the Mn-3d orbitals are treated within DMFT.

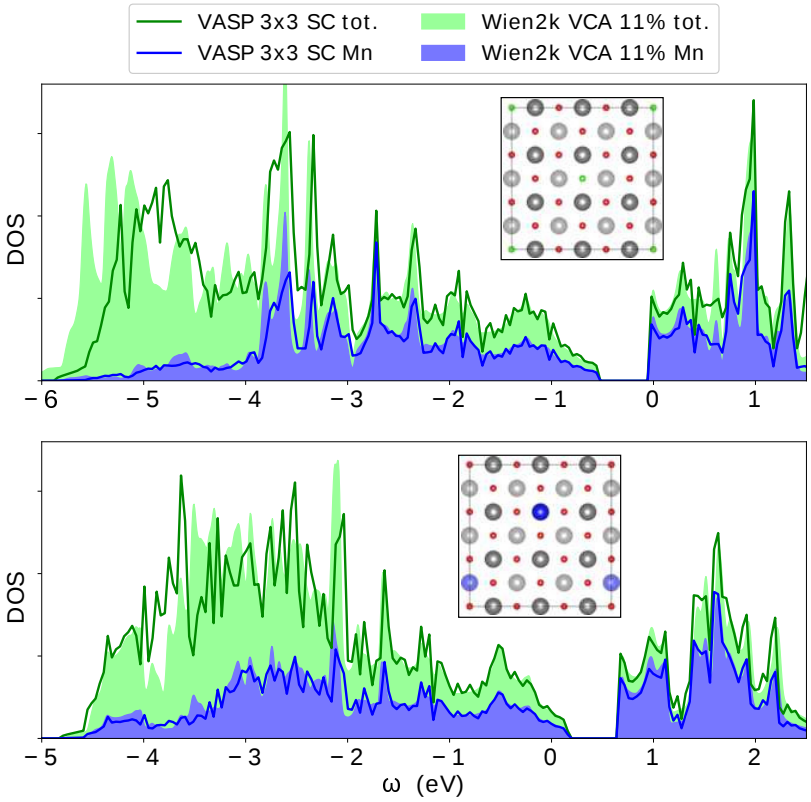

Figure 6.1.: Comparison of the total Wien2k VCA DOS in the antiferromagnetic state at 11% doping (filled areas) with the VASP super-cell (SC) DOS for a $3 \times 3 \times 1$ super-cell (lines), i.e. a doping of 11.11%. Top: Electron doping (substitution of O with F). Bottom: Hole doping (substitution of La with Sr). The total DOS is colored in green and the projected Mn-3*d* DOS in blue. In the insets (prepared with VESTA [154]), which show a top view of the La-O layer, the positions of the F atoms (green) substituting the O atoms (red) and the Sr atoms (blue) substituting the La atoms (grey) are indicated. The La and Sr atoms sitting below the O plane are lighter colored than those above. The Fermi energy is set to $\omega = 0\,\mathrm{eV}$. Note that the VCA cannot distinguish between dopants in the same column of the periodic table (e.g. Ba, Sr, Ca).

Of course, in energy regions exhibiting dopant states, one cannot expect a good agreement between VCA and the super-cell calculation. This is especially apparent from $-6\,\mathrm{eV}$ to about $-3\,\mathrm{eV}$, where the DOS is mainly determined by O states, i.e. the properties of the La-O layer. Super-cell calculations with a different arrangement of the dopants in the unit cell did not substantially change the DOS. We also compared the VCA and super-cell calculation for the non-spin-polarized state, because this is actually used as input for the DMFT calculation. An agreement is found on the same level as for the spin-polarized calculations (not shown). As we are mainly interested in spectral properties in the vicinity of the Fermi energy, which are to a great extent determined by the Mn-As layer, the comparison presented in Fig. 6.1 underlines that VCA is an eligible approximation for studying doped LaMnAsO. Similarly, for the earlier discussed $BaMn_2As_2$, it was shown with super-cell calculations that the main features of the undoped band structure were retained under a doping of 25% [29]. Hence, all results discussed in the remainder of this chapter are obtained with Wien2k and the VCA.

6.3.2. Spectral functions under electron doping

In this section we use the VCA and DFT+DMFT to simulate $LaMnAsO_{1-\delta}F_{\delta}$ with electron doping levels of $\delta = 3$, 5, 7 and 10%. We start our discussion with the total DFT+DMFT spectral functions $A(\omega)$ in the AFM phase (top left graph of Fig. 6.2). In comparison to undoped LaMnAsO (dashed line), doping has three major effects: First, there is some small spectral weight at the chemical potential. Second, the edge of the spectral function between 0.0 eV and 0.25 eV in the undoped compound is pushed towards $\omega = 0.0\,\mathrm{eV}$ when the doping level is increased. Although the slope of this edge is steeper in comparison to the undoped spectral function, it does not substantially change for the different doping levels. Third, additional weight below the chemical potential emerges, which increases with the doping level and develops into a shoulder, well visible for 10% doping. We will see below in the analysis of the **k**-resolved spectral function $A(\mathbf{k}, \omega)$ that the spectral weight appearing below the chemical potential is not the result of, e.g., an electron pocket, but is rather incoherent weight originating from electronic correlations.

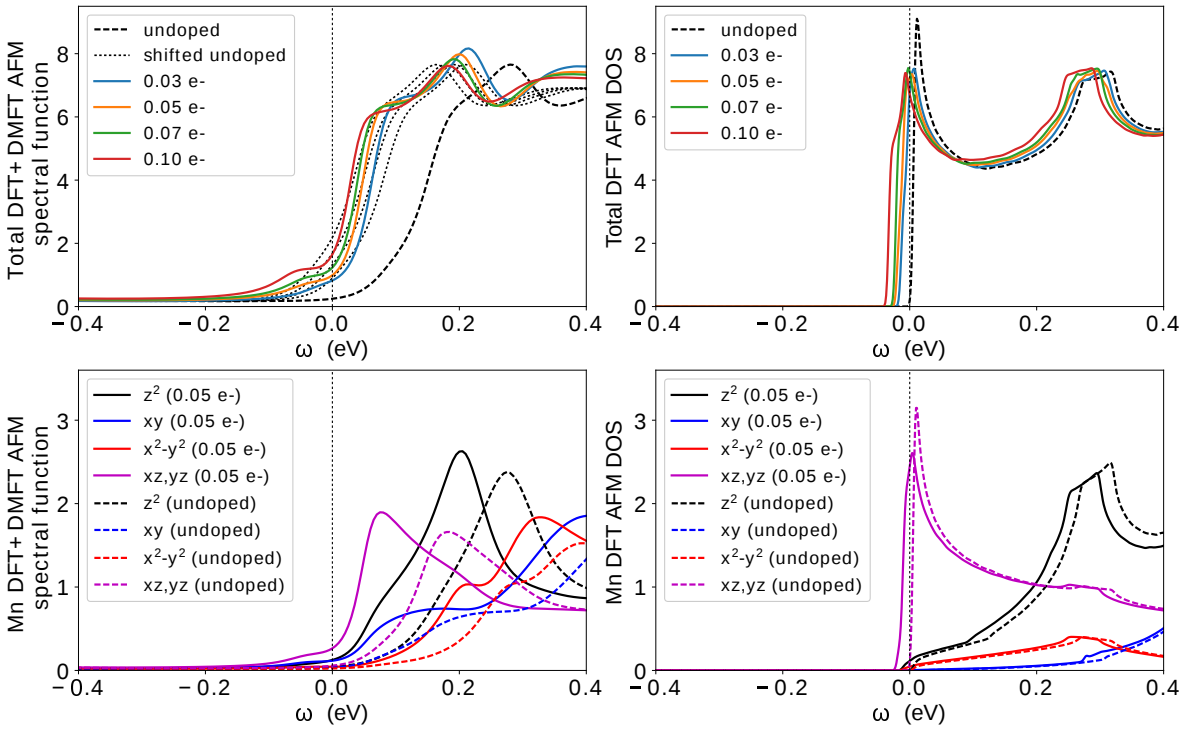

Figure 6.2.: Top left: Evolution of total DFT+DMFT antiferromagnetic spectral functions for 3, 5, 7 and 10% electron doping (colored lines). The undoped spectral function (dashed black line) is shown for comparison and a simple energy shift of it, adjusted to a filling corresponding to the four doping levels, is indicated by the dotted black lines. Bottom left: DFT+DMFT orbital-resolved spectral functions of the correlated Mn atom (sum of up and down spin) for 5% electron doping (solid lines) compared to the undoped spectral functions (dashed lines). Top right: Evolution of total antiferromagnetic DFT DOS for 3, 5, 7 and 10% electron doping (colored lines). Additionally, the undoped spectral function (dashed black line) shifted by $-0.51\,\mathrm{eV}$ is shown. This shift was determined such that the onset of the unoccupied states is at the Fermi energy. Bottom right: DFT orbital-resolved DOS of the Mn atoms for 5% electron doping (solid lines) compared to the (shifted) undoped spectral functions (dashed lines).
Note that the doping levels given in the legends are per O atom, but the total spectral function is shown for a unit cell containing two atoms of each kind (2 LaMnAsO). The magenta lines in the bottom graphs correspond to only one orbital and *not* the sum of the xz and yz orbitals. The Fermi level is set to $\omega = 0.0\,\mathrm{eV}$ and is indicated by the vertical dotted black line in all graphs.

Additionally, we show in Fig. 6.2 (top left) spectral functions which are generated by simply shifting the undoped spectral function by $\Delta\omega$ according to the different doping levels (dotted black lines). These energy shifts $\Delta\omega$ are determined by integrating from 0.0 eV up to $\Delta\omega$, such that the area corresponds to δ. The fact that not much spectral weight is present in the first 0.05 eV above the chemical potential result in a substantial shift already for the lowest doping level of 3%. A further increase of the doping gives only small additional shifts. Importantly, these simple energy shifts do not correctly reproduce the three effects mentioned in the above paragraph, and are therefore not justified on the level of the DFT+DMFT spectral function.

In the bottom left graph of Fig. 6.2 we present the Mn-3d orbital projected spectral function for the undoped compound and for an electron doping of 5%. In undoped LaMnAsO, the lowest unoccupied weight is mainly of xz/yz character (dashed magenta line, see also Sec. 5.3.1), and unsurprisingly the low-energy properties of these two orbitals are affected the most by the doping (full magenta line).[33] This is manifested in the position of the peak present in the undoped xz/yz spectral function at about 0.2 eV, which lies more than -0.14 eV lower in energy at 5% doping. On the contrary, the positions of the peaks present in the spectral functions of the other orbitals are shifted by only about -0.07 eV. Additional spectral weight develops below the chemical potential and the slope of the xz/yz becomes considerably steeper under doping. Note that at the chemical potential the spectral weight of the z^2 and the x^2-y^2 orbitals is much lower than the xz/yz weight. Furthermore, we observe that the small shoulder in the z^2 spectral function around 0.1 eV is not present in the undoped spectral function.

The total and the Mn-3d orbital projected spin-polarized (AFM) DFT DOS are shown in the right graphs of Fig. 6.2. In Wien2k the Fermi energy E_F of an insulator is defined by the valance band edge. For a better comparison to the doped results we shift the undoped DOS by -0.51 eV, such that the onset of the unoccupied states is at E_F. Like in DFT+DMFT, also the DFT DOS shows that the degenerate xz/yz orbitals dominate the low-energy region. However, in the doped case the spectral weight at E_F is about 10 times larger and the DOS in the vicinity of E_F is sharply peaked in comparison to the DFT+DMFT spectral function. The slope of the DFT DOS does not become steeper with doping and also the additional spectral weight below E_F is not observed.

[33] The magenta lines in Fig. 6.2 correspond to only one orbital and *not* the sum of the xz/yz orbitals.

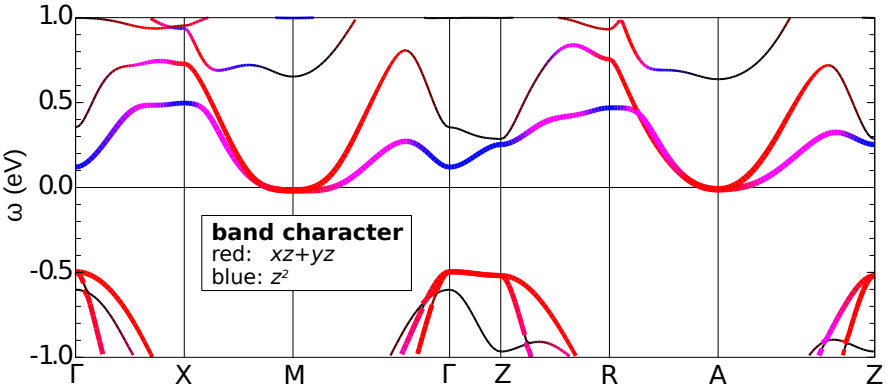

Figure 6.3.: Spin-polarized (antiferromagnetic) DFT band structure along the **k**-path shown in Fig. A.3. The band character of the summed up and down spin of the xz/yz orbitals is colored in red and the z^2 orbitals are colored in blue, respectively. The prima Wien2k add-on [211] was used to create this figure. The Fermi energy is set to $\omega = 0.0\,\text{eV}$.

The DFT band structure for 5% electron doping is shown in Figs. 6.3, where the bands are colored according to their characters: red for the xz/yz orbitals and blue for the z^2 orbital. The DFT picture is that of a band insulating LaMnAsO which becomes metallic under doping as E_F is shifted into the unoccupied states. The doping is mainly affecting the hole pockets of the xz/yz orbitals at the A and M points. Especially at the M point the bands are rather flat, resembling a mold-like shape. For all electron doping levels (> 0) the bottom of the bands at the A and M points lies below E_F.

We turn now to the correlated DFT+DMFT band structure $A(\mathbf{k}, \omega)$ shown in the top graph of Fig. 6.4. Already in the discussion of Fig. 5.3 we have seen that electronic correlations lead to important differences in comparison to the DFT band structure. Around the A and M points the spectral weight has a stronger pronounced flat part than the corresponding DFT bands, e.g. apparent in the lowest unoccupied DFT band on the path from M to Γ. Up to the middle of the path this band is relatively flat in energy in the DFT+DMFT result, but substantially more dispersive in the DFT band structure. The middle and bottom graphs of Fig. 6.4 show that these strong spectral weights have the same orbital character (xz/yz) like in the DFT calculation. Away from the M and A points the character of the lowest band changes to z^2 and xy (see bottom graph of Fig. 6.4). These orbitals are strongest visible in the weakly dispersing spectral weight between the Γ and Z point.

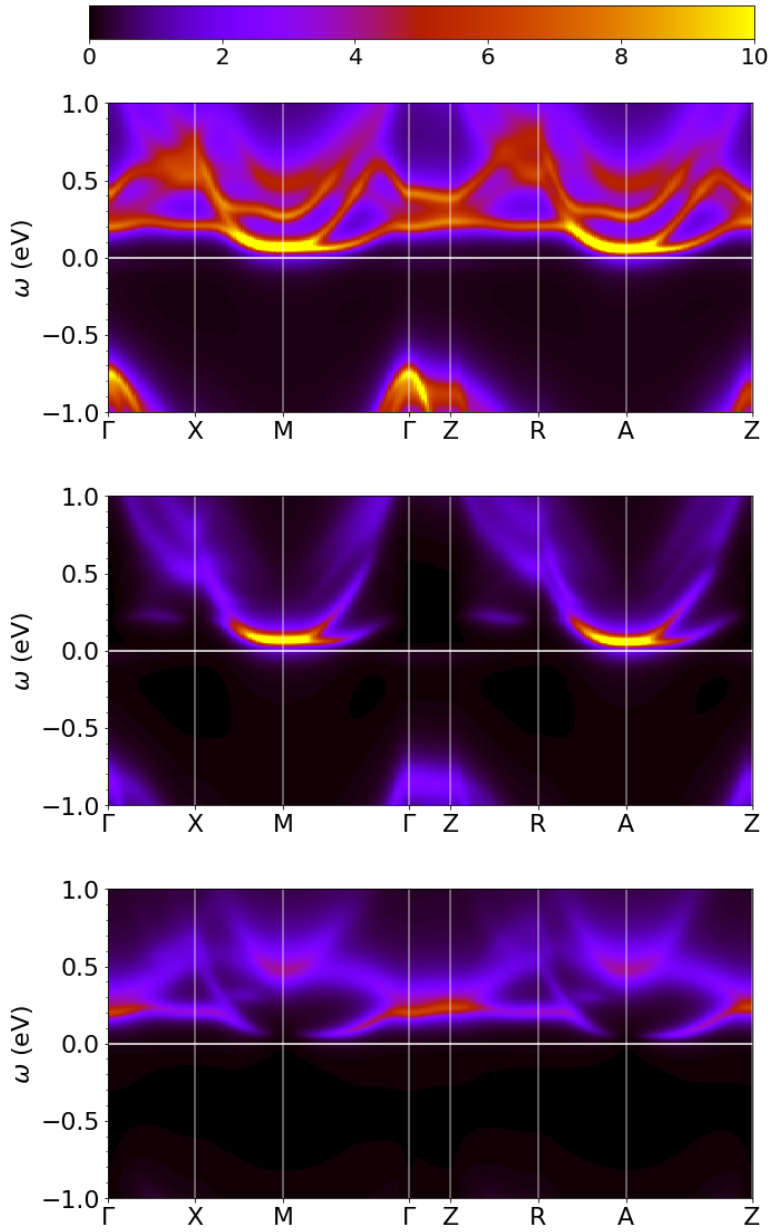

Figure 6.4.: Correlated spectral functions $A(\mathbf{k}, \omega)$ at 5 % electron doping on the BZ path shown in Fig. A.3. Top: Total spectral function, Middle: Projection onto the xz and yz orbitals, Bottom: Projection onto the z^2 and xy orbitals. All figures are plotted with the same color range and color map. The Fermi level is set to $\omega = 0.0\,\text{eV}$ in all graphs.

Another consequence of electronic correlations is the emergent incoherent weight of the electronic states, which can be seen from the washed out spectral features in Fig. 6.4. In the DFT+DMFT calculation the effect of doping is to move the chemical potential into the incoherent part, present due to $\Im\Sigma(\omega)$, of these states. To be more precise, an artificial band structure, where only $\Re\Sigma(\omega)$ is used and $\Im\Sigma(\omega)$ is set to zero, does not have bands crossing E_F (not shown here). In sharp contrast to the DFT result, the prominent spectral features in the correlated band structure at the A and M point lie clearly above the chemical potential.

The fact that the bottom of the xz/yz bands is below E_F in DFT, whereas the pronounced spectral features of these orbitals are still located above the chemical potential in DFT+DMFT, does lead to a completely different interpretation of the high Seebeck coefficients in electron-doped LaMnAsO. Overall, the special case of relatively flat spectral features around the chemical potential constitutes an interesting case for the Seebeck coefficient, because both, a high asymmetry in the spectral function and, at the same time, a high asymmetry in the velocities is present. To what extent these asymmetries influence the Seebeck coefficient is the focus of the following section.

6.3.3. Seebeck coefficient and its origin

Due to the ω-factor in the kinetic coefficient $K_1^{\alpha\alpha'}$ (Eq. 3.25), electron contributions (with $\omega > 0$) and hole contribution (with $\omega < 0$) influence the Seebeck coefficient S in an opposite way. Having a high electron-hole asymmetry, i.e. a strongly asymmetric transport distribution $\Gamma^{\alpha\alpha'}$ (Eq. 3.23), is a necessary ingredient for a high $K_1^{\alpha\alpha'}$, and in turn a high S. There are two different mechanisms to promote a strong asymmetry in $\Gamma^{\alpha\alpha'}$, as there are likewise two quantities entering $\Gamma^{\alpha\alpha'}$: the velocity matrices $v^{\alpha}(\mathbf{k})$ and the spectral function $A(\mathbf{k},\omega)$.

The obvious situation, which is shown in sketch (1) of Fig. 6.5, is to have a very asymmetric spectral function $A(\mathbf{k},\omega)$, i.e. a steep slope of the spectrum close to E_F [219–221]. A high positive Seebeck coefficient is expected if there are many more states below E_F than above and a high negative Seebeck coefficient for cases with many more states above E_F than below, respectively. Thus, a high Seebeck coefficient can be understood on the level of the DOS. In the context of strongly correlated systems this picture was

also discussed with regard to a sharp Kondo peak directly above or blow the chemical potential [145, 222]. An indicator for the influence of the asymmetry present in the spectral function is to evaluate S (Eq. 3.25) with $v^{\alpha}(\mathbf{k}) = \text{const.} \times \mathbb{1}$. In this case the velocities drop out and we end up with[34]

$$S^{v=\mathbb{1}} = -\frac{\int d\omega \ \beta\omega \left(-\partial f\left(\omega\right)/\partial\omega\right) \sum_{\mathbf{k}} \operatorname{Tr} A^2(\mathbf{k},\omega)}{\int d\omega \ \left(-\partial f\left(\omega\right)/\partial\omega\right) \sum_{\mathbf{k}} \operatorname{Tr} A^2(\mathbf{k},\omega)} \ . \tag{6.1}$$

In the literature it was pointed out that not just an asymmetry in $A(\mathbf{k},\omega)$, but also peculiar band shapes can strongly enhance the Seebeck coefficient [223–225]. In this scenario, a strong asymmetry is found directly in $v(\mathbf{k})$. If we assume a constant isotropic scattering time τ_s, the kinetic coefficients (Eq. 3.35) can be approximated as [223]

$$K_0 \sim \sum_{\mathbf{k}} \left(v_A^2(\mathbf{k}) + v_B^2(\mathbf{k})\right) \qquad K_1 \sim \sum_{\mathbf{k}} \left(v_A^2(\mathbf{k}) - v_B^2(\mathbf{k})\right) \ . \tag{6.2}$$

Here the summation runs only over states in the range of $|\omega - E_F| \lesssim 1/\beta$. The velocities v_A^2 and v_B^2 are characteristic velocities for the states above (A) and below (B) E_F. A linear dispersion in the vicinity of E_F means that $v_A^2 \approx v_B^2$, and thus K_1 will be low, like it is the case for usual metals [223]. The optimal situation for a high S are "pudding-mold"-like bands which are non- or only weakly-dispersive below/above E_F and show a strongly dispersive behavior above/below E_F (see sketch (2) in Fig. 6.5). If E_F is located close to the flat portion of a band and the temperature is high enough, we find $v_A^2 \gg v_B^2$, and consequently $K_1 \sim v_A^2$. In general, asymmetries in $v(\mathbf{k})$ provide an opposing picture and add a second facet to the theoretical understanding of materials with good thermoelectric properties.

Of course, $v(\mathbf{k})$ and $A(\mathbf{k},\omega)$ are intertwined and for real materials the influence of the electronic structure on the thermoelectric properties should be always considered as an interplay of these two ingredients [226, 227]. A band structure showing a strong asymmetry in $v(\mathbf{k})$ usually comes with an asymmetry in $A(\mathbf{k},\omega)$, which can be such that it will partially compensate the asymmetry in $v(\mathbf{k})$. For example, it was shown that this is the case in $Na_{0.7}CoO_2$ [226]. Coming back to sketch (2) in Fig. 6.5, one

[34] For a better readability we omit the directional indices α and α' in the remainder of this chapter.

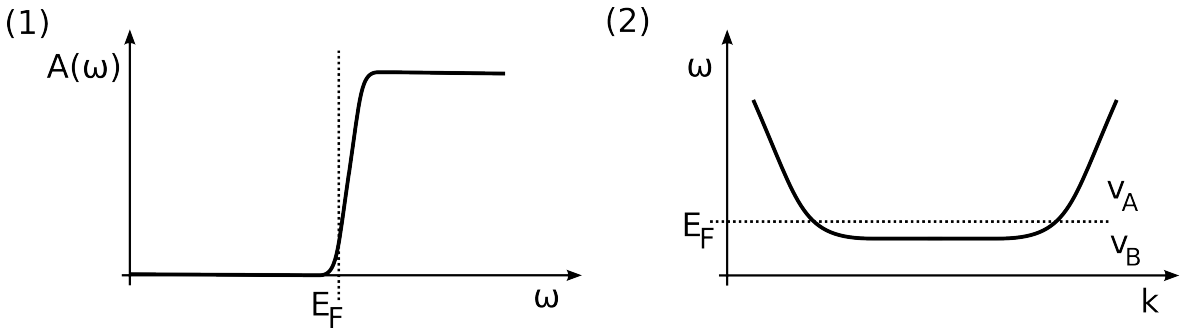

Figure 6.5.: Sketch of two scenarios promoting a high Seebeck coefficient. (1): Particle-hole asymmetry in the spectral function $A(\omega)$. (2): Asymmetry in the velocities $v_A \gg v_B$ due to the flat portion of the band below the Fermi energy E_F and a high dispersion above.

would expect many more states below E_F, and thus also a much higher spectral function below E_F. For energies above E_F the spectral function would sharply diminish to a lower value. However, if the bending point of the band is very close to E_F and the temperature high enough, one could again have a scenario where more states above E_F contribute in total. This would not compensate the effect of the asymmetry in $v(\mathbf{k})$, but even enhance S. We will show below, in the discussion of Fig. 6.6, that this is indeed the case for LaMnAsO in the const.-τ_s approximation.

We have seen in Ch. 5 and in Sec. 6.3.2 that in both quantities, $v(\mathbf{k})$ and $A(\omega)$, asymmetries are present in LaMnAsO. In the remainder of this section we will focus on how these thermoelectrically-favorable properties influence the Seebeck coefficient.

As all experimentally synthesized samples of LaMnAsO (doped and undoped) are polycrystalline, we simulate a "polycrystalline" Seebeck coefficient by averaging over the three Cartesian coordinates (see also Eq. B.3) [228]

$$S_{av} = \frac{S^{xx}\sigma^{xx} + S^{yy}\sigma^{yy} + S^{zz}\sigma^{zz}}{\sigma^{xx} + \sigma^{yy} + \sigma^{zz}} \,. \tag{6.3}$$

We show the averaged Seebeck coefficient S_{av} as a function of electron doping level in Fig. 6.6. The DFT+DMFT S_{av} in the AFM phase is $-290\,\mu\mathrm{V\,K^{-1}}$ at 3% doping and increases up to $-190\,\mu\mathrm{V\,K^{-1}}$ for 10% doping (blue circles). At a doping of 3% the

calculated value coincides with the experimental data [43] (black circles), but considering the uncertainties present on the experimental and the theoretical side, also the results at doping levels of 5 and 7% are still in very good agreement. However, the DFT+DMFT S_{av} deviates from the experimental result at 10% doping. On the other hand, in the PM DFT+DMFT calculations S_{av} is only $-40\,\mu\mathrm{V\,K^{-1}}$ at 5% doping and $-15\,\mu\mathrm{V\,K^{-1}}$ at 10% doping (blue squares). The large discrepancy at 5% doping in comparison to the AFM result suggest that the magnetic ground state, which is a property most manganese pnictides share, is, at least at lower doping levels, an essential ingredient to describe the thermoelectric properties of LaMnAsO. Controversially, at 10% doping we actually find that the PM solution agrees better with the experiment.

Interestingly, the experimental measurement of the conductivity as a function of temperature reveals a rather abrupt change to a clearly metallic regime at a doping level of 10% [43]. This might be connected to a magnetic phase transition as also a 14% H doping leads to the destruction of the AFM ground state in LaMnAsO [186]. A similar behavior has been observed for $SmMnAsO_{1-\delta}$ samples [42]. In this compound the Seebeck coefficient is $S = -350\,\mu\mathrm{V\,K^{-1}}$ for an oxygen-deficiency of $\delta = 0.075$ and $S = -280\,\mu\mathrm{V\,K^{-1}}$ for $\delta = 0.17$ at room temperature. However, upon a further increase of doping it jumps to only $-40\,\mu\mathrm{V\,K^{-1}}$ for $\delta = 0.2$. The Néel temperature of the $\delta = 0.2$ sample is about 30 K, whereas no transition to a PM state is observed up to the highest measured temperature of 400 K for the samples with lower dopings. Clearly, further experimental investigation would be necessary to definitely determine the magnetic state of $LaMnAsO_{0.9}F_{0.1}$ at room temperature.

Although we initially break the spin-symmetry in the AFM DFT+DMFT calculations, the system is in principle free to converge to the PM solution, as it does indeed at high enough temperatures (see Sec. 5.3.3). However, even for 10% electron doping we find the AFM ground state strongly prevailing. The ordered magnetic moment only reduces by $0.1\,\mu_B$/Mn in comparison to the undoped result, and also the total energy clearly favors the AFM phase. In the same way as DMFT is not reliable in predicting the absolute value of magnetic transition temperatures (cf. Sec. 5.3.3), we do not expect DMFT to correctly describe a possible transition from the AFM to the PM phase with increasing doping levels due to the mean-field character of the theory.

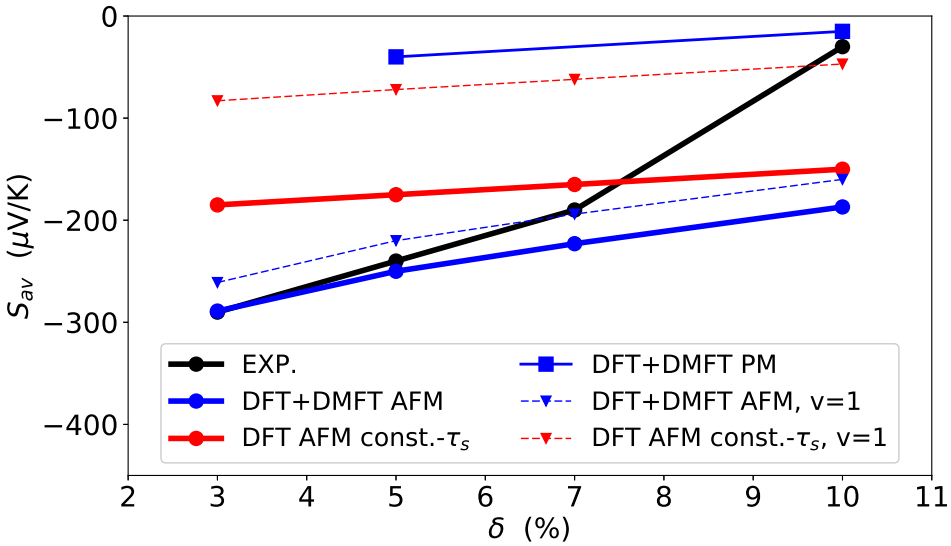

Figure 6.6.: Averaged Seebeck coefficient S_{av} as a function of the electron doping level δ calculated with spin-polarized (antiferromagnetic) DFT+const.-τ_s (red circles), DFT+DMFT in the antiferromagnetic phase (blue circles), DFT+DMFT in the paramagnetic phase (blue squares) and compared to experimental results from Ref. [43] (black circles). The dashed lines correspond to the evaluation of S_{av} with $v(\mathbf{k}) = \mathbb{1}$ (Eq. 6.1) for the antiferromagnetic DFT+DMFT result (blue triangles) and the DFT result (red triangles). The lines are a guide to the eye.

Using spin-polarized DFT and the const.-τ_s approximation,[35] we also obtain high negative values for S_{av} (red circles in Fig. 6.6). At 10% doping the DFT+const.-τ_s S_{av} is comparable to the DFT+DMFT result, but at 3% doping $|S_{av}|$ is by more than $100\,\mu\mathrm{V\,K^{-1}}$ smaller than the DFT+DMFT value and the experimental data.[36] On a qualitative level, one might argue that already the const.-τ_s approximation is sufficient to provide an understanding of the high Seebeck coefficient. However, the evaluation of $S_{av}^{v=\mathbb{1}}$, using Eqs. 6.1 and 6.3, reveals a completely different interpretation for the two approaches (red and blue triangles in Fig. 6.6).

[35] In the TRIQS/DFTTools transport code we achieve this by setting $\Sigma(\omega) = -i/\tau_s$ with $1/\tau_s = 0.05\,\mathrm{eV}$. Note that the actual value of τ_s is not relevant as it cancels in the calculation of S.

[36] In contrast to PM DFT+DMFT, the non-spin-polarized DFT+const.-τ_s calculation even results in a positive Seebeck coefficient of $10\,\mu\mathrm{V\,K^{-1}}$ at 5% doping and $15\,\mu\mathrm{V\,K^{-1}}$ at 10% doping.

In the DFT+const.-τ_s calculation $|S_{av}^{v=\mathbb{1}}|$ is about $100\,\mu\mathrm{V\,K^{-1}}$ smaller than $|S_{av}|$, i.e $|S_{av}|$ reduces by 60-70% when the velocity matrices $v(\mathbf{k})$ are set to $\mathbb{1}$, suggesting that the asymmetry in $v(\mathbf{k})$ are a dominant ingredient of $|S_{av}|$. This insight is supported by our analysis of the band structure and the spectral function in the previous section. The rather flat bottom of the xz/yz bands lying below E_F and their more dispersive character above E_F (see Fig. 6.3) already indicates a strong influence of $v(\mathbf{k})$ on S_{av}. Furthermore, the asymmetry in the DOS (top right graph of Fig. 6.2) does not compensate the $v(\mathbf{k})$ asymmetry, but rather gives a contribution with the same sign, confirmed by the negative values of $S_{av}^{v=\mathbb{1}}$ for all doping levels in the DFT+const.-τ_s results (red triangles in Fig. 6.6). We attribute this to the fact that at $\beta = 40\,\mathrm{eV^{-1}}$ there are still more relevant states above E_F than below; selected by the derivation of the Fermi function in Eq. 3.25 (cf. Fig. 3.1 and the top right graph in Fig. 6.2).

On the other hand, the same analysis for the DFT+DMFT calculation shows only a slight reduction of $|S_{av}|$ by about 15% when setting $v(\mathbf{k}) = \mathbb{1}$. Therefore, we draw the conclusion that in this case the asymmetry in the DFT+DMFT spectral function is the determining factor for the Seebeck coefficient of LaMnAsO. Again, we can deduce this already from the spectral function and the correlated band structure (Figs. 6.2 and 6.4). Here we have strongly pronounced spectral features present slightly above the chemical potential, leading to a considerable spectral asymmetry. The situation is such that v_A^2 and v_B^2 are small, but $v_A^2 \approx v_B^2$.[37]

Clearly, the flat bands, i.e. spectral features of the xz/yz orbitals, are the decisive ingredient for the Seebeck coefficient in electron-doped LaMnAsO, but the ways how the specific properties of these bands enhance the Seebeck coefficient are completely different in the DFT+const.-τ_s approximation and the DFT+DMFT calculation. Due to the strong effect of the electronic correlations on the unoccupied states of LaMnAsO, and the better agreement with experiments, we are convinced that DFT+DMFT provides the appropriate picture for understanding the observed Seebeck coefficients.

Additionally, we show in Tab. 6.1 the Seebeck coefficient calculated at 5% doping for a lower temperature of 145 K ($\beta = 80\,\mathrm{eV^{-1}}$). In the DFT+const.-$\tau_s$ calculation the difference is basically a narrowing of the energy window by the derivative of the Fermi function. However, within DFT+DMFT we have to perform a full calculation

[37] Even if v_A^2 and v_B^2 are small, the Seebeck coefficient can still be high, because the velocities enter both coefficients K_0 and K_1.

at the new β, because also the correlated $A(\mathbf{k}, \omega)$ changes with temperature. It turns out that $|S_{av}|$ is a little bit lower than at room temperature in both approaches. In DFT+const.-τ_s the difference to $S_{av}^{v=\mathbb{1}}$ is still $100\,\mu\mathrm{V\,K^{-1}}$. We infer that the effect of the velocity asymmetry is roughly the same as at room temperature, whereas the contribution from the spectral function is slightly lower. This is plausible, because the narrower energy window effectively captures less unoccupied states in the DFT DOS (cf. Fig. 3.1 and the top right graph in Fig. 6.2). For the DFT+DMFT calculation, deducing from the spectral function at room temperature, one would expect a much lower $|S_{av}|$ at the two times lower temperature. However, this is compensated by an even stronger asymmetric $A(\omega)$ at $T = 145\,\mathrm{K}$ (not shown).

Although the agreement of the calculated DFT+DMFT Seebeck coefficients for electron-doped LaMnAsO with experimental data is intriguing, we should, for the sake of a conscientious discussion, put this comparison into a broader perspective. On the theoretical side the details of DFT+DMFT can have an influence on the resulting Seebeck coefficients, as the double counting, the analytic continuation, and the interaction values U and J have an effect on the precise shape of the spectral function. For example, increasing or decreasing the input error of the Beach algorithm by a reasonable factor of 5 can change S by about 20%. Due to the strong hybridization of the Mn-3d orbitals with the As-4p orbitals below the chemical potential, the details of the occupied spectral function might be influenced by the double counting, choice, because it determines the effective location of the Mn-3d states with respect to the As-4p bands. We think that this is less severe for the unoccupied states, which have mainly Mn-3d character (cf. Fig. A.1). Anyhow, we emphasize that we did not modify the double counting and the interaction parameters with regard to the calculations in Ch. 5.

On the other hand, also the experimental data has to be treated with care, because it is obtained from only one polycrystalline sample per doping level [43]. Indeed, measurements for the related compound LaMnPO, which has overall very similar physical properties [22], show Seebeck coefficients scattered from $-100\,\mu\mathrm{V\,K^{-1}}$ to $-300\,\mu\mathrm{V\,K^{-1}}$ for undoped samples [40]. This wide range of Seebeck coefficients is attributed to the non-stoichiometry of the synthesized samples, because the chemical composition is difficult to control precisely (especially the anion ratio P:O). Further, the fact that an undoped LaMnAsO sample and a sample with 5% Ca doping show both $S \approx 340\,\mu\mathrm{V\,K^{-1}}$ [43] might point towards difficulties in the synthesis of precise doping levels.

Table 6.1.: Averaged Seebeck coefficients S_{av} and $S_{av}^{v=\mathbb{1}}$ (in $\mu V\,K^{-1}$) of LaMnAsO calculated with DFT+const.-τ_s and DFT+DMFT at 5% electron doping and temperatures of 145 K (top) and 290 K (bottom).

T = 145 K	DFT+const.-τ_s	DFT+DMFT
S_{av}	−150	−230
$S_{av}^{v=\mathbb{1}}$	−50	−205

T = 290 K	DFT+const.-τ_s	DFT+DMFT
S_{av}	−170	−250
$S_{av}^{v=\mathbb{1}}$	−70	−220

Finally, for thermoelectric applications not only S is crucial, but more so the power-factor $S^2\sigma$ (numerator of ZT). The calculated out-of-plane conductivity σ^{zz} of electron-doped LaMnAsO is about a factor 50 lower in our DFT+DMFT calculations and still 5 to 10 times lower in DFT+const.-τ_s than the in-plane conductivity σ^{xx} (not shown). As we have seen in Sec. 5.3, this is a consequence of the quasi-two-dimensional nature of LaMnAsO. The crystal symmetries demand equal properties of the in-plane directions, i.e. $\sigma^{xx} = \sigma^{yy}$ and $S^{xx} = S^{yy}$. Thus, following from Eq. 6.3, the averaged Seebeck coefficient is mainly determined by its in-plane value $S_{av} \approx S^{xx}$. Interestingly, the difference in the dimensionality is not pronounced in the direction dependent Seebeck coefficient itself. For all studied doping levels in the AFM phase $|S^{zz}|$ is less than $40\,\mu V\,K^{-1}$ smaller than $|S^{xx}|$.

Putting everything together, the in-plane direction offers a similarly high Seebeck coefficient, but exhibits a much higher conductivity than the out-of-plane direction. Therefore, we predict that a possible single-crystalline $LaMnAsO_{1-\delta}F_\delta$ sample should show the highest power-factor if thermoelectricity is harvested in the in-plane direction.

6.4. Conclusion

In this chapter we studied LaMnAsO under electron doping in the framework of fully charge self-consistent DFT+DMFT. To incorporate an effective electron doping we employed the virtual crystal approximation on the DFT level, which we first demonstrated to give reasonable results by a comparison to VASP super-cell calculations. A detailed study of the effect of doping on the DFT and DFT+DMFT (**k**-resolved) spectral functions revealed a completely different picture. On the DFT level, the doping pushes the Fermi energy into the flat xz/yz bands, with the bottom of the bands below the Fermi energy. On the contrary, the incorporation of electronic correlations within DMFT shows that doping leads to incoherent weight below the chemical potential, whereas stronger pronounced spectral features are still located above it. We investigated the implications of these differences on the Seebeck coefficient by emphasizing the role of the magnetic ground state, the contribution of band-structure effects and the degree of particle-hole asymmetry in the spectral function. In principle, it might be possible to further enhance the present asymmetries with a targeted modification of the crystal structure, e.g. by applying external pressure. At this point, we leave such investigations open for future works.

7. Conclusions

This thesis dealt with the description of strongly correlated materials; namely $SrVO_3$, $BaMn_2As_2$, LaMnAsO and Sr_2RuO_4. A special emphasis was geared on the calculation of transport quantities (optical conductivity, Seebeck coefficient and Hall number) in a post-processing step to DFT+DMFT calculations. To this end, we presented the transport code of the TRIQS/DFTTools package.

We started with $SrVO_3$, one of the simplest correlated materials, for which we have discussed various DFT+DMFT results including transport properties. Despite being branded as benchmark material in the DMFT community, we were able to reveal an atomic multiplet structure in the upper Hubbard band provided by the recently developed FTPS impurity solver. The first observation of a distinct multiplet structure in a real-material calculation is an important affirmation of the atom-centered view promoted by DMFT. We showed that such spectral features cannot be resolved with conventional CTQMC impurity solvers, because then the calculation of real-frequency spectra is plagued by the necessary ill-posed analytic continuation.

The core focus of this thesis was the investigation of the manganese pnictides $BaMn_2As_2$ and LaMnAsO in their paramagnetic and antiferromagnetic phases. We analyzed the properties of these two compounds within the framework of fully charge self-consistent DFT+DMFT. In our study of the paramagnetic phase, we established that both materials are close to the Mott metal-insulator transition, which helps explain their high Néel temperatures. Additionally, we substantiated the differences between the two materials, which are already present on the level of the crystal structure. A maximally localized Wannier function analysis of the real-space Hamiltonian for the Mn-3d orbitals confirmed that LaMnAsO can be classified as effectively two-dimensional material with only a weak interlayer coupling. On the other hand, $BaMn_2As_2$ is much more

three-dimensional due to the substantial coupling of the Mn-As layers. We demonstrated that differences in physical properties such as the Néel temperature, the band gap, and the optical conductivity can be traced back largely to this difference in the effective dimensionality. Furthermore, by a comparison of (**k**-resolved) spectral functions and transport quantities to experimental data, we confirm our confidence in the applicability of DFT+DMFT to the compounds under consideration. The presented results constitute an important example where fully charge self-consistent DFT+DMFT is superior to one-shot calculations.

Finally, we studied the electronic influences on the Seebeck coefficient of electron-doped LaMnAsO. To model experimentally synthesized $LaMnAsO_{1-\delta}F_{\delta}$ we employed the virtual crystal approximation for electron doping levels of δ = 3, 5, 7 and 10%. Our analysis showed that the xz/yz orbitals are the decisive ingredient to understand the observed Seebeck coefficients. In DFT+DMFT electronic correlations lead to incoherent spectral weight below the chemical potential, whereas the more strongly pronounced spectral features of these orbitals are located above it. We demonstrated that this is in sharp contrast to the spin-polarized DFT results, where the bottom of the xz/yz bands lies below the Fermi energy. Both, DFT and DFT+DMFT calculations, predict considerably high Seebeck coefficients, however with completely opposing underlying mechanisms. While DFT points towards a picture where the asymmetry in the velocities is pivotal, DFT+DMFT traces the Seebeck coefficient almost exclusively back to the asymmetry of the correlated spectral function. We predict that a possible single-crystalline $LaMnAsO_{1-\delta}F_{\delta}$ sample would exhibit the highest power-factor if thermoelectricity is harvested in the in-plane direction.

Our work shows the importance of electronic correlations for the understanding of manganese pnictides, which opens new paths towards a targeted modification of these materials to, e.g., further enhance their thermoelectric properties.

A. DFT band structure of $BaMn_2As_2$ and LaMnAsO

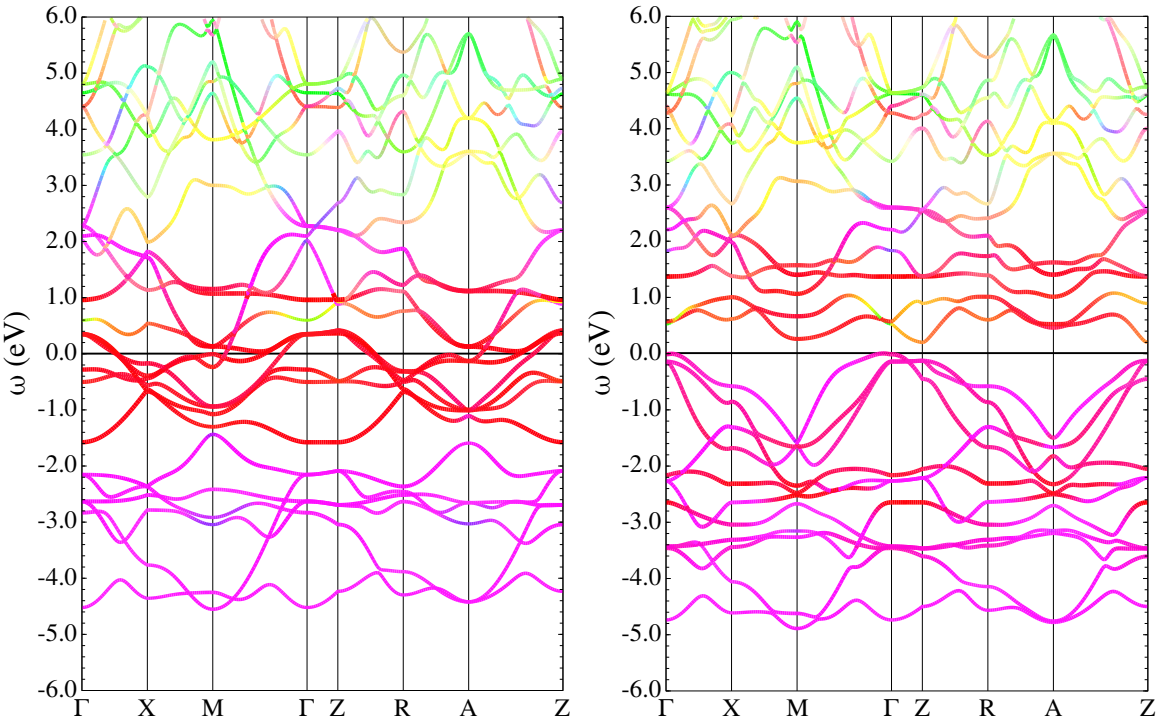

Figure A.1.: $BaMn_2As_2$ total non-spin-polarized (left) and spin-polarized (right) DFT (GGA-PBE) band structure along the BZ path shown in Fig. A.3. The bands are colored according to their character: green for Ba, red for Mn and blue for As. Note that in the antiferromagnetic ground state (right) the up and the down spins are equal in the total band structure. The Fermi energy is set to $\omega = 0.0\,\mathrm{eV}$. The prima Wien2k add-on [211] was used to create this figure.

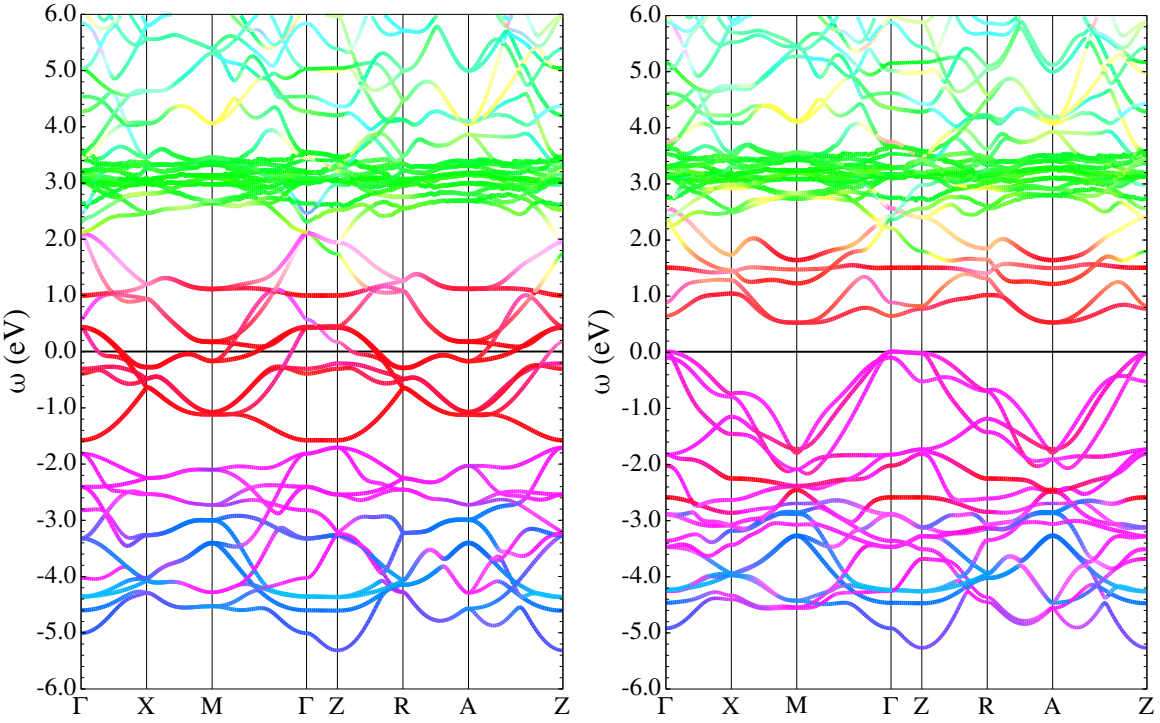

Figure A.2.: LaMnAsO total non-spin-polarized (left) and spin-polarized (right) DFT (GGA-PBE) band structure along the BZ path shown in Fig. A.3. The bands are colored according to their character: green for La, red for Mn and blue for As and O. Note that in the antiferromagnetic ground state (right) the up and the down spins are equal in the total band structure. The Fermi energy is set to $\omega = 0.0\,\text{eV}$. The prima Wien2k add-on [211] was used to create this figure.

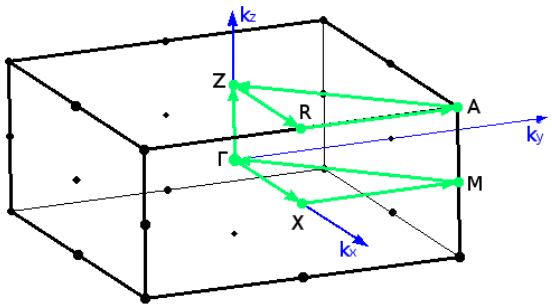

Figure A.3.: High symmetry points and **k**-path (green arrows) through the conventional unit cell of LaMnAsO and $BaMn_2As_2$. This figure was generated with XCrySDen [229].

B. Hall number of Sr_2RuO_4

Preamble

In this appendix we investigate how electronic correlations influence the temperature dependence of the Hall number of Sr_2RuO_4. The presented calculations and discussions were carried out by the author of this thesis. A. Georges, O. Parcollet, J. Mravlje, and M. Aichhorn greatly contributed to the analysis of the results. A. Georges initiated this project.

B.1. Motivation

We aim to shed light on the unusual temperature behavior of the Hall number R_H of Sr_2RuO_4. Experiments show a rather complex temperature dependence of R_H [230–233].[38] Below 1 K R_H is essentially temperature independent ($-1.2 \times 10^{-10}\,\mathrm{m^3\,C^{-1}}$), but with increasing temperature a rapid rise of R_H from its $T < 1\,\mathrm{K}$ value to zero at about 30 K (green triangles in Fig. B.3) is observed. After a positive maximum of $0.1 \times 10^{-10}\,\mathrm{m^3\,C^{-1}}$ at $T \approx 80\,\mathrm{K}$ R_H starts a slow decay and becomes negative again at about 120 K.

In contrast to the distinct temperature behavior of R_H, the Seebeck coefficient S is purely positive in the full temperature range up to 1000 K [234–236]. A maximum in S is found around 400 K [236]. The signs of both transport quantities, S and R_H,

[38] In our discussion we only consider the experimental findings of Refs. [231–233]. Although the first measurement of R_H, presented in Ref. [230], shows a similar temperature behavior, the detailed values differ. This is possibly related to the fact that this measurement was performed under a higher magnetic field.

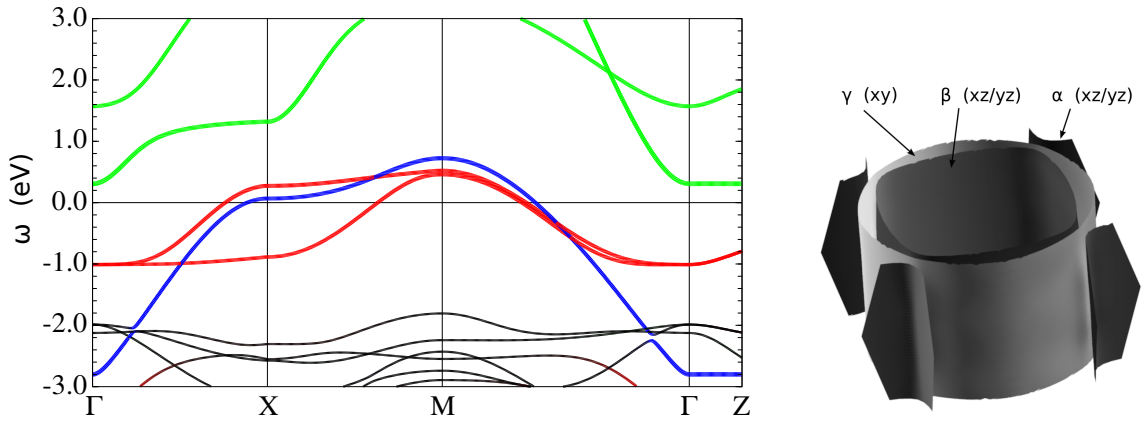

Figure B.1.: Left: Sr_2RuO_4 DFT band structure along the BZ path Γ-X-M-Γ-Z. The Ru bands with xy character are colored in blue, the xz and yz in red and the x^2-y^2 and z^2 in green. The prima Wien2k add-on [211] was used to create this band structure. The Fermi energy is set to $\omega = 0.0\,\text{eV}$. Right: Fermi surface of Sr_2RuO_4 showing the hole-like α sheet and the electron-like β and γ sheets. This Fermi surface was generated with XCrySDen [229].

carry information on the type of carrier (hole or electron) in a material. At first sight, the opposite signs, outside the intermediate temperature region ($30\,\text{K} > T > 120\,\text{K}$), might seem contradicting, but it is actually a clear indication for Sr_2RuO_4 being a multi-carrier system. This is also verified by the DFT band structure and the Fermi surface (Fig. B.1). The bands with Ru-xy character (blue) and Ru-xz/yz character (red) cross the Fermi energy and thus determine the low-energy physics. The Fermi surface consists of the hole-like α sheet centered at the M point and two electron-like sheets (β and γ) in the center of the BZ. The γ sheet can be attributed to the xy orbitals, whereas the α and β sheets show xz/yz character. The weakly dispersive nature on the Γ-Z path of the band structure and the cylindrical shape of the Fermi surface are a consequence of the layered crystal structure.

Assured of the multi-band nature of Sr_2RuO_4, we will show now that different signs of S and R_H can result from differences in averaging individual contributions to these transport quantities (see also Refs. [234, 237, 238]). We start with S and two type of carriers (with index h for holes and e for electrons) and assume a temperature gradient in x direction. For diagonal σ and S, this results in an electric field and a current also pointing in x direction. Therefore, we neglect the directional index in the following and note that σ and S are only scalar numbers. Using Eq. 3.1, the individual currents

are given as

$$j_e = \sigma_e E + \sigma_e S_e \nabla T \quad \text{and} \quad j_h = \sigma_h E + \sigma_h S_h \nabla T \ , \tag{B.1}$$

which sums to a total current of

$$j = j_e + j_h = (\sigma_e + \sigma_h) E + (\sigma_e S_e + \sigma_h S_h) \nabla T = \sigma E + \sigma S \nabla T \ . \tag{B.2}$$

By comparing to prefactors of E and S we see that the total static conductivity σ and the total Seebeck coefficient S are

$$\sigma = \sigma_e + \sigma_h \quad \text{and} \quad S = \frac{\sigma_e S_e + \sigma_h S_h}{\sigma_e + \sigma_h} \ . \tag{B.3}$$

This means that σ is the sum of the individual contributions (e.g. holes and electrons), but S is averaged with weights given by the individual conductivities.[39]

For R_H we assume an external magnetic field in z direction and an electric field in x direction. The induced currents in y direction $j^\perp$ (perpendicular to the applied electric and magnetic fields) are (Eq. 3.1)

$$j_e^\perp = \sigma_{H,e} E B \quad \text{and} \quad j_h^\perp = \sigma_{H,h} E B \ . \tag{B.4}$$

Again, we have dropped the directional indices. With Eq. 3.9, which further simplifies here to $\sigma_H = \sigma^2 R_H$, we obtain for the total perpendicular current

$$j^\perp = j_e^\perp + j_h^\perp = \left(\sigma_e^2 R_{H,e} + \sigma_h^2 R_{H,h}\right) E B = \sigma^2 R_H E B = (\sigma_e + \sigma_h)^2 R_H E B \ , \tag{B.5}$$

where we have used Eq. B.3 in the last step. From Eq. B.5 follows the average of R_H

$$R_H = \frac{\sigma_e^2 R_{H,e} + \sigma_h^2 R_{H,h}}{(\sigma_e + \sigma_h)^2} \ . \tag{B.6}$$

In comparison to Eq. B.3, we see that the individual R_H are multiplied by the square of the corresponding conductivities. In general, S_e and $R_{H,e}$ are negative and S_h and $R_{H,h}$ are positive. However, it becomes apparent from the different averages in Eqs. B.3 and B.6 that certain regions of σ_e/σ_h can exist where S and R_H show opposite signs.

[39] Exactly the same way of averaging is used in Eq. 6.3 to obtain a "polycristalline" S for LaMnAsO.

B.2. Methods

Similar to the ordinary conductivity σ^{xx}, expressed in terms of the derivatives $\partial\epsilon^\nu_{\mathbf{k}}/\partial k^\alpha$ and the spectral function $A(\mathbf{k},\omega)$ (Eq. 3.31 with $n = 0$), the Hall conductivity σ_H^{xyz} can be described with [15, 239]

$$\sigma_H^{xyz} = \frac{2N_\sigma\pi^2}{3V}\int d\omega\left(-\frac{\partial f}{\partial\omega}\right) \times\sum_\nu\sum_{\mathbf{k}}\left(\frac{\partial\epsilon^\nu_{\mathbf{k}}}{\partial k^x}\right)\left(\left(\frac{\partial\epsilon^\nu_{\mathbf{k}}}{\partial k^y}\right)\frac{\partial^2\epsilon^\nu_{\mathbf{k}}}{\partial k^x\partial k^y} - \left(\frac{\partial\epsilon^\nu_{\mathbf{k}}}{\partial k^x}\right)\frac{\partial^2\epsilon^\nu_{\mathbf{k}}}{(\partial k^y)^2}\right)A^{\nu\nu}(\mathbf{k},\omega)^3\ . \quad \text{(B.7)}$$

In contrast to σ^{xx} (Eq. 3.31), Eq. B.7 requires the evaluation of second derivatives of the Bloch band dispersion $\epsilon^\nu_{\mathbf{k}}$.[40] Eq. B.7 is in principle a single-band formulation (see Sec. 3.3); off-diagonal elements of the velocity matrices are neglected and only a simple sum over the individual bands ν is performed. Whether this is justified for Sr_2RuO_4 will be tested on the level of σ and S in Sec. B.3. Like for the other transport quantities, the derivatives are taken with respect to the bare (unrenormalized) dispersion, but many-body effects are incorporated via the correlated spectral function $A(\mathbf{k},\omega)$. Note that $A(\mathbf{k},\omega)$ enters Eq. B.7 with its 3rd power. In the context of strongly correlated systems Eq. B.7 was used in Ref. [241]. Therein, correlations were taken into account with a quasiparticle approximation for $A(\mathbf{k},\omega)$ and quasiparticle renormalizations obtained from DMFT self-energies.

The calculation of the $\epsilon^\nu_{\mathbf{k}}$ derivatives is not a trivial task. We take advantage of the implementation in the BoltzTraP code [141], which evaluates Eq. B.7 in the const.-τ_s approximation. To this end, it offers a stable way to obtain the derivatives of $\epsilon^\nu_{\mathbf{k}}$. The basic idea is the following: First, for each band an inverse Fourier transform is performed to real space ($H_0(\mathbf{k}) \rightarrow H_0(\mathbf{r})$). Usually, the number of $\mathbf{r}$-points is chosen to be the same as the number of $\mathbf{k}$-points so that the same information is carried by the quantities $H_0(\mathbf{k})$ and $H_0(\mathbf{r})$. However, BoltzTraP performs the Fourier transform to a

[40] An alternative equation for σ_H was derived by Itoh (Eq. 2.30 in Ref. [240]). Surprisingly, it does not require second derivatives and σ_H is only given in terms of the spectral function and the velocity matrices. However, our numerical tests for simple single-band models showed that the results are only equivalent to Eq. B.7 in some special cases. The likely source of the error is in the step from A10 to A11 in the appendix of Ref. [240]. We believe that the used symmetrization would also require a change of the sign, which prohibits the remaining derivation after this step.

denser **r**-grid and uses the gained additional freedom to minimize a roughness function (see Ref. [141] for details). The back transform opens the possibility to change the initial **k**-grid, or to use a denser **k**-grid, which is basically a Fourier interpolation. The benefit of this scheme is that it provides an "analytical" expression for $\epsilon^\nu_{\mathbf{k}}$, and thus allows to evaluate $\epsilon^\nu_{\mathbf{k}}$, $\partial\epsilon^\nu_{\mathbf{k}}/\partial k^\alpha$ and $\partial^2\epsilon^\nu_{\mathbf{k}}/\partial k^\alpha \partial k^{\alpha'}$ on an arbitrarily dense **k**-mesh. The BoltzTraP package offers a Wien2k interface, however we have modified the code for our specific purposes. This involves the option to write the $\epsilon^\nu_{\mathbf{k}}$ derivatives to data files on a customized output **k**-grid. Further, this output data can be split into multiple files to allow for a batch-by-batch processing in the evaluation of R_H, providing a simple way to parallelizing the computation. Additionally, we reduce the computational demand by incorporating the crystal symmetries.

We perform one-shot DFT+DMFT calculations for Sr_2RuO_4 at inverse temperatures between $\beta = 200\,\mathrm{eV}^{-1}$ and $25\,\mathrm{eV}^{-1}$ (cf. Tab. B.2 for the used β and the corresponding temperatures in K). In accordance with Ref. [242], we use a Kanamori Hamiltonian with $U_K = 2.3\,\mathrm{eV}$ and $J_K = 0.4\,\mathrm{eV}$. The projective energy window is set to $\mathcal{W} = [-3.0, 1.0]\,\mathrm{eV}$ with respect to the Fermi energy. For the analytic continuation we employ the Padé approximation [95, 96] and the stochastic analytic continuation method by Beach [101] (Sec. 2.5).

Initially, we perform the DFT+DMFT calculation on a $21 \times 21 \times 21$ **k**-mesh in the full BZ. For the conductivity and the Seebeck coefficient obtained with the Wien2k *optics* velocity matrices (shown in Tab. B.1) a $80 \times 80 \times 80$ **k**-mesh is used. In the calculation of R_H an even denser **k**-mesh is necessary, and thus we use BoltzTraP to generate a Fourier interpolated $\epsilon^\nu_{\mathbf{k}}$ (and its first and second derivatives) on a $250 \times 250 \times 250$ **k**-grid in the full BZ. Considering the crystal symmetries, in total 996 282 **k**-points have to be processed.

B.3. Results

Before we discuss the Hall number R_H, we want to judge the importance of inter-band transitions for the transport properties of Sr_2RuO_4. We calculate σ and S, once with off-diagonal elements of the Wien2k *optics* velocity matrices and once without (Tab. B.1, "with off-diag" and "no off-diag" rows).

Table B.1.: Influence of the velocity off-diagonal elements on the conductivity σ and the Seebeck coefficient S in x and z direction. The results for $\beta = 50\,\mathrm{eV}^{-1}$ are shown in the top table and for $\beta = 100\,\mathrm{eV}^{-1}$ in the bottom one, respectively. We use the full Wien2k *optics* velocity matrices in the "with off-diag" rows. The "no off-diag" rows show the results for calculation on the same **k**-grid without off-diagonal elements. Additionally, we perform calculations with velocities from BoltzTraP $\partial\epsilon^{\nu}_{\mathbf{k}}/\partial k^{\alpha}$ ("BoltzTraP" rows). Note that these results are obtained on a denser **k**-grid. For all calculations we use self-energies analytically continued with the Beach method.

$\beta = 50\,\mathrm{eV}^{-1}$	S^{xx} ($\mu\mathrm{V\,K}^{-1}$)	S^{zz} ($\mu\mathrm{V\,K}^{-1}$)	σ^{xx} ($\mathrm{m\Omega}^{-1}\,\mathrm{cm}^{-1}$)	σ^{zz} ($\mathrm{m\Omega}^{-1}\,\mathrm{cm}^{-1}$)
with off-diag	31.8	35.0	497	2.4
no off-diag	31.9	44.7	493	1.8
BoltzTraP	32.1	43.5	493	1.9

$\beta = 100\,\mathrm{eV}^{-1}$	S^{xx} ($\mu\mathrm{V\,K}^{-1}$)	S^{zz} ($\mu\mathrm{V\,K}^{-1}$)	σ^{xx} ($\mathrm{m\Omega}^{-1}\,\mathrm{cm}^{-1}$)	σ^{zz} ($\mathrm{m\Omega}^{-1}\,\mathrm{cm}^{-1}$)
with off-diag	21.2	24.9	1370	5.4
no off-diag	21.2	27.1	1366	4.8
BoltzTraP	21.2	26.7	1360	5.0

In the in-plane direction neglecting the off-diagonal elements results in a deviation of less than 1% from the value obtained with the full velocity matrices. On the other hand, such an agreement is not found for the z direction, where deviations of more than 20% are present. Therefore, we conclude that for in-plane transport quantities the off-diagonal elements of the velocity matrices can be neglected. Eq. B.7 is presumably sufficient to describe the Hall effect in Sr_2RuO_4, because only x/y derivatives of $\epsilon^{\nu}_{\mathbf{k}}$ are relevant in the evaluation of the in-plane R_H.

Further, we show the results of evaluating σ and S with the BoltzTraP derivatives $\partial\epsilon^{\nu}_{\mathbf{k}}/\partial k^{\alpha}$. As expected, they compare well to σ and S calculated with the diagonal part of the Wien2k *optics* velocities (see Sec. 3.3). We note that these calculations have been performed on a denser **k**-grid (cf. Sec. B.2), and thus an exact agreement cannot be expected. Overall, S agrees well with experimental data [234–236] of about $19\,\mu\mathrm{V\,K}^{-1}$ for $\beta = 100\,\mathrm{eV}^{-1}$ and $26\,\mu\mathrm{V\,K}^{-1}$ for $\beta = 50\,\mathrm{eV}^{-1}$.

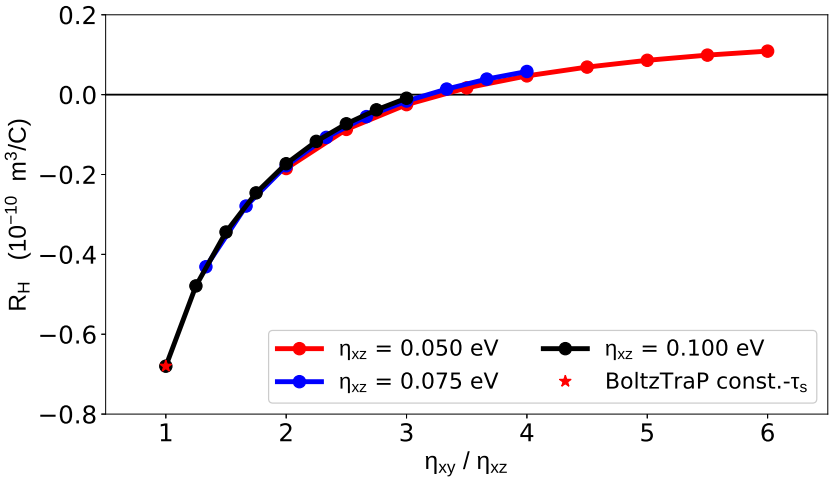

Figure B.2.: Hall number R_H of Sr_2RuO_4 calculated with Eq. B.7 using orbital-dependent constant scattering rates η_{xy} and η_{xz}. The ratio η_{xy}/η_{xz} is measured on the x axis. Different colors (red, blue, and black) correspond to different values of η_{xz} while η_{xy} is varied. For $\eta_{xy}/\eta_{xz} = 1$ we also show the result obtained with the BoltzTraP code [141] (red star).

Now, we turn to the discussion of R_H within the simplest approximation, using just a constant, but *orbital-dependent*, scattering rate η ($\Sigma(\omega) = -i\eta$) for the xy and the xz/yz orbitals. We vary the ratio η_{xy}/η_{xz} between 1 and 6 (Fig. B.2).[41] Already with this simple approach we are able to obtain a sign change in R_H. With increasing η_{xy}/η_{xz}, the Hall number increases monotonically from its lowest negative value of $-0.68 \times 10^{-10}\,\mathrm{m^3\,C^{-1}}$ to become positive at around $\eta_{xy}/\eta_{xz} = 3$. Interestingly, the resulting R_H does not depend on the specific values of the scatterings, as seen in the very similar R_H for different η_{xz}, i.e. the black, blue, and red lines fall on top of each other. Although R_H increases rather quickly as long as it is negative, it levels off and reaches the highest calculated value of $0.11 \times 10^{-10}\,\mathrm{m^3\,C^{-1}}$ at $\eta_{xy}/\eta_{xz} = 6$. This behavior suggests that, for even higher η_{xy}/η_{xz}, the Hall number would not exceed $R_H \approx 0.2 \times 10^{-10}\,\mathrm{m^3\,C^{-1}}$. As it should be, our result at $\eta_{xy}/\eta_{xz} = 1$ coincides with the BoltzTraP result (red star) within the const.-τ_s approximation. Even tough our approximation seems quite crude, the range of the resulting R_H agrees with what is observed in the experiment, where R_H ranges between $-1.2 \times 10^{-10}\,\mathrm{m^3\,C^{-1}}$ and $0.1 \times 10^{-10}\,\mathrm{m^3\,C^{-1}}$ (green triangles in Fig. B.3).

[41] Note that $\eta_{xz} = \eta_{yz}$.

As the next step, we use the calculated DFT+DMFT self-energies to obtain a material-specific estimate for the ratios η_{xy}/η_{xz}. Undoubtedly, the imaginary part of the self-energies at $\omega = 0$, i.e. $\omega_n \to 0$, will have the strongest influence on R_H due to the derivative of the Fermi function present in Eq. B.7 (cf. Fig. 3.1). First, we use a polynomial of 4^{th} order to fit the lowest 5 points of the Matsubara self-energies and extrapolate $\Im\Sigma\left(i\omega_n \to 0\right)$. As ratios we take

$$\frac{\eta_{xy}}{\eta_{xz}} = \frac{\Im\Sigma_{xy}\left(i\omega_n \to 0\right)}{\Im\Sigma_{xz}\left(i\omega_n \to 0\right)} \,. \tag{B.8}$$

Additionally, we employ the Padé method and the Beach method to perform the analytic continuations. In these cases we use as ratio

$$\frac{\eta_{xy}}{\eta_{xz}} = \frac{\Im\Sigma_{xy}\left(\omega = 0\right)}{\Im\Sigma_{xz}\left(\omega = 0\right)} \,. \tag{B.9}$$

All three methods provide similar ratios η_{xy}/η_{xz} (Tab. B.2). We point out that the ratios drop monotonously with increasing temperature, where for all studied temperatures $\eta_{xy} > \eta_{xz}$ is valid. For an even higher temperature ($\beta = 12.5\,\text{eV}^{-1}$) the ratio does not change considerably ($\eta_{xy}/\eta_{xz} = 1.6$, not shown here), which indicates that it is converging towards a high temperature limit. Especially at the lowest studied temperature, the extrapolation of the data to small frequencies becomes very sensitive to fine details (order of polynomial, number of Matsubara points, ...), and thus the ratios for $\beta = 200\,\text{eV}^{-1}$ can be only seen as rough estimates.

We use our DFT+DMFT estimates for η_{xy}/η_{xz} (Tab. B.2) to calculate R_H, again within the constant (orbital-dependent) scattering approximation (cf. discussion above).[42] Remarkably, the resulting temperature behavior of R_H, shown in Fig. B.3 with the blue stars and the cyan dots, even quantitatively resembles the experimental data [231, 232] (green triangles). Additionally, we show R_H calculated with the full frequency-dependent self-energy analytically continued with the Padé method (black down-pointing triangles) and with the Beach method (black up-pointing triangles) for

[42] Due to the small η at the lower temperatures ($\beta = 100\,\text{eV}^{-1}$ and $200\,\text{eV}^{-1}$), we cannot directly use η_{xy} and η_{xz}; an even denser **k**-mesh would be necessary. Instead, we use $\eta_{xz} = 0.05\,\text{eV}$ and adjust η_{xy} such that the estimated ratios are obtained.

Table B.2.: Estimation of the ratios η_{xy}/η_{xz} from the imaginary part of the self-energy at $\omega = 0$, i.e. $\omega_n \to 0$, with different methods: (i) Fit of the DFT+DMFT Matsubara self-energy with a 4^{th} order polynomial using the lowest 5 Matsubara points. The ratio is then given by Eq. B.8. (ii) Analytic continuation of the Matsubara self-energy with the Padé method (lowest 31 Matsubara points) using Eq. B.9 as definition of the ratio. (iii) Same as (ii), but with the Beach method for the analytic continuation. We note that the ratios for $\beta = 200\,\text{eV}^{-1}$ are very sensitive to details (order of polynomial, number of points used in Padé) and can thus be only understood as approximate values.

β (eV^{-1})	T (K)	Matsubara Fit	Padé AC	Beach AC
25	464	1.7	1.7	1.7
50	232	2.1	2.2	2.3
100	116	3.2	3.3	3.4
200	58	5.4	5.0	4.7

$\beta = 50\,\text{eV}^{-1}$ and $25\,\text{eV}^{-1}$. The resulting R_H agree well with the simple approximation of orbital-dependent constant scattering rates. This suggests that the frequency dependence of the self-energy has only a minor influence, whereas the ratio η_{xy}/η_{xz} is the pivotal factor determining R_H of Sr_2RuO_4.

With our analysis we cannot access R_H for temperatures below 40 K. On the level of the ratios, the rapid downturn would be accompanied by a decrease of η_{xy}/η_{xz}, which is not observed in our DFT+DMFT calculations. Below 25 K, Sr_2RuO_4 enters the Fermi-liquid regime [243, 244], which is connected to real-frequency self-energies at $\omega = 0$ of the form $\Im\Sigma_\alpha^{FL}(\omega = 0) = -A_\alpha T^2$ with the orbital-dependent constants A_α ($\alpha \in \{xy, xz, yz\}$). The ratio η_{xy}/η_{xz} is temperature independent in this regime, and subsequently our picture would also predict a temperature-independent R_H. This is not consistent with the experimentally observed downturn.

It was pointed out that at sufficiently low temperatures the scattering becomes dominated by elastic impurity and defect scattering [244]. In this limit, it is often assumed that the mean free path l is isotropic and depends only on the separation of the impurities (isotropic const.-l approximation). Then, it can be shown that the value of R_H is purely a consequence of the Fermi-surface topography in quasi-two-dimensional

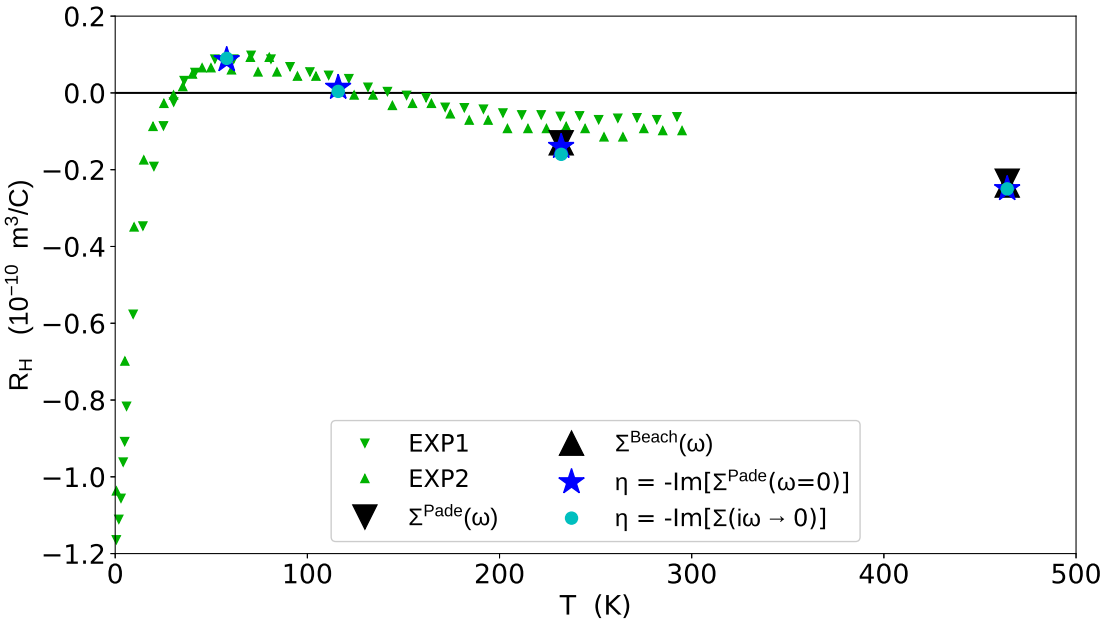

Figure B.3.: Temperature dependence of the Hall number R_H of Sr_2RuO_4. We show R_H calculated in the orbital-dependent const.-τ_s approximation using the ratios η_{xy}/η_{xz} from Tab. B.2 obtained with a fit on the Matsubara axis (cyan dots) and from the real-frequency Padé self-energies at $\omega = 0$ (blue stars). Additionally, we show R_H calculated with the full frequency-dependent Padé self-energy (black down-pointing triangles) and the full frequency-dependent Beach self-energy (black up-pointing triangles) for $\beta = 25\,\mathrm{eV}^{-1}$ (464 K) and $50\,\mathrm{eV}^{-1}$ (232 K). We compare our results to experimental data EXP1 from Ref. [231] (green down-pointing triangles) and EXP2 from Ref. [232] (green up-pointing triangles).

systems [231, 233, 245]. Within this approximation a low temperature value of $R_H = -0.9 \times 10^{-10}\,\mathrm{m}^3\,\mathrm{C}^{-1}$ was obtained [231] in good agreement with experiments. Additionally, already tiny amounts of Al impurities in Sr_2RuO_4 have a strong influence on R_H [233]. In the intermediate temperature range R_H loses the positive shoulder and only shows a monotonic increase with increasing temperature, without becoming positive anymore. The higher the amount of impurities, the stronger is this effect. For $T < 1\,\mathrm{K}$ and $T > 300\,\mathrm{K}$ the signs are unchanged (minus) and the precise values of R_H are little affected by the introduced impurities. Thus, it is argued in Ref. [233] that the low-temperature regime is strongly influenced by impurity scattering. Of course, this is not captured within our DFT+DMFT calculations.

However, with increasing temperature the electron-electron scattering becomes more and more important (initially with $\sim T^2$ in the Fermi-liquid regime), which might help explain the rapid increase of R_H for $T < 40\,\mathrm{K}$. Likely, the positive maximum of R_H is a result of the large orbital differentiation $\eta_{xy}/\eta_{xz} > 3$ in the Fermi-liquid regime. For temperatures above 40 K the scattering rates become slowly more orbital-independent with a high-temperature limit of $\eta_{xy}/\eta_{xz} \approx 1.5$. We are confident that the observed temperature behavior above 40 K is well captured by our DFT+DMFT calculations, where we were able to show that the sign of R_H depends on the ratio η_{xy}/η_{xz}.

List of Abbreviations

AFM	Antiferromagnetic
AIM	Anderson impurity model
ARPES	Angle-resolved photoemission spectroscopy
AMF	Around mean field
BZ	Brillouin zone
cLDA	Constrained local density approximation
cRPA	Constrained random phase approximation
CTHYB	Continuous-time (Monte Carlo) in hybridization expansion
CTINT	Continuous-time (Monte Carlo) in interaction expansion
CTQMC	Continuous-time quantum Monte Carlo
DC	Double counting
DFT	Density functional theory
DMFT	Dynamical mean-field theory
DMRG	Density matrix renormalization group
DOS	Density of states
ED	Exact diagonalization
FLL	Fully localized limit
FTPS	Fork tensor product states
GGA	Generalized gradient approximation
GS	Ground state
HFQMC	Hirsch-Fye quantum Monte Carlo
IPT	Iterative perturbation theory

LAPW+lo	Linearized augmented plane wave + local orbitals
LDA	Local density approximation
MEM	Maximum entropy method
MPS	Matrix product states
NCA	Non-crossing approximation
NRG	Numerical renormalization group
PAW	Projector augmented wave
PBE	Perdew-Burke-Ernzerhof functional
PM	Paramagnetic
TRIQS	Toolbox for Research on Interacting Quantum Systems
VCA	Virtual crystal approximation

List of Publications and Presentations

This page comprises peer-reviewed articles written during the time of this thesis. Additionally, oral talks and some selected poster presentations given at conferences, seminars and schools are listed below.

Peer-reviewed articles

- **M. Zingl**, M. Nuss, D. Bauernfeind, M. Aichhorn
  Physica B: Condensed Matter SCES issue, accepted (2017); arXiv:1707.08841
  "A real-frequency solver for the Anderson impurity model based on bath optimization and cluster perturbation theory"

- G. J. Kraberger, R. Triebl, **M. Zingl**, M. Aichhorn
  Phys. Rev. B, accepted (2017); arXiv:1705.08838
  "Maximum entropy formalism for the analytic continuation of matrix-valued Green's functions"

- D. Bauernfeind, **M. Zingl**, R. Triebl, M. Aichhorn, H. G. Evertz
  Phys. Rev. X 7, 031013 (2017); arXiv:1612.05587
  "Fork Tensor-Product States: Efficient Multiorbital Real-Time DMFT Solver"

- **M. Zingl**, E. Assmann, P. Seth, I. Krivenko, M. Aichhorn
  Phys. Rev. B 94, 045130 (2016); arXiv:1603.02115
  "Importance of effective dimensionality in manganese pnictides"

- M. Aichhorn, L. Pourovskii, P. Seth, V. Vildosola, **M. Zingl**, O. E. Peil, X. Deng, J. Mravlje, G. J. Kraberger, C. Martins, M. Ferrero, and O. Parcollet
  Comput. Phys. Comm. 204, 200 (2016); arXiv:1511.01302
  "TRIQS/DFTTools: A TRIQS application for ab initio calculations of correlated materials"

Oral presentations

- **M. Zingl**, S. Erker, M. Aichhorn
  DPG, Berlin, Germany, 19.03.2015
  "Electronic and magnetic properties of manganese pnictides"

- **M. Zingl**
  TU Graz Materials Day, Graz, Austria, 30.09.16
  "Ab-initio Description of Strongly-Correlated Materials:
  The Case of Manganese Pnictides"

- **M. Zingl**
  Physikalisches Oberseminar, Graz, Austria, 03.02.17
  "Ab-initio Description of Strongly-Correlated Materials:
  The Case of Manganese Pnictides"

- **M. Zingl**, E. Assmann, M. Aichhorn
  DPG, Dresden, Germany, 21.03.17
  "Importance of Mott physics in manganese pnictides:
  LaMnAsO and $BaMn_2As_2$"

- **M. Zingl**
  Seminar in theoretical physics, Fribourg, Switzerland, 10.04.17
  "Linear-response transport calculations for strongly-correlated materials within the framework of DFT+DMFT"

Poster presentations

- **M. Zingl**, E. Assmann, M. Aichhorn
  DPG, Regensburg, Germany, 10.03.16
  "Dimensional crossover in manganese based analogues of iron pnictides"

- **M. Zingl**, E. Assmann, P. Seth, I. Krivenko, M.Aichhorn
  International Summer School on Computational Quantum Materials, Sherbrooke, Canada, 30.05.16
  "Importance of effective dimensionality in manganese pnictides"

- **M. Zingl**, E. Assmann, P. Seth, I. Krivenko, M.Aichhorn
  VICOM Magnetism Winter School, Vienna, Austria, 20.02.17
  "Importance of effective dimensionality in manganese pnictides"

- **M. Zingl**, G. J. Kraberger M. Aichhorn
  SCES, Prague, Czech Republic, 20.07.17
  "Seebeck coefficient of the doped manganese pnictide LaMnAsO"

List of Figures

2.1. 2D Hubbard model. 10
2.2. Mapping to an effective impurity problem. 16
2.3. DMFT self-consistency cycle. 18
2.4. AIM in star geometry. 20
2.5. Graphical representation of an MPS and a FTPS. 24
2.6. Mott transition on the Bethe lattice. 31
2.7. DFT+DMFT sketch. 34

3.1. Derivative of the Fermi function at different temperatures. 46
3.2. Comparison of Wien2k *joint* and TRIQS/DFTTools transport code. . . 52

4.1. $SrVO_3$ crystal structure and crystal-field splitting. 54
4.2. DFT DOS of $SrVO_3$. 56
4.3. Correlated band structure of $SrVO_3$. 58
4.4. Optical conductivity of $SrVO_3$. 60
4.5. Comparison of impurity spectral functions (FTPS and CTHYB). 62
4.6. Comparison of the imaginary-time Green's functions $G(\tau)$. 63
4.7. Upper Hubbard band multiplet structure analysis. 65
4.8. Comparison of the correlated band structure (FTPS and CTHYB). . . 66

5.1. Crystal and magnetic structure of LaMnAsO and $BaMn_2As_2$. 71
5.2. PM and AFM spectral functions of LaMnAsO and $BaMn_2As_2$. 75
5.3. PM and AFM correlated band structure of LaMnAsO. 76
5.4. PM and AFM Mn-3*d* spectral functions of LaMnAsO and $BaMn_2As_2$. . 77
5.5. Real-space Hamiltonian of LaMnAsO and $BaMn_2As_2$. 79
5.6. Mn-3*d* maximally localized Wannier orbitals of $BaMn_2As_2$. 80
5.7. Magnetic moment versus temperature. 83

5.8. Optical conductivity components of $BaMn_2As_2$ and LaMnAsO. 85
5.9. LaMnAsO optical conductivity. 86
5.10. Comparison to LaMnAsO PES spectra from Ref. [208]. 88
5.11. Correlated band structure on Γ-M path of $BaMn_2As_2$. 89
5.12. Detail of the $BaMn_2As_2$ DFT band structure. 90

6.1. Comparison of VCA and super-cell DOS at 11% doping. 98
6.2. Spectral functions of LaMnAsO under electron doping. 100
6.3. AFM DFT band structure of 5 % electron-doped LaMnAsO. 102
6.4. Correlated band structure of 5 % electron-doped LaMnAsO. 103
6.5. Sketch of two scenarios promoting a high Seebeck coefficient. 106
6.6. Seebeck coefficient of electron-doped LaMnAsO. 108

A.1. $BaMn_2As_2$ DFT band structure. 115
A.2. LaMnAsO DFT band structure. 116
A.3. Conventional unit cell and BZ path. 116

B.1. Sr_2RuO_4 DFT band structure and Fermi surface. 118
B.2. Hall number of Sr_2RuO_4 for orbital-dependent constant scatterings. . . 123
B.3. Temperature dependence of Hall number of Sr_2RuO_4. 126

List of Tables

4.1. $SrVO_3$ atomic states (without spin-flip and pair-hopping terms.) 64

6.1. Seebeck coefficient of LaMnAsO at 5% electron doping. 111

B.1. Influence of velocity off-diagonal elements on σ and S. 122
B.2. Estimation of the ratio η_{xy}/η_{xz}. 125

Bibliography

[1] P. W. Anderson. More Is Different. *Science* 177, 393 (1972).

[2] W. Kohn. Nobel Lecture: Electronic structure of matter - wave functions and density functionals. *Rev. Mod. Phys.* 71, 1253 (1999).

[3] U. von Barth. Basic Density Functional Theory an Overview. *Phys. Scripta* 2004, 9 (2004).

[4] R. O. Jones and O. Gunnarsson. The density functional formalism, its applications and prospects. *Rev. Mod. Phys.* 61, 689 (1989).

[5] P. A. Lee, N. Nagaosa, and X.-G. Wen. Doping a Mott insulator: Physics of high-temperature superconductivity. *Rev. Mod. Phys.* 78, 17 (2006).

[6] T. V. Ramakrishnan, H. R. Krishnamurthy, S. R. Hassan, and G. V. Pai. Theory of Insulator Metal Transition and Colossal Magnetoresistance in Doped Manganites. *Phys. Rev. Lett.* 92, 157203 (2004).

[7] M. R. Peterson, B. S. Shastry, and J. O. Haerter. Thermoelectric effects in a strongly correlated model for Na_xCoO_2. *Phys. Rev. B* 76, 165118 (2007).

[8] J. Hubbard. Electron Correlations in Narrow Energy Bands. *Proc. Roy. Soc. A* 276, 238 (1963).

[9] M. J. Rozenberg, G. Kotliar, and X. Y. Zhang. Mott-Hubbard transition in infinite dimensions. II. *Phys. Rev. B* 49, 10181 (1994).

[10] J. E. Hirsch and S. Tang. Antiferromagnetism in the Two-Dimensional Hubbard Model. *Phys. Rev. Lett.* 62, 591 (1989).

[11] T. Yanagisawa. Physics of the Hubbard model and high temperature superconductivity. *J. Phys. Conf. Ser.* 108, 012010 (2008).

[12] W. Metzner and D. Vollhardt. Correlated Lattice Fermions in d=∞ Dimensions. *Phys. Rev. Lett.* 62, 324 (1989).

[13] A. Georges and G. Kotliar. Hubbard model in infinite dimensions. *Phys. Rev. B* 45, 6479 (1992).

[14] A. Georges. Strongly Correlated Electron Materials: Dynamical Mean Field Theory and Electronic Structure. *AIP Conf. Proc.* 715, 3 (2004).

[15] A. Georges, G. Kotliar, W. Krauth, and M. J. Rozenberg. Dynamical mean-field theory of strongly correlated fermion systems and the limit of infinite dimensions. *Rev. Mod. Phys.* 68, 13 (1996).

[16] G. Kotliar and D. Vollhardt. Strongly correlated materials: Insights from dynamical mean-field theory. *Physics Today* 57, 53 (2004).

[17] M. Imada, A. Fujimori, and Y. Tokura. Metal-insulator transitions. *Rev. Mod. Phys.* 70, 1039 (1998).

[18] V. I. Anisimov, A. I. Poteryaev, M. A. Korotin, A. O. Anokhin, and G. Kotliar. First-principles calculations of the electronic structure and spectra of strongly correlated systems: dynamical mean-field theory. *J. Phys.: Condens. Matter* 9, 7359 (1997).

[19] G. Kotliar, S. Y. Savrasov, K. Haule, V. S. Oudovenko, O. Parcollet, and C. A. Marianetti. Electronic structure calculations with dynamical mean-field theory. *Rev. Mod. Phys.* 78, 865 (2006).

[20] T. Miyake, K. Nakamura, R. Arita, and M. Imada. Comparison of Ab initio Low-Energy Models for LaFePO, LaFeAsO, $BaFe_2As_2$, LiFeAs, FeSe, and FeTe: Electron Correlation and Covalency. *J. Phys. Soc. Jpn.* 79, 044705 (2010).

[21] D. E. McNally, S. Zellman, Z. P. Yin, K. W. Post, H. He, K. Hao, G. Kotliar, D. Basov, C. C. Homes, and M. C. Aronson. From Hund's insulator to Fermi liquid: Optical spectroscopy study of K doping in $BaMn_2As_2$. *Phys. Rev. B* 92, 115142 (2015).

[22] D. E. McNally, J. W. Simonson, K. W. Post, Z. P. Yin, M. Pezzoli, G. J. Smith, V. Leyva, C. Marques, L. DeBeer-Schmitt, A. I. Kolesnikov, Y. Zhao, J. W. Lynn, D. N. Basov, G. Kotliar, and M. C. Aronson. Origin of the charge gap in LaMnPO. *Phys. Rev. B* 90, 180403 (2014).

[23] Y. X. Yao, J. Schmalian, C. Z. Wang, K. M. Ho, and G. Kotliar. Comparative study of the electronic and magnetic properties of $BaFe_2As_2$ and $BaMn_2As_2$ using the Gutzwiller approximation. *Phys. Rev. B* 84, 245112 (2011).

[24] A. Beleanu, J. Kiss, G. Kreiner, C. Köhler, L. Müchler, W. Schnelle, U. Burkhardt, S. Chadov, S. Medvediev, D. Ebke, C. Felser, G. Cordier, B. Albert, A. Hoser, F. Bernardi, T. I. Larkin, D. Pröpper, A. V. Boris, and B. Keimer. Large resistivity change and phase transition in the antiferromagnetic semiconductors LiMnAs and LaOMnAs. *Phys. Rev. B* 88, 184429 (2013).

[25] K. Kayanuma, H. Hiramatsu, T. Kamiya, M. Hirano, and H. Hosono. Epitaxial film growth and optoelectrical properties of layered semiconductors, LaMnXO (X=P, As, and Sb). *J. Appl. Phys.* 105. (2009).

[26] A. Antal, T. Knoblauch, Y. Singh, P. Gegenwart, D. Wu, and M. Dressel. Optical properties of the iron-pnictide analog $BaMn_2As_2$. *Phys. Rev. B* 86, 014506 (2012).

[27] J. An, A. S. Sefat, D. J. Singh, and M.-H. Du. Electronic structure and magnetism in $BaMn_2As_2$ and $BaMn_2Sb_2$. *Phys. Rev. B* 79, 075120 (2009).

[28] A. T. Satya, A. Mani, A. Arulraj, N. V. C. Shekar, K. Vinod, C. S. Sundar, and A. Bharathi. Pressure-induced metallization of $BaMn_2As_2$. *Phys. Rev. B* 84, 180515 (2011).

[29] J.-K. Bao, H. Jiang, Y.-L. Sun, W.-H. Jiao, C.-Y. Shen, H.-J. Guo, Y. Chen, C.-M. Feng, H.-Q. Yuan, Z.-A. Xu, G.-H. Cao, R. Sasaki, T. Tanaka, K. Matsubayashi, and Y. Uwatoko. Weakly ferromagnetic metallic state in heavily doped $Ba_{1-x}K_xMn_2As_2$. *Phys. Rev. B* 85, 144523 (2012).

[30] S. Yeninas, A. Pandey, V. Ogloblichev, K. Mikhalev, D. C. Johnston, and Y. Furukawa. Metal-insulator transition in antiferromagnetic $Ba_{1-x}K_xMn_2As_2$ ($0 \leqslant x \leqslant 0.4$) single crystals studied by ^{55}Mn and ^{75}As NMR. *Phys. Rev. B* 88, 241111 (2013).

[31] N. Emery, E. J. Wildman, J. M. S. Skakle, A. C. Mclaughlin, R. I. Smith, and A. N. Fitch. Variable temperature study of the crystal and magnetic structures of the giant magnetoresistant materials LMnAsO(L = La, Nd). *Phys. Rev. B* 83, 144429 (2011).

[32] Y. Singh, M. A. Green, Q. Huang, A. Kreyssig, R. J. McQueeney, D. C. Johnston, and A. I. Goldman. Magnetic order in $BaMn_2As_2$ from neutron diffraction measurements. *Phys. Rev. B* 80, 100403 (2009).

[33] S. Dong, W. Li, X. Huang, and E. Dagotto. First principles study of the magnetic properties of LaOMnAs. *J. Appl. Phys.* 115, 17D723 (2014).

[34] G. Xu, W. Ming, Y. Yao, X. Dai, S.-C. Zhang, and Z. Fang. Doping-dependent phase diagram of LaOMAs (M=V-Cu) and electron-type superconductivity near ferromagnetic instability. *EPL* 82, 67002 (2008).

[35] M. A. McGuire and V. O. Garlea. Short- and long-range magnetic order in LaMnAsO. *Phys. Rev. B* 93, 054404 (2016).

[36] D. C. Johnston, R. J. McQueeney, B. Lake, A. Honecker, M. E. Zhitomirsky, R. Nath, Y. Furukawa, V. P. Antropov, and Y. Singh. Magnetic exchange interactions in $BaMn_2As_2$: A case study of the J_1-J_2-J_c Heisenberg model. *Phys. Rev. B* 84, 094445 (2011).

[37] H. F. Wang, K. F. Cai, H. Li, L. Wang, and C. W. Zhou. Synthesis and thermoelectric properties of $BaMn_2Sb_2$ single crystals. *J. Alloy. Comp.* 477, 519 (2009).

[38] H. F. Wang, K. F. Cai, and S. Chen. Preparation and thermoelectric properties of $BaMn_{2-x}Zn_xSb_2$ zintl compounds. *J. Mater. Sci. Mater. Electron.* 23, 2289 (2012).

[39] K. Wang and C. Petrovic. Large thermopower in the antiferromagnetic semiconductor $BaMn_2Bi_2$. *Appl. Phys. Lett.* 103, 192104 (2013).

[40] H. Yanagi, T. Watanabe, K. Kodama, S. Iikubo, S. Shamoto, T. Kamiya, M. Hirano, and H. Hosono. Antiferromagnetic bipolar semiconductor LaMnPO with ZrCuSiAs-type structure. *J. Appl. Phys.* 105, 093916 (2009).

[41] Y.-L. Sun, J.-K. Bao, Y.-K. Luo, C.-M. Feng, Z.-A. Xu, and G.-H. Cao. Insulator-to-metal transition and large thermoelectric effect in $La_{1-x}Sr_xMnAsO$. *EPL* 98, 17009 (2012).

[42] Y. Shiomi, S. Ishiwata, Y. Taguchi, and Y. Tokura. Mott insulator to metal transition in filling-controlled $SmMnAsO_{1-x}$. *Phys. Rev. B* 84, 054519 (2011).

[43] G. Ryu. Study on exploration for superconducting transition metal compounds with low-dimensionality. PhD thesis (Tokyo Institute of Technology, Japan, 2012).

[44] M. H. Elsheikh, D. A. Shnawah, M. F. Sabri, S. B. Said, M. H. Hassan, M. B. Bashir, and M. Mohamad. A review on thermoelectric renewable energy: Principle parameters that affect their performance. *Renew. Sustainable Energy Rev.* 30, 337 (2014).

[45] G. J. Snyder and E. S. Toberer. Complex thermoelectric materials. *Nat. Mater.* 7, 105 (2008).

[46] W. Liu, Q. Jie, H. S. Kim, and Z. Ren. Current progress and future challenges in thermoelectric power generation: From materials to devices. *Acta Mater.* 87, 357 (2015).

[47] M. Zingl. Real-frequency impurity solver for dynamical mean-field theory based on cluster perturbation theory. MA thesis (Graz University of Technology, Austria, 2014).

[48] N. W. Ashcroft and N. D. Mermin. *Solid State Physics* (Saunders College, Philadelphia, 1976).

[49] P. Hohenberg and W. Kohn. Inhomogeneous Electron Gas. *Phys. Rev.* 136, B864 (1964).

[50] W. Kohn and L. J. Sham. Self-Consistent Equations Including Exchange and Correlation Effects. *Phys. Rev.* 140, A1133 (1965).

[51] D. M. Ceperley and B. J. Alder. Ground State of the Electron Gas by a Stochastic Method. *Phys. Rev. Lett.* 45, 566 (1980).

[52] J. P. Perdew, K. Burke, and M. Ernzerhof. Generalized Gradient Approximation Made Simple [Phys. Rev. Lett. 77, 3865 (1996)]. *Phys. Rev. Lett.* 78, 1396 (1997).

[53] Z. Szabó and Z. Gulácsi. Superconductivity in the extended Hubbard model with more than nearest-neighbour contributions. *Philos. Mag. B* 76, 911 (1997).

[54] J. E. Han, M. Jarrell, and D. L. Cox. Multiorbital Hubbard model in infinite dimensions: Quantum Monte Carlo calculation. *Phys. Rev. B* 58, 4199 (1998).

[55] J. C. Slater. *Quantum theory of atomic structure. 1* (McGraw-Hill, New York, 1960).

[56] V. I. Anisimov, F. Aryasetiawan, and A. I. Lichtenstein. First-principles calculations of the electronic structure and spectra of strongly correlated systems: the LDA + U method. *J. Phys.: Condens. Matter* 9, 767 (1997).

[57] V. I. Anisimov, I. V. Solovyev, M. A. Korotin, M. T. Czyżyk, and G. A. Sawatzky. Density-functional theory and NiO photoemission spectra. *Phys. Rev. B* 48, 16929 (1993).

[58] L. Vaugier, H. Jiang, and S. Biermann. Hubbard U and Hund exchange J in transition metal oxides: Screening versus localization trends from constrained random phase approximation. *Phys. Rev. B* 86, 165105 (2012).

[59] O. Gunnarsson, O. K. Andersen, O. Jepsen, and J. Zaanen. Density-functional calculation of the parameters in the Anderson model: Application to Mn in CdTe. *Phys. Rev. B* 39, 1708 (1989).

[60] F. Aryasetiawan, M. Imada, A. Georges, G. Kotliar, S. Biermann, and A. I. Lichtenstein. Frequency-dependent local interactions and low-energy effective models from electronic structure calculations. *Phys. Rev. B* 70, 195104 (2004).

[61] J. Kanamori. Electron Correlation and Ferromagnetism of Transition Metals. *Prog. of Theor. Phys.* 30, 275 (1963).

[62] A. Georges, L. de'Medici, and J. Mravlje. Strong Correlations from Hund's Coupling. *Annu. Rev. Condens. Matter Phys.* 4, 137 (2013).

[63] E. H. Lieb and F. Y. Wu. Absence of Mott Transition in an Exact Solution of the Short-Range, One-Band Model in One Dimension. *Phys. Rev. Lett.* 20, 1445 (1968).

[64] R. Bulla. Dynamical Mean-Field Theory: From Quantum Impurity Physics to Lattice Problems. *Phil. Mag.* 86, 1877 (2006).

[65] A. L. Fetter and J. D. Walecka. *Quantum Theory of Many-Particle Systems* (McGraw-Hill, Boston, 1971).

[66] H. Bruus and K. Flensberg. *Many-Body Quantum Theory in Condensed Matter Physics* (Oxford University Press, Oxford, 2004).

[67] P. W. Anderson. Localized Magnetic States in Metals. *Phys. Rev.* 124, 41 (1961).

[68] M. Caffarel and W. Krauth. Exact diagonalization approach to correlated fermions in infinite dimensions: Mott transition and superconductivity. *Phys. Rev. Lett.* 72, 1545 (1994).

[69] M. Capone, L. de'Medici, and A. Georges. Solving the dynamical mean-field theory at very low temperatures using the Lanczos exact diagonalization. *Phys. Rev. B* 76, 245116 (2007).

[70] K. G. Wilson. The renormalization group: Critical phenomena and the Kondo problem. *Rev. Mod. Phys.* 47, 773 (1975).

[71] S. R. White. Density matrix formulation for quantum renormalization groups. *Phys. Rev. Lett.* 69, 2863 (1992).

[72] H. Kajueter and G. Kotliar. New Iterative Perturbation Scheme for Lattice Models with Arbitrary Filling. *Phys. Rev. Lett.* 77, 131 (1996).

[73] H. Keiter and J. C. Kimball. Perturbation Technique for the Anderson Hamiltonian. *Phys. Rev. Lett.* 25, 672 (1970).

[74] J. E. Hirsch and R. M. Fye. Monte Carlo Method for Magnetic Impurities in Metals. *Phys. Rev. Lett.* 56, 2521 (1986).

[75] P. Werner, A. Comanac, L. de'Medici, M. Troyer, and A. J. Millis. Continuous-Time Solver for Quantum Impurity Models. *Phys. Rev. Lett.* 97, 076405 (2006).

[76] A. Liebsch and H. Ishida. Temperature and bath size in exact diagonalization dynamical mean field theory. *J. Phys.: Condens. Matter* 24, 053201 (2012).

[77] M. Schüler, C. Renk, and T. O. Wehling. Variational exact diagonalization method for Anderson impurity models. *Phys. Rev. B* 91, 235142 (2015).

[78] M. Granath and H. U. R. Strand. Distributional exact diagonalization formalism for quantum impurity models. *Phys. Rev. B* 86, 115111 (2012).

[79] C. Lin and A. A. Demkov. Efficient variational approach to the impurity problem and its application to the dynamical mean-field theory. *Phys. Rev. B* 88, 035123 (2013).

[80] Y. Lu, M. Höppner, O. Gunnarsson, and M. W. Haverkort. Efficient real-frequency solver for dynamical mean-field theory. *Phys. Rev. B* 90, 085102 (2014).

[81] C. Weber, A. Amaricci, M. Capone, and P. B. Littlewood. Augmented hybrid exact-diagonalization solver for dynamical mean field theory. *Phys. Rev. B* 86, 115136 (2012).

[82] M. Zingl, M. Nuss, D. Bauernfeind, and M. Aichhorn. A real-frequency solver for the Anderson impurity model based on bath optimization and cluster perturbation theory. *ArXiv e-prints.* arXiv:1707.08841 (2017).

[83] K. Yamada. Perturbation expansion for the Anderson Hamiltonian. II. *Prog. Theor. Phys.* 53, 970 (1975).

[84] N. Dasari, W. R. Mondal, P. Zhang, J. Moreno, M. Jarrell, and N. S. Vidhyadhiraja. A multi-orbital iterated perturbation theory for model Hamiltonians and real material-specific calculations of correlated systems. *Eur. Phys. J. B* 89, 202 (2016).

[85] E. Gull, A. J. Millis, A. I. Lichtenstein, A. N. Rubtsov, M. Troyer, and P. Werner. Continuous-time Monte Carlo methods for quantum impurity models. *Rev. Mod. Phys.* 83, 349 (2011).

[86] A. N. Rubtsov, V. V. Savkin, and A. I. Lichtenstein. Continuous-time quantum Monte Carlo method for fermions. *Phys. Rev. B* 72, 035122 (2005).

[87] P. Werner and A. J. Millis. Hybridization expansion impurity solver: General formulation and application to Kondo lattice and two-orbital models. *Phys. Rev. B* 74, 155107 (2006).

[88] P. Seth, I. Krivenko, M. Ferrero, and O. Parcollet. TRIQS/CTHYB: A continuous-time quantum Monte Carlo hybridisation expansion solver for quantum impurity problems. *Comput. Phys. Commun.* 200, 274 (2016).

[89] D. Bauernfeind, M. Zingl, R. Triebl, M. Aichhorn, and H. G. Evertz. Fork Tensor-Product States: Efficient Multiorbital Real-Time DMFT Solver. *Phys. Rev. X* 7, 031013 (2017).

[90] U. Schollwöck. The density-matrix renormalization group in the age of matrix product states. *Ann. Phys.* 326, 96 (2011).

[91] F. Verstraete and J. I. Cirac. Matrix product states represent ground states faithfully. *Phys. Rev. B* 73, 094423 (2006).

[92] M. Ganahl, M. Aichhorn, H. G. Evertz, P. Thunström, K. Held, and F. Verstraete. Efficient DMFT impurity solver using real-time dynamics with matrix product states. *Phys. Rev. B* 92, 155132 (2015).

[93] F. A. Wolf, I. P. McCulloch, O. Parcollet, and U. Schollwöck. Chebyshev matrix product state impurity solver for dynamical mean-field theory. *Phys. Rev. B* 90, 115124 (2014).

[94] G. J. Kraberger, R. Triebl, M. Zingl, and M. Aichhorn. Maximum entropy formalism for the analytic continuation of matrix-valued Green's functions. *ArXiv e-prints.* arXiv:1705.08838 (2017).

[95] K. S. D. Beach, R. J. Gooding, and F. Marsiglio. Reliable Padé analytical continuation method based on a high-accuracy symbolic computation algorithm. *Phys. Rev. B* 61, 5147 (2000).

[96] A. V. Ferris-Prabhu and D. H. Withers. Numerical analytic continuation using Padé approximants. *J. Comput. Phys.* 13, 94 (1973).

[97] R. N. Silver, D. S. Sivia, and J. E. Gubernatis. Maximum-entropy method for analytic continuation of quantum Monte Carlo data. *Phys. Rev. B* 41, 2380 (1990).

[98] J. E. Gubernatis, M. Jarrell, R. N. Silver, and D. S. Sivia. Quantum Monte Carlo simulations and maximum entropy: Dynamics from imaginary-time data. *Phys. Rev. B* 44, 6011 (1991).

[99] S. F. Gull and J. Skilling. Maximum entropy method in image processing. *Commun., Radar and Signal Proces., IEE Proc. F* 131, 646 (1984).

[100] A. W. Sandvik. Stochastic method for analytic continuation of quantum Monte Carlo data. *Phys. Rev. B* 57, 10287 (1998).

[101] K. S. Beach. Identifying the maximum entropy method as a special limit of stochastic analytic continuation. *ArXiv e-prints.* arXiv:cond-mat/0403055 (2004).

[102] A. S. Mishchenko, N. V. Prokof'ev, A. Sakamoto, and B. V. Svistunov. Diagrammatic quantum Monte Carlo study of the Fröhlich polaron. *Phys. Rev. B* 62, 6317 (2000).

[103] X. Wang, E. Gull, L. de'Medici, M. Capone, and A. J. Millis. Antiferromagnetism and the gap of a Mott insulator: Results from analytic continuation of the self-energy. *Phys. Rev. B* 80, 045101 (2009).

[104] V. I. Anisimov, D. E. Kondakov, A. V. Kozhevnikov, I. A. Nekrasov, Z. V. Pchelkina, J. W. Allen, S.-K. Mo, H.-D. Kim, P. Metcalf, S. Suga, A. Sekiyama, G. Keller, I. Leonov, X. Ren, and D. Vollhardt. Full orbital calculation scheme for materials with strongly correlated electrons. *Phys. Rev. B* 71. (2005).

[105] J. Mravlje and A. Georges. Thermopower and Entropy: Lessons from Sr_2RuO_4. *Phys. Rev. Lett.* 117, 036401 (2016).

[106] N. F. Mott. Metal-Insulator Transition. *Rev. Mod. Phys.* 40, 677 (1968).

[107] F. Gebhard. *The Mott Metal-Insulator Transition: Models and Methods* (Springer, Berlin and Heidelberg, 1997).

[108] E. N. Economou. *Green's Functions in Quantuum Physics* (Springer, Berlin and Heidelberg, 2006).

[109] J. Joo and V. Oudovenko. Quantum Monte Carlo calculation of the finite temperature Mott-Hubbard transition. *Phys. Rev. B* 64, 193102 (2001).

[110] R. Bulla, T. A. Costi, and D. Vollhardt. Finite-temperature numerical renormalization group study of the Mott transition. *Phys. Rev. B* 64, 045103 (2001).

[111] J. M. Luttinger. Analytic Properties of Single-Particle Propagators for Many-Fermion Systems. *Phys. Rev.* 121, 942 (1961).

[112] M. Aichhorn, L. Pourovskii, P. Seth, V. Vildosola, M. Zingl, O. E. Peil, X. Deng, J. Mravlje, G. J. Kraberger, C. Martins, M. Ferrero, and O. Parcollet. TRIQS/DFTTools: A TRIQS application for ab initio calculations of correlated materials. *Comput. Phys. Commun.* 204, 200 (2016).

[113] N. Marzari and D. Vanderbilt. Maximally localized generalized Wannier functions for composite energy bands. *Phys. Rev. B* 56, 12847 (1997).

[114] I. Souza, N. Marzari, and D. Vanderbilt. Maximally localized Wannier functions for entangled energy bands. *Phys. Rev. B* 65, 035109 (2001).

[115] F. Lechermann, A. Georges, A. Poteryaev, S. Biermann, M. Posternak, A. Yamasaki, and O. K. Andersen. Dynamical mean-field theory using Wannier functions: A flexible route to electronic structure calculations of strongly correlated materials. *Phys. Rev. B* 74, 125120 (2006).

[116] M. Aichhorn, L. Pourovskii, V. Vildosola, M. Ferrero, O. Parcollet, T. Miyake, A. Georges, and S. Biermann. Dynamical mean-field theory within an augmented plane-wave framework: Assessing electronic correlations in the iron pnictide LaFeAsO. *Phys. Rev. B* 80, 085101 (2009).

[117] P. Blaha, K. Schwarz, G. Madsen, D. Kvasnicka, and J. Luitz. *WIEN2k, An augmented Plane Wave + Local Orbitals Program for Calculating Crystal Properties* (Techn. Universitaet Wien, Austria, 2001).

[118] K. Schwarz and P. Blaha. Solid state calculations using WIEN2k. *Comput. Mater. Sci.* 28, 259 (2003).

[119] M. Aichhorn, L. Pourovskii, and A. Georges. Importance of electronic correlations for structural and magnetic properties of the iron pnictide superconductor LaFeAsO. *Phys. Rev. B* 84, 054529 (2011).

[120] A. I. Lichtenstein, M. I. Katsnelson, and G. Kotliar. Finite-Temperature Magnetism of Transition Metals: An *ab initio* Dynamical Mean-Field Theory. *Phys. Rev. Lett.* 87, 067205 (2001).

[121] J. Kuneš, V. I. Anisimov, A. V. Lukoyanov, and D. Vollhardt. Local correlations and hole doping in NiO: A dynamical mean-field study. *Phys. Rev. B* 75, 165115 (2007).

[122] K. Haule, T. Birol, and G. Kotliar. Covalency in transition-metal oxides within all-electron dynamical mean-field theory. *Phys. Rev. B* 90, 075136 (2014).

[123] K. Haule. Exact Double Counting in Combining the Dynamical Mean Field Theory and the Density Functional Theory. *Phys. Rev. Lett.* 115, 196403 (2015).

[124] V. I. Anisimov, J. Zaanen, and O. K. Andersen. Band theory and Mott insulators: Hubbard U instead of Stoner I. *Phys. Rev. B* 44, 943 (1991).

[125] M. T. Czyżyk and G. A. Sawatzky. Local-density functional and on-site correlations: The electronic structure of La_2CuO_4 and $LaCuO_3$. *Phys. Rev. B* 49, 14211 (1994).

[126] K. Held. Electronic structure calculations using dynamical mean field theory. *Adv. Phys.* 56, 829 (2007).

[127] O. Parcollet, M. Ferrero, T. Ayral, H. Hafermann, I. Krivenko, L. Messio, and P. Seth. TRIQS: A toolbox for research on interacting quantum systems. *Comput. Phys. Commun.* 196, 398 (2015).

[128] G. D. Mahan. *Many-Particle Physics* (Springer US, New York, 2000).

[129] J. M. Tomczak. Spectral and Optical Properties of Correlated Materials. PhD thesis (École Polytechnique, France, 2007).

[130] V. S. Oudovenko, G. Pálsson, K. Haule, G. Kotliar, and S. Y. Savrasov. Electronic structure calculations of strongly correlated electron systems by the dynamical mean-field method. *Phys. Rev. B* 73, 035120 (2006).

[131] E. Assmann, P. Wissgott, J. Kuneš, A. Toschi, P. Blaha, and K. Held. woptic: Optical conductivity with Wannier functions and adaptive k-mesh refinement. *Comput. Phys. Commun.* 202, 1 (2016).

[132] T. Seebeck. Magnetische Polarisation der Metalle und Erze durch Temperatur-Differenz. *Abhandlungen der Preussischen Akademie der Wissenschaften,* 265 (1823).

[133] A. F. Ioffe. *Semiconductor thermoelements and Thermoelectric cooling* (Infosearch Ltd., London, 1957).

[134] E. H. Hall. On a New Action of the Magnet on Electric Currents. *Am. J. Math.* 2, 287 (1879).

[135] J. M. Tomczak and S. Biermann. Optical properties of correlated materials: Generalized Peierls approach and its application to VO_2. *Phys. Rev. B* 80, 085117 (2009).

[136] R. Kubo. Statistical-Mechanical Theory of Irreversible Processes. I. General Theory and Simple Applications to Magnetic and Conduction Problems. *J. Phys. Soc. Jpn.* 12, 570 (1957).

[137] A. Khurana. Electrical conductivity in the infinite-dimensional Hubbard model. *Phys. Rev. Lett.* 64, 1990 (1990).

[138] V. Zlatic and B. Horvatic. The local approximation for correlated systems on high dimensional lattices. *Solid State Commun.* 75, 263 (1990).

[139] T. Pruschke, M. Jarrell, and J. K. Freericks. Anomalous normal-state properties of high-T_c superconductors: intrinsic properties of strongly correlated electron systems? *Adv. Phys.* 44, 187 (1995).

[140] R. P. Feynman. Forces in Molecules. *Phys. Rev.* 56, 340 (1939).

[141] G. K. Madsen and D. J. Singh. BoltzTraP. A code for calculating band-structure dependent quantities. *Comput. Phys. Commun.* 175, 67 (2006).

[142] P. B. Allen. Boltzmann Theory and Resistivity of Metals. In: *Quantum Theory of Real Materials*. p. 219 (Kluwer, Bosten, 1996).

[143] G. D. Mahan and J. O. Sofo. The best thermoelectric. *Proc. Natl. Acad. Sci.* 93, 7436 (1996).

[144] T. J. Scheidemantel, C. Ambrosch-Draxl, T. Thonhauser, J. V. Badding, and J. O. Sofo. Transport coefficients from first-principles calculations. *Phys. Rev. B* 68, 125210 (2003).

[145] K. Held, R. Arita, V. I. Anisimov, and K. Kuroki. The LDA+DMFT Route to Identify Good Thermoelectrics. In: *Properties and Applications of Thermoelectric Materials: The Search for New Materials for Thermoelectric Devices*. p. 141 (Springer Netherlands, Dordrecht, 2009).

[146] C. Ambrosch-Draxl and J. O. Sofo. Linear optical properties of solids within the full-potential linearized augmented planewave method. *Comput. Phys. Commun.* 175, 1 (2006).

[147] G. Kresse and J. Hafner. Ab initio molecular dynamics for liquid metals. *Phys. Rev. B* 47, 558 (1993).

[148] G. Kresse and J. Hafner. Ab initio molecular-dynamics simulation of the liquid-metal-amorphous-semiconductor transition in germanium. *Phys. Rev. B* 49, 14251 (1994).

[149] G. Kresse and J. Furthmüller. Efficiency of ab-initio total energy calculations for metals and semiconductors using a plane-wave basis set. *Comput. Mater. Sci.* 6, 15 (1996).

[150] G. Kresse and J. Furthmüller. Efficient iterative schemes for ab initio total-energy calculations using a plane-wave basis set. *Phys. Rev. B* 54, 11169 (1996).

[151] A. A. Mostofi, J. R. Yates, Y.-S. Lee, I. Souza, D. Vanderbilt, and N. Marzari. wannier90: A tool for obtaining maximally-localised Wannier functions. *Comput. Phys. Commun.* 178, 685 (2008).

[152] M. J. Rey, P. Dehaudt, J. C. Joubert, B. Lambert-Andron, M. Cyrot, and F. Cyrot-Lackmann. Preparation and structure of the compounds $SrVO_3$ and Sr_2VO_4. *J. Solid State Chem.* 86, 101 (1990).

[153] Y. Tokura and N. Nagaosa. Orbital Physics in Transition-Metal Oxides. *Science* 288, 462 (2000).

[154] K. Momma and F. Izumi. *VESTA3* for three-dimensional visualization of crystal, volumetric and morphology data. *J. Appl. Crystallogr.* 44, 1272 (2011).

[155] I. A. Nekrasov, K. Held, G. Keller, D. E. Kondakov, T. Pruschke, M. Kollar, O. K. Andersen, V. I. Anisimov, and D. Vollhardt. Momentum-resolved spectral functions of $SrVO_3$ calculated by LDA + DMFT. *Phys. Rev. B* 73, 155112 (2006).

[156] C. Taranto, M. Kaltak, N. Parragh, G. Sangiovanni, G. Kresse, A. Toschi, and K. Held. Comparing quasiparticle GW+DMFT and LDA+DMFT for the test bed material $SrVO_3$. *Phys. Rev. B* 88, 165119 (2013).

[157] R. Sakuma, P. Werner, and F. Aryasetiawan. Electronic structure of $SrVO_3$ within GW+DMFT. *Phys. Rev. B* 88, 235110 (2013).

[158] P. Wissgott, J. Kuneš, A. Toschi, and K. Held. Dipole matrix element approach versus Peierls approximation for optical conductivity. *Phys. Rev. B* 85, 205133 (2012).

[159] T. Yoshida, K. Tanaka, H. Yagi, A. Ino, H. Eisaki, A. Fujimori, and Z.-X. Shen. Direct Observation of the Mass Renormalization in $SrVO_3$ by Angle Resolved Photoemission Spectroscopy. *Phys. Rev. Lett.* 95, 146404 (2005).

[160] L. Boehnke, F. Nilsson, F. Aryasetiawan, and P. Werner. When strong correlations become weak: Consistent merging of GW and DMFT. *Phys. Rev. B* 94, 201106 (2016).

[161] J. M. Tomczak, M. Casula, T. Miyake, and S. Biermann. Asymmetry in band widening and quasiparticle lifetimes in $SrVO_3$: Competition between screened exchange and local correlations from combined *GW* and dynamical mean-field theory *GW* + DMFT. *Phys. Rev. B* 90, 165138 (2014).

[162] Y. C. Lan, X. L. Chen, and M. He. Structure, magnetic susceptibility and resistivity properties of $SrVO_3$. *J. Alloy. Comp.* 354, 95 (2003).

[163] H. Makino, I. H. Inoue, M. J. Rozenberg, I. Hase, Y. Aiura, and S. Onari. Bandwidth control in a perovskite-type $3d^1$-correlated metal $Ca_{1-x}Sr_xVO_3$. II. Optical spectroscopy. *Phys. Rev. B* 58, 4384 (1998).

[164] I. H. Inoue, O. Goto, H. Makino, N. E. Hussey, and M. Ishikawa. Bandwidth control in a perovskite-type $3d^1$-correlated metal $Ca_{1-x}Sr_xVO_3$. I. Evolution of the electronic properties and effective mass. *Phys. Rev. B* 58, 4372 (1998).

[165] P. Dougier, J. C. Fan, and J. B. Goodenough. Etude des proprietes magnetiques, electriques et optiques des phases de structure perovskite $SrVO_{2.90}$ et $SrVO_3$. *J. Solid State Chem.* 14, 247 (1975).

[166] D. Bergeron and A.-M. S. Tremblay. Algorithms for optimized maximum entropy and diagnostic tools for analytic continuation. *Phys. Rev. E* 94, 023303 (2016).

[167] A. Liebsch. Surface versus Bulk Coulomb Correlations in Photoemission Spectra of $SrVO_3$ and $CaVO_3$. *Phys. Rev. Lett.* 90, 096401 (2003).

[168] A. Sekiyama, H. Fujiwara, S. Imada, S. Suga, H. Eisaki, S. I. Uchida, K. Takegahara, H. Harima, Y. Saitoh, I. A. Nekrasov, G. Keller, D. E. Kondakov, A. V. Kozhevnikov, T. Pruschke, K. Held, D. Vollhardt, and V. I. Anisimov. Mutual Experimental and Theoretical Validation of Bulk Photoemission Spectra of $Sr_{1-x}Ca_xVO_3$. *Phys. Rev. Lett.* 93, 156402 (2004).

[169] A. Gössling, R. Schmitz, H. Roth, M. W. Haverkort, T. Lorenz, J. A. Mydosh, E. Müller-Hartmann, and M. Grüninger. Mott-Hubbard exciton in the optical conductivity of $YTiO_3$ and $SmTiO_3$. *Phys. Rev. B* 78, 075122 (2008).

[170] T. Arima and Y. Tokura. Optical Study of Electronic Structure in Perovskite-Type RMO3 (R=La, Y; M=Sc, Ti, V, Cr, Mn, Fe, Co, Ni, Cu). *J. Phys. Soc. Jpn.* 64, 2488 (1995).

[171] E. V. Benckiser. Optical Spectroscopy of Orbital and Magnetic Excitations in Vanadates and Cuprates. PhD thesis (Universitaet zu Köln, Germany, 2007).

[172] A. Gössling, M. W. Haverkort, M. Benomar, H. Wu, D. Senff, T. Möller, M. Braden, J. A. Mydosh, and M. Grüninger. Mott-Hubbard versus charge-transfer behavior in $LaSrMnO_4$ studied via optical conductivity. *Phys. Rev. B* 77, 035109 (2008).

[173] J. Reul, L. Fels, N. Qureshi, K. Shportko, M. Braden, and M. Grüninger. Temperature-dependent optical conductivity of layered $LaSrFeO_4$. *Phys. Rev. B* 87, 205142 (2013).

[174] M. Zingl, E. Assmann, P. Seth, I. Krivenko, and M. Aichhorn. Importance of effective dimensionality in manganese pnictides. *Phys. Rev. B* 94, 045130 (2016).

[175] S. Erker. Correlated Electronic Structure of Manganese Pnictides. MA thesis (Graz University of Technology, Austria, 2014).

[176] Y. Kamihara, T. Watanabe, M. Hirano, and H. Hosono. Iron-Based Layered Superconductor $La[O_{1-x}F_x]FeAs$ (x = 0.05-0.12) with T_c = 26 K. *J. Am. Chem. Soc.* 130, 3296 (2008).

[177] K. Haule, J. H. Shim, and G. Kotliar. Correlated Electronic Structure of $LaO_{1-x}F_xFeAs$. *Phys. Rev. Lett.* 100, 226402 (2008).

[178] K. Haule and G. Kotliar. Coherence–incoherence crossover in the normal state of iron oxypnictides and importance of Hund's rule coupling. *New J. Phys.* 11, 025021 (2009).

[179] L. de'Medici, J. Mravlje, and A. Georges. Janus-Faced Influence of Hund's Rule Coupling in Strongly Correlated Materials. *Phys. Rev. Lett.* 107, 256401 (2011).

[180] H. Ishida and A. Liebsch. Fermi-liquid, non-Fermi-liquid, and Mott phases in iron pnictides and cuprates. *Phys. Rev. B* 81, 054513 (2010).

[181] L. de'Medici, G. Giovannetti, and M. Capone. Selective Mott Physics as a Key to Iron Superconductors. *Phys. Rev. Lett.* 112, 177001 (2014).

[182] A. Pandey, V. K. Anand, and D. C. Johnston. Large miscibility gap in the $Ba(Mn_xFe_{1-x})_2As_2$ system. *Phys. Rev. B* 84, 014405 (2011).

[183] A. Pandey, R. S. Dhaka, J. Lamsal, Y. Lee, V. K. Anand, A. Kreyssig, T. W. Heitmann, R. J. McQueeney, A. I. Goldman, B. N. Harmon, A. Kaminski, and D. C. Johnston. $Ba_{1-x}K_xMn_2As_2$: An Antiferromagnetic Local-Moment Metal. *Phys. Rev. Lett.* 108, 087005 (2012).

[184] J. Lamsal, G. S. Tucker, T. W. Heitmann, A. Kreyssig, A. Jesche, A. Pandey, W. Tian, R. J. McQueeney, D. C. Johnston, and A. I. Goldman. Persistence of local-moment antiferromagnetic order in $Ba_{1-x}K_xMn_2As_2$. *Phys. Rev. B* 87, 144418 (2013).

[185] A. Pandey and D. C. Johnston. $Ba_{0.4}Rb_{0.6}Mn_2As_2$: A prototype half-metallic ferromagnet. *Phys. Rev. B* 92, 174401 (2015).

[186] T. Hanna, S. Matsuishi, K. Kodama, T. Otomo, S. Shamoto, and H. Hosono. From antiferromagnetic insulator to ferromagnetic metal: Effects of hydrogen substitution in LaMnAsO. *Phys. Rev. B* 87, 020401 (2013).

[187] N. Emery, E. J. Wildman, J. M. S. Skakle, G. Giriat, R. I. Smith, and A. C. Mclaughlin. Giant magnetoresistance in oxypnictides (La,Nd)OMnAs. *Chem. Commun.* 46, 6777 (2010).

[188] D. D. Dung, W. Feng, and S. Cho. Growth and transport studies of $BaMn_2As_2$ thin films. *J. Vac. Sci. Technol. B* 29. (2011).

[189] Y. Singh, A. Ellern, and D. C. Johnston. Magnetic, transport, and thermal properties of single crystals of the layered arsenide $BaMn_2As_2$. *Phys. Rev. B* 79, 094519 (2009).

[190] J. Mravlje, M. Aichhorn, and A. Georges. Origin of the High Néel Temperature in $SrTcO_3$. *Phys. Rev. Lett.* 108, 197202 (2012).

[191] S. L. Brock, J. E. Greedan, and S. M. Kauzlarich. Resistivity and Magnetism of AMn_2P_2 (A = Sr, Ba): The Effect of Structure Type on Physical Properties. *J. Solid State Chem.* 113, 303 (1994).

[192] A. C. McLaughlin. Private Communication. The correct value of the measured manganese magnetic moment in LaMnAsO is $3.55\,\mu_B$/Mn at 2 K, as given in the Supplemental Material of Ref. [31]. (2016).

[193] O. K. Andersen and L. Boeri. On the multi-orbital band structure and itinerant magnetism of iron-based superconductors. *Ann. Phys.* 523, 8 (2011).

[194] S. Graser, A. F. Kemper, T. A. Maier, H.-P. Cheng, P. J. Hirschfeld, and D. J. Scalapino. Spin fluctuations and superconductivity in a three-dimensional tight-binding model for $BaFe_2As_2$. *Phys. Rev. B* 81, 214503 (2010).

[195] T. Ribic, E. Assmann, A. Tóth, and K. Held. Cubic interaction parameters for t_{2g} Wannier orbitals. *Phys. Rev. B* 90, 165105 (2014).

[196] S. L. Skornyakov, A. V. Efremov, N. A. Skorikov, M. A. Korotin, Y. A. Izyumov, V. I. Anisimov, A. V. Kozhevnikov, and D. Vollhardt. Classification of the electronic correlation strength in the iron pnictides: The case of the parent compound $BaFe_2As_2$. *Phys. Rev. B* 80, 092501 (2009).

[197] J. W. Simonson, Z. P. Yin, M. Pezzoli, J. Guo, J. Liu, K. Post, A. Efimenko, N. Hollmann, Z. Hu, H.-J. Lin, C.-T. Chen, C. Marques, V. Leyva, G. Smith, J. W. Lynn, L. L. Sun, G. Kotliar, D. N. Basov, L. H. Tjeng, and M. C. Aronson. From antiferromagnetic insulator to correlated metal in pressurized and doped LaMnPO. *Proc. Natl. Acad. Sci.* 109, E1815 (2012).

[198] J. Kuneš, R. Arita, P. Wissgott, A. Toschi, H. Ikeda, and K. Held. Wien2wannier: From linearized augmented plane waves to maximally localized Wannier functions. *Comput. Phys. Commun.* 181, 1888 (2010).

[199] P. Werner, M. Casula, T. Miyake, F. Aryasetiawan, A. J. Millis, and S. Biermann. Satellites and large doping and temperature dependence of electronic properties in hole-doped $BaFe_2As_2$. *Nat. Phys.* 8, 331 (2012).

[200] A. Horvat, L. Pourovskii, M. Aichhorn, and J. Mravlje. Theoretical prediction of antiferromagnetism in layered perovskite Sr_2TcO_4. *Phys. Rev. B* 95, 205115 (2017).

[201] A. A. Katanin, A. Toschi, and K. Held. Comparing pertinent effects of antiferromagnetic fluctuations in the two- and three-dimensional Hubbard model. *Phys. Rev. B* 80, 075104 (2009).

[202] G. Rohringer, A. Toschi, A. Katanin, and K. Held. Critical Properties of the Half-Filled Hubbard Model in Three Dimensions. *Phys. Rev. Lett.* 107, 256402 (2011).

[203] M. Karolak, M. Edelmann, and G. Sangiovanni. Nickel-titanium double perovskite: A three-dimensional spin-1 Heisenberg antiferromagnet. *Phys. Rev. B* 91, 075108 (2015).

[204] R. P. Singh and M. Singh. Effect of Interlayer Coupling on Néel Temperature in Antiferromagnets. *Phys. Status Solidi B* 169, 571 (1992).

[205] R. P. Singh, Z. C. Tao, and M. Singh. Role of antiferromagnetic interlayer coupling on magnetic properties of $YBa_2Cu_3O_{6+x}$. *Phys. Rev. B* 46, 1244 (1992).

[206] Ajay, S. Patra, and R. S. Tripathi. Effect of interlayer coupling on Néel, temperature in copper oxide based antiferromagnets. *Phys. Status Solidi B* 188, 787 (1995).

[207] W.-L. Zhang, P. Richard, A. van Roekeghem, S.-M. Nie, N. Xu, P. Zhang, H. Miao, S.-F. Wu, J.-X. Yin, B. B. Fu, L.-Y. Kong, T. Qian, Z.-J. Wang, Z. Fang, A. S. Sefat, S. Biermann, and H. Ding. Angle-resolved photoemission observation of Mn-pnictide hybridization and negligible band structure renormalization in $BaMn_2As_2$ and $BaMn_2Sb_2$. *Phys. Rev. B* 94, 155155 (2016).

[208] A. Higashiya, K. Nakagawa, A. Yamasaki, K. Nagai, S. Fujioka, Y. Kanai, K. Yamagami, H. Fujiwara, A. Sekiyama, A. Abozeed, T. Kadono, S. Imada, K. Kuga, M. Yabashi, K. Tamasaku, T. Ishikawa, S. Toyama, and K. Takase. Hole doping effect on the electronic structure of layered oxypnictide LaOMnAs. *J. Electron. Spectrosc. Relat. Phenom.* In Press, Corrected Proof. (2017).

[209] H. Chen, H. Park, A. J. Millis, and C. A. Marianetti. Charge transfer across transition-metal oxide interfaces: Emergent conductance and electronic structure. *Phys. Rev. B* 90, 245138 (2014).

[210] M. Karolak, G. Ulm, T. Wehling, V. Mazurenko, A. Poteryaev, and A. Lichtenstein. Double counting in LDA+DMFT - The example of NiO. *J. Electron. Spectrosc. Relat. Phenom.* 181, 11 (2010).

[211] E. Assmann. *Spaghetti-prima.py* [`http://eassmann.github.io/prima.py`]. Software Version 0.3.

[212] M. Edelmann, G. Sangiovanni, M. Capone, and L. de'Medici. Chromium analogs of iron-based superconductors. *Phys. Rev. B* 95, 205118 (2017).

[213] S. K. Mishra, S. Satpathy, and O. Jepsen. Electronic structure and thermoelectric properties of bismuth telluride and bismuth selenide. *J. Phys. Condens. Matter* 9, 461 (1997).

[214] L. Nordheim. Zur Elektronentheorie der Metalle. I. *Ann. Phys.* 401, 607 (1931).

[215] P. E. Blöchl. Projector augmented-wave method. *Phys. Rev. B* 50, 17953 (1994).

[216] G. Kresse and D. Joubert. From ultrasoft pseudopotentials to the projector augmented-wave method. *Phys. Rev. B* 59, 1758 (1999).

[217] H. J. Monkhorst and J. D. Pack. Special points for Brillouin-zone integrations. *Phys. Rev. B* 13, 5188 (1976).

[218] A. Naito, Y. Morosawa, T. Watanabe, Y. Takano, and K. Takase. Carrier Doping Effects on the Physical Properties of the Layered Antiferromagnetic Semiconductor (LaO)MnAs. *JPS Conf. Proc.* 1, 036401 (2014).

[219] J. P. Heremans, V. Jovovic, E. S. Toberer, A. Saramat, K. Kurosaki, A. Charoenphakdee, S. Yamanaka, and G. J. Snyder. Enhancement of Thermoelectric Efficiency in PbTe by Distortion of the Electronic Density of States. *Science* 321, 554 (2008).

[220] J. R. Sootsman, D. Y. Chung, and M. G. Kanatzidis. New and Old Concepts in Thermoelectric Materials. *Angew. Chem. Int. Ed.* 48, 8616 (2009).

[221] J. M. Tomczak, K. Haule, and G. Kotliar. Thermopower of the Correlated Narrow Gap Semiconductor FeSi and Comparison to RuSi. In: *New Materials for Thermoelectric Applications: Theory and Experiment*. p. 45 (Springer Netherlands, Dordrecht, 2013).

[222] K. Haule and G. Kotliar. Thermoelectrics Near the Mott Localization-Delocalization Transition. In: *Properties and Applications of Thermoelectric Materials: The Search for New Materials for Thermoelectric Devices*. p. 119 (Springer Netherlands, Dordrecht, 2009).

[223] K. Kuroki and R. Arita. "Pudding Mold" Band Drives Large Thermopower in Na_xCoO_2. *J. Phys. Soc. Jpn.* 76, 083707 (2007).

[224] R. Arita, K. Kuroki, K. Held, A. V. Lukoyanov, S. Skornyakov, and V. I. Anisimov. Origin of large thermopower in $LiRh_2O_4$: Calculation of the Seebeck coefficient by the combination of local density approximation and dynamical mean-field theory. *Phys. Rev. B* 78, 115121 (2008).

[225] K. Mori, H. Sakakibara, H. Usui, and K. Kuroki. Ideal band shape in the potential thermoelectric material $CuAlO_2$: Comparison to Na_xCoO_2. *Phys. Rev. B* 88, 075141 (2013).

[226] P. Wissgott, A. Toschi, H. Usui, K. Kuroki, and K. Held. Enhancement of the Na_xCoO_2 thermopower due to electronic correlations. *Phys. Rev. B* 82, 201106 (2010).

[227] P. Wissgott, A. Toschi, G. Sangiovanni, and K. Held. Effects of electronic correlations and disorder on the thermopower of Na_xCoO_2. *Phys. Rev. B* 84, 085129 (2011).

[228] D. J. Singh. Electronic structure and fermiology of superconducting $LaNiGa_2$. *Phys. Rev. B* 86, 174507 (2012).

[229] A. Kokalj. Computer graphics and graphical user interfaces as tools in simulations of matter at the atomic scale. *Comput. Mater. Sci.* 28, 155 (2003).

[230] N. Shirakawa, K. Murata, Y. Nishihara, S. Nishizaki, Y. Maeno, T. Fujita, J. G. Bednorz, F. Lichtenberg, and N. Hamada. Novel Hall-Coefficient Behavior in Superconducting Sr_2RuO_4. *J. Phys. Soc. Jpn.* 64, 1072 (1995).

[231] A. P. Mackenzie, N. E. Hussey, A. J. Diver, S. R. Julian, Y. Maeno, S. Nishizaki, and T. Fujita. Hall effect in the two-dimensional metal Sr_2RuO_4. *Phys. Rev. B* 54, 7425 (1996).

[232] R. S. Perry, L. M. Galvin, A. P. Mackenzie, D. M. Forsythe, S. R. Julian, S. I. Ikeda, and Y. Maeno. Hall effect of $Sr_3Ru_2O_7$. *Phys. B: Condens. Matter* 284, 1469 (2000).

[233] L. M. Galvin, R. S. Perry, A. W. Tyler, A. P. Mackenzie, S. Nakatsuji, and Y. Maeno. Hall effect in single crystal $Ca_{2-x}Sr_xRuO_4$. *Phys. Rev. B* 63, 161102 (2001).

[234] H. Yoshino, K. Murata, N. Shirakawa, Y. Nishihara, Y. Maeno, and T. Fujita. Thermopower of a Layered Perovskite Superconductor, Sr_2RuO_4. *J. Phys. Soc. Jpn.* 65, 1548 (1996).

[235] X. F. Xu, Z. A. Xu, T. J. Liu, D. Fobes, Z. Q. Mao, J. L. Luo, and Y. Liu. Band-Dependent Normal-State Coherence in Sr_2RuO_4: Evidence from Nernst Effect and Thermopower Measurements. *Phys. Rev. Lett.* 101, 057002 (2008).

[236] N. Keawprak, R. Tu, and T. Goto. Thermoelectric Properties of Sr-Ru-O Compounds Prepared by Spark Plasma Sintering. *Mater. Trans. JIM* 49, 600 (2008).

[237] D. K. MacDonald. *Thermoelectricity: An Introduction to the Principles* (John Wiley and Sons, New York and London, 1962).

[238] J. M. Ziman. *Principles of the Theory of Solids* (Cambridge University Press, Cambridge, 1972).

[239] P. Voruganti, A. Golubentsev, and S. John. Conductivity and Hall effect in the two-dimensional Hubbard model. *Phys. Rev. B* 45, 13945 (1992).

[240] M. Itoh. Hall effect of noninteracting electrons as a Fermi-surface property: A rigorously derived gauge-independent formula in the on-shell form. *Phys. Rev. B* 45, 4241 (1992).

[241] W. Xu, K. Haule, and G. Kotliar. Hidden Fermi Liquid, Scattering Rate Saturation, and Nernst Effect: A Dynamical Mean-Field Theory Perspective. *Phys. Rev. Lett.* 111, 036401 (2013).

[242] J. Mravlje, M. Aichhorn, T. Miyake, K. Haule, G. Kotliar, and A. Georges. Coherence-Incoherence Crossover and the Mass-Renormalization Puzzles in Sr_2RuO_4. *Phys. Rev. Lett.* 106, 096401 (2011).

[243] Y. Maeno, K. Yoshida, H. Hashimoto, S. Nishizaki, S. Ikeda, M. Nohara, T. Fujita, A. P. Mackenzie, N. E. Hussey, J. G. Bednorz, and F. Lichtenberg. Two-Dimensional Fermi Liquid Behavior of the Superconductor Sr_2RuO_4. *J. Phys. Soc. Jpn.* 66, 1405 (1997).

[244] A. P. Mackenzie and Y. Maeno. The superconductivity of Sr_2RuO_4 and the physics of spin-triplet pairing. *Rev. Mod. Phys.* 75, 657 (2003).

[245] N. P. Ong. Geometric interpretation of the weak-field Hall conductivity in two-dimensional metals with arbitrary Fermi surface. *Phys. Rev. B* 43, 193 (1991).